A Detailed Study of Axon Initial Segment Maturation and Structural Organization by Fluorescence Microscopy

Dissertation

for the award of the degree

"Doctor rerum naturalium"

of the Georg-August-Universität Göttingen

within the doctoral program GGNB

of the Georg-August University School of Science (GAUSS)

submitted by

Melanie Dannemeyer

from Brake (Unterweser), Lower Saxony

Göttingen 2015

Members of the Thesis Committee:

Prof. Dr. J. Enderlein (Reviewer)

3rd Institute of Physics - Biophysics, Faculty of Physics

Georg-August-University Göttingen

Dr. A. Neef (Reviewer)

Bernstein Center for Computional Neuroscience Göttingen

MPI for Dynamics and Self-Organization

Prof. Dr. K. Tittmann

Department of Bioanalytics, Faculty of Biology and Psychology

Georg-August-University Göttingen

Prof. Dr. Luis A. Pardo

Department of Molecular Biology of Neuronal Signals

Max Planck Institute for Experimental Medicine

Dr. Dieter Klopfenstein

3rd Institute of Physics - Biophysics, Faculty of Physics

Georg-August-University Göttingen

Dr. Florian Rehfeldt

3rd Institute of Physics - Biophysics, Faculty of Physics

Georg-August-University Göttingen

Date of oral examination: 25.01.2016

Affidavit

Hereby, I declare that the presented thesis has been written independently and with no other sources and aids than quoted.

Göttingen, 26.11.2015

Contents

Abstract

The distribution and density of neuronal voltage-gated sodium channels (VGSCs) is important for neuronal excitability, maturation and plasticity. High density of VGSCs in the axon initial segment (AIS) depends on the cytoskeletal proteins βIV-spectrin and ankyrin-G (ankG). Here, the density and structure of βIV-spectrin, βII-spectrin, ankG and VGSCs in the AIS is studied with maturation. Neuronal cultures were prepared from hippocampus and immunofluorescence was imaged between 7 and 21 *days in vitro* with conventional wide-field and stochastic optical reconstruction microscopy (STORM).

At the earliest time point studied, *DIV 7*, βII-spectrin is arranged in the AIS on a very regular structure. With maturation βII-spectrin density decreases slightly, while the density of βIV-spectrin increases in the AIS. Neuronal βIV-spectrin appears in two isoforms βIV$\sum$1 and βIV$\sum$6. Within this detailed study the density and structural organization of βIV-spectrin is examined in detail. The mean fluorescence intensity of βIV-spectrin labeled at its N-terminus is found on a constant level starting at *DIV 14*. Based on the fact that N-terminal labeling targets βIV$\sum$1, but not βIV$\sum$6, the mean fluorescence intensity stagnates within the second week of studied maturation and a prominent periodic organization is revealed, it is suggested that βIV$\sum$1 is highly enriched early on, arranged in the AIS on a very regular basis and functions as the main stabilizing βIV-spectrin isoform. Contrariwise, C-terminal labeling of βIV-spectrin reports an increase of the mean fluorescence intensity over the whole three weeks of studied maturation. Moreover, at *DIV 6* βIV-spectrin is found on a very regular basis, whereas at *DIV 14* a diffuse distribution is observed. Based on the fact that C-terminal labeling targets βIV$\sum$1 and βIV$\sum$6, the careful study allows to conclude that the detected increase of the mean fluorescence intensity and thus likely an increase of the density of βIV-spectrin density is due to an increase of βIV$\sum$6. Further, a diffuse βIV-spectrin structure in mature neurons suggests an irregular placement of βIV$\sum$6 in the existing regular structured cytoskeleton of actin-adducin rings. The adapter protein ankG mediates the contact between VGSCs and the underlying cytoskeleton. Its density is found to increase over the studied maturation period. AnkG is found organized prominently periodically in immature neurons. With maturation the periodic organization of ankG becomes less pronounced. Whereas previous studies simplify the observation by reporting the distance of ankG to the underlying network and the distribution of binding positions on a spectrin tetramer are the cause, not considering that these conditions are not only found in mature neurons, but also immature neurons, here a high quality study suggests non-periodic βIV$\sum$6 as a mediator for the increase of irregularity of ankG. In agreement with ankG, the density of VGSCs and specifically the densities of the subtypes $Na_v1.2$ and $Na_v1.6$ increase with maturation. Additionally, the data suggest an early expression of $Na_v1.2$

(measured *DIV 6*) and a late expression of $Na_v1.6$ (not detected at *DIV 7*, but at *DIV 10*). Whereas, $Na_v1.2$ is found proximal in immature and evenly distributed in mature neurons, is $Na_v1.6$ found distal in mature neurons and evenly distributed in immature neurons. A developmental switch from one subtype to another is not found. VGSCs and specifically $Na_v1.6$ are found (semi-)periodic. The data obtained for $Na_v1.2$ organization do not allow to draw a final conclusion, yet. The mouse strain qv^{3J} is a loss of function mutation in the βIV-spectrin gene (Spnb4). A single inserted base (InsT6786) causes a frameshift at amino acid G2209 and a completely changed new 49-amino-acid C-terminal extension.[1] Here, the effect of this mutation on the expression and structural organization of βII-spectrin, βIV-spectrin, ankG and VGSCs in the AIS is studied. At *DIV 7* wildtype and mutant neurons are very similar with respect to density and periodicity of ankG, VGSCs and βII-spectrin. However, only very little βIV-spectrin is observed in mutant qv^{3J} neurons at *DIV 7* and is not detectable when labeling *DIV 14* neurons. The density and regularity of βII-spectrin is not altered, suggesting that it has no role within a rescue mechanism for βIV-spectrin absence. In contrast to the maturation in wildtype no increase of the ankG and VGSCs density is observed in qv^{3J} mutant neurons. AnkG is found at a constant density and arranged strongly periodic between *DIV 11 - 24*. This supports its binding to βII-spectrin and suggests an absence of βIV∑6 as an irregular cytoskeletal binding partner. The VGSC density in mutant qv^{3J} neurons decreases progressively in the three weeks of studied maturation. A detailed analysis suggests that $Na_v1.2$ channels are not stabilized and constantly decrease in density with maturation, whereas $Na_v1.6$ channels are rare at all ages, due to a not fully functional recruitment mechanism of VGSCs by the ankG-βIV-spectrin complex. Furthermore, the constant ankG density, but a consecutive decrease of VGSC density, suggests a direct relation between VGSCs and βIV-spectrin. The disruption of the complete mechanism is suggested to be mainly due to a disrupted βIV∑1, an isoform suggested to function as a stabilizer, and the complete absence of βIV∑6, an isoform suggested to function as a recruiter for VGSCs in neuronal maturation.

To conclude, βIV-spectrin is incorporated in the existing βII-spectrin grid, βIV∑1 periodic and βIV∑6 non-periodic. The ring-like organization of proteins along the AIS does not depend on βIV-spectrin. The C-terminal mutation qv^{3J} causes a complete loss of βIV-spectrin. The βIV-spectrin C-terminal tail is essential for its incorporation and stabilization. βIV-spectrin is a key component in ankG and VGSC recruitment. βIV-spectrin is crucial for VGSC stabilization. In addition, ankG stabilization depends strongly on βII-spectrin.

1 Motivation

Neurons in the brain exchange information in a digital code, by means of brief electrical pulses, called action potentials. The action potential (AP) is generated in the axon initial segment (AIS).[2][3] The AIS underlies a complex maturation progress and a highly specialized composition, including a unique structural organization, which allows the enrichment of voltage-gated sodium channels (VGSCs), lowering its threshold and giving it the functionality as the site of AP initiation.[4][5][6][7][8] AIS dysfunctions, mediated by composition alterations, have been linked to multiple neuronal disorders, such as epilepsy, Alzheimer's and schizophrenia.[9][6] In order to understand AIS dysfunction and identify abnormalities in composition, the maturation and structure of the AIS needs to be fully understood. Thereby, it is of interest to establish a detailed model of the AIS structure, and monitor and quantify concurrent maturation of cytoskeletal proteins and the functional VGSCs. The two methods used in this thesis, wide-field and stochastical optical reconstruction microscopy (STORM) imaging, allow (i) a semi-quantification of AIS protein expression levels with AIS maturation and (ii) imaging of structural organization. The goal of the thesis is to present a model of the AIS, showing its full complexity and leading towards a better understanding of the AISs functionality and observed phenotypes during diseases.

Previous work within the Bernstein Group "Biophysics of neural information encoding" focused on the maturation of electrophysiological properties in hippocampal neurons. Neurons were monitored between the age of *DIV 6* to *55 in vitro*. The somatic AP waveform was analyzed to extract parameters thought to reflect the functional properties and densities of VGSCs in the axon (AP threshold, voltage dependence of the initial rate of change of the membrane potential $(d^2V/dtdV)$) and in the soma (peak rate of rise of the membrane potential). Axonal and somatic components changed significantly within the first two weeks and stabilized at the end of the third week, suggesting that the neurons reached their mature stage.[1] As the functionality of the AIS has been shown to depend on the enrichment of VGSCs,[4][5][6][7][8] it is of interest to monitor simultaneously the compositional and structural maturation of the AIS. Here, it is focused on monitoring VGSC density, especially the subtypes $Na_v1.2$ and $Na_v1.6$, until the neurons reach the their mature stage. Further, it is of interest to look at the densities of cytoskeletal proteins, such as βIV-spectrin and ankyrin-G (ankG), which have been shown as function as linker and adapter proteins for proper VGSC placement and thus play a role in AIS maintenance (**Chapter: 4**). Besides protein densities, a deeper insight is gained by a structural study.

---

[1] Previous work: Electrophysiology measurements on wildtype neurons were performed by Elinor Lazarov, *Hebrew University of Jerusalem, Israel* during her PhD thesis. Manuscript: (1) Elinor Lazaorv, Melanie Dannemeyer, Anja Huss, Michael Gutnick, Fred Wolf, Andreas Neef "Functional and structural maturation of the axon initital segment in cultured hippocampal neurons."

In January 2013 the lab of *Xiaowei Zhuang* reported the existence of a highly regular cytoskeleton and associated VGSCs in the AIS of rat hippocampal neurons. Based on their high resolution images obtained by STORM microscopy, a model of the structural organization of AIS proteins has been established. The work was performed based on a previous model of the actin-adducin-spectrin-ankyrin network, imaged underneath the membranes of swollen erythrocytes.[10] *Xiaowei Zhuangs* lab studied actin, adducin, βII-spectrin, βIV-spectrin, ankyrin-B (ankB) and VGSCs in detail (slightly modified model: 2).[11] Further, maturation of the structural organization has been published in December, 2014. Here, the proteins, actin, adducin, βII-spectrin, βIV-spectrin and ankG have been studied.[12] Combined, these two publications give a first idea of AIS organization and its structural maturation. Although, recently studies on structural AIS organization get numerous[11][12][13], questions remain and results are not proved and analyzed in detail. Such simple models (slightly modified model: 2) mask the full complexity of the AIS. For example, diverse results obtained by N- and C-terminal labeling of βIV-spectrin have not been examined in detail, instead non-verified suggestions, such as freely moving C-terminal tail regions and an increase of the protein densities have been made.[12][13] It has not been considered that these assumptions do not agree with their published model. This addresses the question of sufficiency and correctness of the model. Within this thesis the main focus is on differential structural organization of βIV-spectrin and ankG isoforms, and VGSC subtypes, $Na_v1.2$ and $Na_v1.6$, whereby the different roles of protein isoforms and subtypes are demonstrated (**Chapter: 5**). Together, the electrophysiological characterization [1], protein density studies as well as structural organization of VGSCs and cytoskeletal proteins allow the establishment of a new more detailed functional and structural model of the AIS throughout neuronal maturation.

In another part of the project, the consequences of a mutation in βIV-spectrin were studied. The qv^{3J} mutant displays a small, but perturbing defect in the cytoskeletal protein βIV-spectrin. βIV-spectrin has been suggested as appearing early in maturation and being the main stabilizer of the AIS architecture. Numerous proteins, such as ankyrins and VGSCs have been reported to be properly stabilized by the key element βIV-spectrin.[14][15][16][17][18][19] Previous work within this project revealed similar AP waveforms in the first two weeks of maturation for qv^{3J} mutant and control neurons. Starting the third week AP onset in qv^{3J} mutant neurons slowed down significantly. [2] Consequently, the AIS function is affected by the mutation and suggests a defect of VGSC enrichment in the AIS. Most likely are defects of stabilization. Here it is of major interest to monitor the density of VGSCs and the cytoskeletal proteins, βIV-spectrin and

---

[2]Previous work: Electrophysiology measurements on control (wildtype/heterocygote) and qv^{3J} mutant neurons were performed by Elinor Lazarov, *Hebrew University of Jerusalem, Israel* during her PhD thesis. Manuscript: (2) Elinor Lazarov, Melanie Dannemeyer, Michael Gutnick, Fred Wolf, Andreas Neef "Reduced Nav channel density in the axon initial segment slows down the action potential onset and impairs high frequency encoding."

ankG, with maturation (**Chapter: 6**). Further, a detailed structural study leads towards a better understanding of the mechanism, which impairs information encoding in the qv^{3J} mutant (**Chapter: 7**). [2] Thereby, the qv^{3J} mutant demonstrates the importance of maintaining the AIS structure for its full functionality.

2   Introduction

2.1   The Neuron

The hippocampal neuron consists of a cell body, referred to as the soma, and two classes of branches, referred to as axons and dendrites. A typical neuron has one axon and several dendrites, which arise from the soma. Both processes form complex axonal, respectively dendritic trees. The axonal region close to the soma is called the axon hillock. A special about 20 µm region of the axon is called the axon initial segment (AIS).[20] [21] It contains a special protein composition and arrangement. Upon a stimulus, which leads to a depolarization above the threshold potential, an electrical signal, the action potential (AP), is initiated in the AIS and propagated towards surrounding neurons. The neurons are connected with each other by junctions, referred to as synapses. At these regions the membranes of two neurons are located close to each other and allow the transfer of an electrical or chemical signal from one to another neuron. The signal is received by dendrites of the connecting neurons and propagated towards their soma. A new all or nothing AP is initiated in the AIS of these neurons.[22]
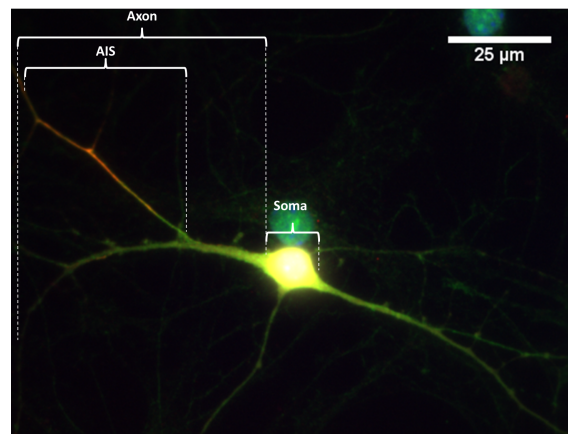
Figure 1: The hippocampal neuron. The image shows a hippocamal neuron at *DIV 14*, filled with Alexa 568 (yellow) using a patch pipette, stained for voltage-gated sodium channels (VGSCs) with Alexa 488 (red), ankG with Alexa 647 (green) and nucleus with DAPI (blue). Imaging was performed by wide-field microscopy with a 60 x objective (method: 3.4, using an additional excitation (Semrock, BLP01-594R-25) filter to separate the emission light). The main parts of the axon, the AIS and the soma are labeled. Several dendrites arise from the soma. *The neuron was patched and filled by Elinor Lazarov (Hebrew University Jerusalem, Israel), labeling and imaging was performed by myself.*

2.1.1   The Axon Initial Segment

The axon initial segment (AIS) is a highly specialized neuronal subregion. [21] [5] [6] It is located in the proximal region of the axon, directly distal of the axon hillock, where the axon arises from the cell body. [6] Its exact position varies across and within different cell types and is amongst others modulated by activity. [23] In recent experiments two days depolarization of mature hippocampal neurons resulted in a significant shift of their AIS. The AIS has been moved up to 17 μm further away from the soma. Returning to normal conditions showed reversibility of this process. [24]

The length and size of the AIS varies between neuronal cell types and organisms. Early electron microscopy studies (from 1976) of the AIS on purkinje cells (PCs) of rats revealed a length of about 17.1 +/- 2.0 μm, a diameter of 0.79 +/- 0.10 μm at the origin, a diameter of 0.73 +/- 0.19 μm at the beginning of myelin and a total surface of about 45.6 μm^2. [20]

The AIS is involved in action potential (AP) initiation, modulation and propagation by converting the dendritic input into an all or nothing AP. [4] [5] [6] It is highly enriched with ion channels, including voltage-gated sodium channels (VGSCs) [7] [8], which lower the threshold for AP initiation and lead to a fast inward current during the rising phase of depolarization. [6] Electrophysiology [3] [25] and immunogold labeling [26] [27] experiments revealed that the channel density in the AIS is about 40 to 50 (electrophysiology), respectively 35 to 80 (immunogold labeling) times higher than that of the soma or dendrites. [21] The threshold for initiation depends amongst others on the position of the AIS. More distal located AISs have been shown to have higher thresholds for initiation. [24]

Early electrophysiological [25] and immunohistochemistry studies indicated an evenly distribution of VGSCs throughout the AIS. [28] [29] Recent immunohistochemistry experiments combined with novel imaging techniques indicate that the AP is formed at the distal part of the AIS. [30] [31] [6] The subtype $Na_v1.2$ has been identified as being located in the proximal part of the AIS and displays a high threshold, whereas the subtype $Na_v1.6$ has been found more distal and displays a low threshold for initiation. [31] [6]

Besides VGSCs [7] [8] [6], the AIS is enriched with associated proteins, such as the adapter protein ankG [32] (details: 2.3), the cytoskeletal linker protein βIV-spectrin (details: 2.2) and cell adhesion molecules. [33] [34] The composition functions as a barrier between the axonal and somatodendritic compartments for maintenance of neuronal polarity. [35] [36] [25] [5] The lateral mobility of membrane proteins has been demonstrated to differ in the AIS and distal axon. [36] [5] Some membrane proteins, such as the L1 family proteins, neurofilament (NF) and neuronal adhesion molecule (NrCAM), show a very slow or no diffusion in the AIS. [35] A disruption of the underlying cytoskeleton results in a loss of the barrier and thus an increase of membrane protein diffusion. Highly debated remains the sequence of protein recruitment to the AIS.

1. NF and NrCAM have been proposed to cluster prior ankG in the AIS [34],

2. but others suggest that ankG first localizes in the AIS and all other proteins [5], including NF and NrCAM, are recruited by ankG through their ankG binding sites. [6]

3. Also, the ankG-βIV-spectrin complex has been described to form the AIS before ion channels cluster. [37] [17] [6]

4. Even the theory that the sodium channel β-subunit of VGSCs plays a role in recruiting ankG has been suggested. [38]

The structural organization of proteins in the AIS is particular. [11] [12] Actin forms ring-like structures along the entire axon, but not in dendrites. The actin rings are evenly spaced in about 180 - 190 nm. Adducin [39], an actin-capping protein, colocalizes with the actin ring-like structures and composes a ring-like organization. The distance between each actin-adducin ring is about 182 +/- 16 nm. [11] [12] This corresponds to the length of a spectrin tetramer, which is formed from two 100 nm long spectrin heterodimers [40] [10] [11] [12], and connects the actin-adducin rings with each other by binding to a specific site on the actin (more information: 2.2). Similar organization for actin and spectrin has been described earlier for the cytoskeleton of erythrocytes. [41] [40] [42] [14] [43] [44] Each spectrin tetramer [40] [44] contains two binding sites for the adapter protein ankG. [42] [45] The binding sites are located on the β-spectrin chains more closely towards the C-termini (more information: 2.2). Due to its two binding sites to spectrin, which are closely located to each other, ankG displays a periodic organization approximately halfway between the actin rings or halfway between the spectrins N-termini (more information: 2.2). [12] VGSCs are highly enriched in the AIS. They are connected to spectrin by binding to the adapter protein ankG. [46] [47] [12] Based on the underlying cytoskeletal structure they appear as an organized pattern halfway between the actin rings (or halfway between the spectrins N-termini, colocalized with ankG). [11] [12]
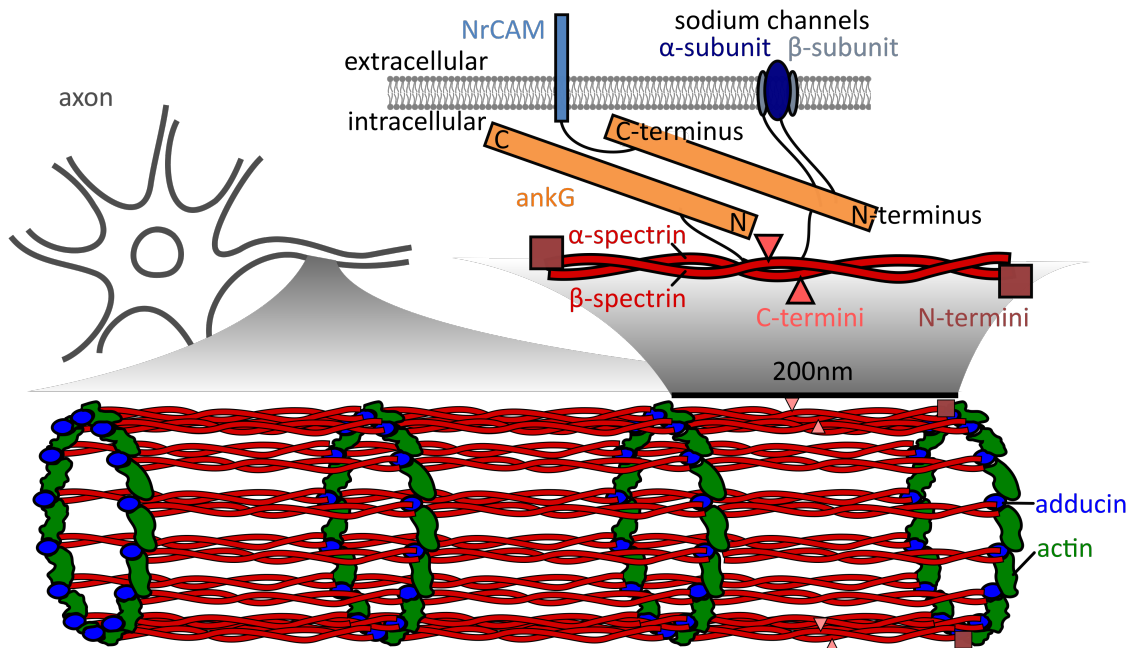
Figure 2: A schematic view of the AIS. Actin, capped with adducin, is organized in ring-like structures. Actin rings are connected by spectrin tetramers with a length of about 200 nm. N-termini of the spectrin tetramers are orientated towards the actin. AnkG binds to ankyrin-binding sites of β-spectrins. Integral membrane proteins, such as sodium channels and the cell adhesion molecule NrCAM, are connected by ankG to the underlying cytoskeleton. Figure has been *modified and extended from* [11] [12] [48] [49] [25] [6].

## 2.2   The cytoskeletal protein spectrin

Spectrin is a major component of the neuronal membrane skeleton.[19] It has been first described in red blood cells, erythrocytes[50] [41] [43], where it is part of forming a network amongst others with anykrins, to resist shear forces.[50] Sequence analysis suggests that it has been evolutionary evolved before ankyrins. [51] [19] Spectrins are distinguished in α- and β-spectrins. The two major isoforms of α-spectrin are encoded by the genes *SPTA1* and *SPTBAN1*.[19] The five β-spectrins, βI-V spectrin, are encoded by the genes *SPTB*, *SPTBN1*, *SPTBN2*, *SPTBN4*, and *SPTBN5*.[48] [19] The core element of spectrin is a helical repeating unit, the spectrin repeat.[19] α-spectrins have typically 20 to 21 and β-spectrins 17 repeats. [44] [52] Their sequence homology is less than 30 %. [19] Spectrins form tetramers consisting of two α- and β-spectrins[40] [44] [53] [16], 200 nm in length.[40] [43] Interactions between two repeats, located close to the C-terminus of α-spectrin, repeat 20 and 21, and two repeats, located close to the N-terminus of β-spectrin, repeat 1 and 2[54], form a dimer of α- and β-spectrin. [48] The α-spectrin repeat 1 and β-spectrin repeat 17 of the heterodimer interact with the corresponding repeat of a second heterodimer. [55] [56] [57] [19] This head-to-head association forms a spectrin tetramer. [58] [59] [16]

In spectrins, a number of domains and binding sites have been identified. An actin-binding domain

(ABD)[43][60] mediates the binding of spectrin to the underlying actin network (figure: 2).[16][19] Further, a SH3 domain and a PH-domain are found.[16] SH3- and PH-domains are common features of proteins involved in cellular signaling.[19][61] The role of spectrin e.g. in lymphocyte activation has been described earlier. Additionally, PH-domains play a role in cytoskeletal organization.[19] EF-hand domains, located on the α-spectrin, have been shown to modulate the actin-binding domain.[19] The ankyrin-binding site is located between the 14th and 15th repeat, close to the C-terminus, of each β-spectrin.[62][53][63][57][19]

βIV-spectrin is located on the human and mouse chromosome 19p13.13 and 7b2.[16] It is 8789 bp long and has 2559 amino acids. Alternative splicing generates six isoforms of βIV-spectrin referred to as βIV∑1 - βIV∑6 (βIV∑1 Genbank No. NM_020971, βIV∑6 Genbank No. NM_-001199234.1, NM_001199235.1 and NM_001199236.1).[16][17][18] The role of βIV-spectrin has been extensively studied.[16] Immunohistochemistry studies showed that βIV-spectrin colocalizes with ankG, VGSCs and cell adhesion molecules (such as NF and NrCAM) in the AIS.[60][16][19] It is commonly accepted that spectrin is recruited by ankG and forms a stable complex with membrane proteins.[64] Knockout of βIV-spectrin in mice showed abnormal ankG and VGSC distribution or loss and a quivering phenotype.[17][18] Mice lacking only the isoform βIV∑1 showed a quivering phenotype, too.[18] Therefore, βIV∑1 has been described as being the main isoform of βIV-spectrin for the stabilization of the AIS and nodes of Ranvier (noR) membranes.[15][16][18]
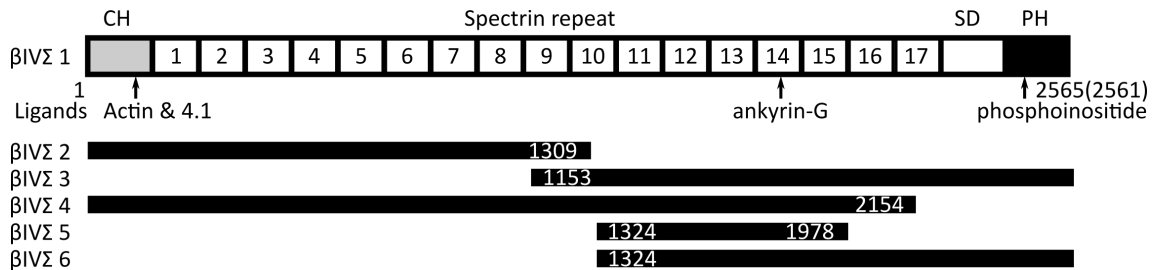
Figure 3: A schematic view of the βIV-spectrin isoforms. βIV∑1 is shown in detail. βIV∑2 - βIV∑6 aligned to βIV∑1. Amino acid sequences of isoforms do not correspond completely. Short insertions, deletions and extensions of βIV∑2 - βIV∑6 relative to βIV∑1 are ignored. White numbers indicate the relative starting and ending amino acid of each isoform in relation to βIV∑1. Ligand binding sites are marked. CH, calponin homology domain; SD, specific domain; PH, pleckstrin homology domain, *modified and extended* [18] *Uniprot.org: Q9H254 , Q8VBX2.*

2.3 The adapter protein ankyrin

Ankyrins are a family of large adapter proteins that link integral membrane proteins to the underlying spectrin-actin cytoskeleton.[65][60][66][67][68][69] The genes *ANK1* [32], *ANK2* and *ANK3* [70] code for the three subtypes ankR [71], ankB and ankG.[70] Each of them appears as a

number of specific isoforms resulting from alternative splicing. AnkR has been first detected in red blood cells, erythrocytes, where it links spectrin to the plasma membrane and provides resistance to shear forces. [50] [42] Ankyrins are composed of four functional domains. An N-terminal domain with 24 tandem ankyrin repeats identified as the membrane-binding domain, a spectrin-binding domain (ZU5 1 domain) [45] [72], a domain that bind proteins of the apoptosis pathway, and a variable C-terminal domain. [67] A mutation in the spectrin-binding domain (ZU5 1 domain) in giant 480 kDa ankG did not affect its ability to recruit β-spectrin. Suggesting that the spectrin-binding domain plays no role in spectrin recruitment. Instead, S2417, located in the 1,900 amino acid region, has been identifed to play a role in β-spectrin binding and recruitment. [73]

The membrane binding domain of ankyrin is composed of four subdomains, each containing six ankyrin repeats. [74] The scaffold protein ankG plays a key role in neuronal development, polarity and stabilization. [75] [76] [7] [17] [77] The role of ankG has been studied extensively by developmental immunohistochemistry in tissues and cell cultures derived from rats and mice including null-mutants, region-specific ankG knockouts and the reduction of the expression by short hairpin RNAs (shRNA). [76] [77] [68] [78]

AnkG is highly concentrated in the AIS [32] [76] where it colocalizes with βIV-spectrin [16] [7] (more information: 2.2) and integral membrane proteins, such as VGSCs [79] [80] [7], NF-186 and NrCAM. [81] [75] [7] Further, it can be found at a lower level in the cell bodies of neurons. [82] [83] It is expressed at stage P2 [7] and therefore one of the earliest expressed proteins. [7] [5] The unique serine-rich domains and the highly divergent tail domain present in the isoforms 480- and 270-kD ankG [32] [82] contribute to its highly specific restriction to the AIS and limit its lateral diffusion. [82] [84]

The lack of ankG results in a complete loss of the cytoskeletal protein βIV-spectrin, which is linked by ankG to the plasma membrane. [76] [7] [17] Opposite, βIV-spectrin links the ankG-membrane protein complex to the underlying cytoskeleton. Concluding, ankG is necessary for the assembly of the spectrin-based cytoskeleton. [65] [76] [7] In ankG knockout mice abnormal distribution or complete loss of the NrCAM [76] [7] and VGSC have been observed. Controversial, NF has been described as appearing normal, disrupted [7] or completely lost [82]. Knockdown of NF or NrCAM does not prevent the formation of an ankG based AIS in cultured hippocampal neurons. [67] [34] Deletion of the sodium channel α-subunit had no effect, but deletion of the β-subunit had an effect on recruiting ankG to the AIS. [38] However, the study could not rule out that the β-subunit plays an indirect, but not direct role in recruiting ankG. [38] Therefore it is commonly accepted in the field that the recruitment of βIV-spectrin [7], NrCAM [38] [7] and VGSC [7] [84] depends on ankG. [7] [5]

Further, silencing of ankG expression caused the axon to show dendritic characteristics. [85] Proteins, normally restricted to the somatodendritic domains, such as MAP2, have been detected

in the axon. [85] [5] Proteolysis of the ankG-βIV-spectrin complex resulted in a loss of VGSCs. [86] Both results support that ankG has a role in the maintenance of neuronal polarity. [85] [86] The role of ankG in VGSC stabilization[76] [7] [78] has been supported by site-directed mutants with decreased affinity for ankG and increased diffusion speed of VGSCs. [84] Channels not anchored by ankG are removed by endocytosis. [87]

In many integral proteins cytoplasmic ankG binding sites have been identified. This includes NF, NrCAM[46] [88], VGSCs and potassium channels. NF and NrCAM bind through a conserved domain (FIGQY motif) in their cytoplasmic C-termini to ankG. [88] The channel subtypes $Na_v1.2$ and $Na_v1.6$ show a common ankG binding domain in the cytoplasmic II-III loop of the α-subunit. [77] [89] [90] Region-specific mutations of the ankG binding domain of βIV-spectrin and other AIS proteins have shown that it is crucial for their AIS localization. [17]

Figure 4: A schematic view of the giant 480 kDa and the 270 kDa ankG isoforms. Giant 480 kDa ankG is shown in full length. 270 kDa ankG has been aligned. Amino acid sequences do not correspond completely. Short insertions, deletions and extensions of 270 kDa ankG are ignored. White numbers indicate the relative starting and ending amino acid of 270 kDa with respect to giant 480 kDa ankG. The spectrin-binding domain and the S2417, located in the 1,900 amino acid region, are marked (blue). *Established after* [73] and *Uniprot.org: Q12955, W6PPA1.*

2.4 Voltage-gated sodium channels

Channels are pore-forming units within the membrane of cells. Sodium channels mediate the selective influx of sodium ions from the extracellular region through the membrane into the cell. It is distinguished between ungated and gated sodium channels. Whereas ungated sodium channels are always open, underlie gated sodium channels a regulartory mechanism. Gated sodium channels are particular found in neurons. The gating mechanism can be conrolled either by chemical or electrical signals. In voltage-gated sodium channels (VGSCs) gating depends on an electrical signal. [22]

VGSCs (Na_v) consist of α- and β-subunits. [91] The pore-forming α-subunit has four homologous protein domains (I-IV) [92], each of them with six transmembrane segments. The β-subunits have a single transmembrane segment with an extracellular N-terminus and a cytoplasmic C-terminus. β-subunits modulate α-subunits and regulate channel gating. [93] [92] Ten genes have been identified to encode the α-subunit, referred to as $Na_v1.1$ - $Na_v1.9$ (Genes: *SCN1A - SCN5A, SCN8A, SCN9A - SCN11A*) and $Na_v x$ (*SCN7A*). [94] Four genes encode the β-subunits $Na_v β1$ - $Na_v β4$ (Genes:

SCN1B - SCN4B), whereas $Na_v\beta1$ assembles with the α-subunits $Na_v1.1$ to $Na_v1.7$, $Na_v\beta2$ with $Na_v1.1$, $Na_v1.2$, $Na_v1.5$ to $Na_v1.7$, $Na_v\beta3$ with $Na_v1.1$ to $Na_v1.3$, $Na_v1.5$ and $Na_v\beta4$ with $Na_v1.1$ to $Na_v1.2$ and $Na_v1.5$.[95][96]

The channel subtypes $Na_v1.7$, $Na_v1.8$ and $Na_v1.9$ are highly concentrated in the pheriperal nervous system (PNS).[69] $Na_v1.4$ and $Na_v1.6$ are found in cardiac and skeletal muscles. The subtypes $Na_v1.1$[29], $Na_v1.2$[29][8], $Na_v1.3$ and $Na_v1.6$[97][29] are mainly expressed in the adult central nervous system (CNS).[69][27] $Na_v1.2$ and $Na_v1.6$ are the main subtypes of the AIS[29][31], whereas $Na_v1.1$ and $Na_v1.3$ are somatodendritic located.[69]

Immunohistochemistry experiments and modeling studies found differentiated expression of the channel subtypes $Na_v1.2$ and $Na_v1.6$.[31][25] The dominant channel subtype expressed in the AIS is $Na_v1.6$. It has been shown to have a proximal to distal gradient, meaning its concentration increases with increase of the distance from the soma. Analysis of 100.0 µm long immunostainings of the axon showed that the anti-$Na_v1.6$ staining intensity peaks at a distance of 30 to 50 µm from the soma.[31] $Na_v1.6$ has not been detected in somatodendritic parts, indicating that it is expressed at a very low concentration or even exclusively confined to the AIS.[26] The distal located $Na_v1.6$ channels set a low threshold for AP initiation and have been found to characterize the distal site for AP initiation.[30][29]

$Na_v1.2$ channels have been found to be localized proximal of the axon. Immunohistochemistry with anti-panNav showed an intensity peak at 10 to 20 µm[31] (20 to 40 µm)[64] from the soma. 10 to 20 µm corresponds to the proximal located $Na_v1.2$ channels.[31] The proximal $Na_v1.2$ channels have a high threshold and have been found to be responsible for backpropagation. Removel of $Na_v1.2$, but not $Na_v1.6$, results in failure of AP backpropagation.[31]

In noR a developmental switch between $Na_v1.2$ and $Na_v1.6$ has been observed. In early development $Na_v1.2$ is strongly expressed and later replaced by $Na_v1.6$.[98][99] At the noR of adults $Na_v1.2$ is not detectable in more than 80 % of the neurons.[99] In the AIS no developmental switch has been observed. $Na_v1.2$ is the main subtype in early stages, but stays throughout maturation as $Na_v1.6$ increases. At P9 $Na_v1.6$ expression is comparable to adults. The increase of $Na_v1.6$ expression at noR and AIS correlates.[8]

As mentioned above, (in 2.3) both the channel targeting and clustering in the AIS depend on ankG[89][77] The sodium channel α-subunit contains a nine amino acid ankG-binding motif ((V/A)P(I/L)AXXE(S/D)D) between its intracellular loops II and III linking them to the underlying cytoskeletal network.[77][5][90] Mutations of a single glutameric acid residue (E1100) within the motif blocked $Na_v1.6$ targeting *in vitro* and *in vivo*, indicating that the motif is essential and sufficient for ankG binding.[90]

Sodium channel β-subunits interact through an extracellular domain with L1 family adhesion

proteins, such as NF-186 and NrCAM, playing a role in their localization. [38] [100]

Both, alterations and the loss of $Na_v1.2$ and $Na_v1.6$ cause major diseases, such as epilepsy and motor dysfunctions, leading to early death. [4] [101] [102] [9] $Na_v1.6$ null mice die before four weeks of age. [103]

```
hNaV1.1 1115 - - - - - - - - -VPIAVGESDFE- - -
hNaV1.2 1105 - - - - - - - - -VPIAVGESDFE- - -
hNaV1.6  894 - - - - - - - - -VPIAVGESDFE- - -
```

Figure 5: Conserved sequence of ankG binding motifs in sodium channel subtypes, *modified from* [68]. Sodium channels share the same common motif.

2.5   The *quivering* mutation

The autosomal recessive *quivering* (*qv*) mutations arose spontaneous in 1953. Six mutations have been described. Phenotypic expressions are progressive paralysis, ataxia, deafness and tremor starting days after birth. Tail stiffening starting about 30 days after birth, eye infections and sterility of males have been described. Males have found to produce viable sperm, but sired no litters. Females have found to nurse their litters. *Qv* die before 5 month of age. [104] Early studies found mouse homocygote to *qv/qv* being unresponsive to sound, although no abnormalities of their cochleas (auditory portion of the inner ear) have been found. In contrast responses from brainstem auditory nuclei showed abnormalities, indicating a central origin. [105] [106] Qv^{3J} is a loss of function mutation in the βIV-spectrin 4 gene (Spnb4). A single inserted base (InsT6786) resulted in a frameshift at amino acid G2209 and a new 49-amino-acid extension. This extension does not show homologies with the wildtype. The complete mutant peptide is about 14 % shorter than the wildtype peptide. [1] Immunohistochemistry experiments showed a loss of βIV-spectrin associated with ion alterations. [107] The AIS of young 1.5 month old had a higher sodium channel density than the AIS of 6 month old qv^{3J}/qv^{3J}. [64] It has been suggested that the function of the spectrin tetramer to anchor and stabilize channels is defective. No abnormalities for targeting and clustering of ankG have been found. [64]
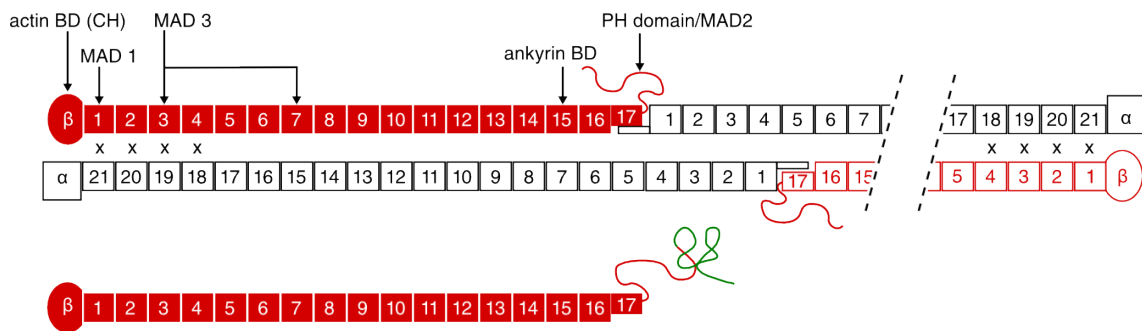
Figure 6: (Top) The spectrin tetramer. β-subunits with 17-spectrin repeats (shown in red, numbered 1-17). α-subunits with 21-spectrin repeats (shown in white, numbered 1-21). Interaction domains are mapped to the β-spectrin peptide. At the N-terminal region, the actin-binding domain (ABD) consisting of two calponin homology (CH) domains. At the C-terminal region the pleckstrin homology (PH), membrane-association (MAD2) and βIV-spectrin specific 'ERQES' domains. The membrane-association domain MAD1 in repeat 1 and MAD3 domains in repeats 3 and 7. The ankyrin-binding domain (ankyrin BD) located in repeat 15. Crosses represent the region of α- and β-peptides for heterodimer association. (Bottom) The predicted qv^{3J} mutant peptide. A new 49-amino-acid extension in βIV-spectrin (green), *modified from* [1].

2.6 Imaging

STORM, stochastic optical reconstruction microscopy[108], belongs to the super-resolution imaging methods. This term summarizes imaging methods, which overcome the diffraction limit (about 200 nm[109]) with optical, chemical or mathematical approaches.[110] STORM allows for high resolution by temporal separation of unresolvable structures.[110][111] The lateral resolution has been reported with about 20 nm.[110][111] Its main advantage is that no high-cost equipment is required. Furthermore, it can be combined with a high number of different fluorescent probes, such as photoactivable fluorescent proteins and organic dyes.[112] STORM has been excessively applied to study biological probes.[110][113][11][12]
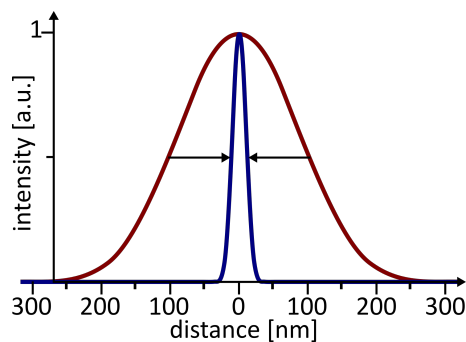

Figure 7: Schematic resolution of wide-field (red) versus STORM (blue) microscopy. Intensity profile of one emitter shows the PSF function of the microscopes [nm].

The target molecule or structure is labeled by a fluorescent probe having a fluorescent ON and

a non-fluorescent OFF state.[108] [111] STORM relies on the sequential activation and inactivation of individual fluorophores. The majority of fluorophores is transferred into the OFF state.[111] A sparse resolvable subset of fluorophores is activated, transferred into the ON state, their positions are determined and transferred back into their OFF state.[111] OFF states have been observed in the range of 10.0 ms to several seconds.[111] At the next point in time, a different subset of fluorophores is activated and their positions are determined.[108] [111] The image is reconstructed from all determined positions.[108] [111] In order to reconstruct a full image at least 2,000 frames need to be recorded.[111] To ensure a full structural reconstruction of a protein of interest frame numbers between 4,000 and 10,000 are recommended. The exact frame number depends on the probe, especially its label density and structural complexity.[111]

The simplest mode is one-color STORM with continuous illumination. Thereby, a single laser wavelength e.g. 647 nm is used to transfer the fluorophores to the OFF state, activate a sparse subset of dyes to the fluorescent state, exciting fluorescence and switching them OFF, allowing for fast imaging.[114] [115]

| (a) all | (b) sparse subset | (c) localize |
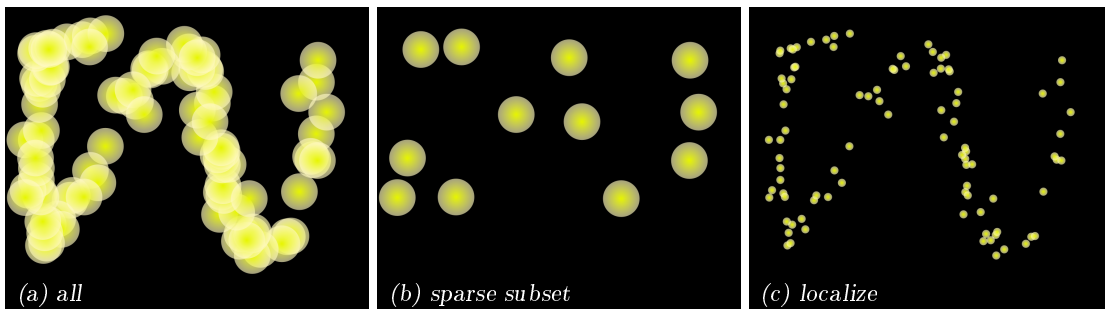
Figure 8: The concept of STORM imaging. (a) The structure of interest is labeled with photoswitchable fluorophores. The fluorophores are in the ON state. All fluorophores are transferred into a non-fluorescent OFF state by irradiation with a laser of suitable wavelength. (b) Spontaneously, a sparse subset is activated. Images are recorded in a specific timescale. (c) Reconstruction of a STORM image by localization of fluorophore positions from each recorded frame. *Modified from* [111].

Organic dyes are reversible switchable and can be converted in a fluorescent ON and OFF state multiple times.[108] [111] [112] The fluorophores switches between the singlet ground state and the excited state by emitting photons. Upon laser illumination the fluorophore can enter the triplet state by intersystem crossing with the rate k_{isc}. By reacting with molecular oxygen it reenters the singlet ground state. If molecular oxygen is removed by an oxygen scavenger system this process is reduced or even eliminated. By adding a thiol, the fluorophore can form a radical anion ($\dot{F}$) with the rate k_{red} and its reentering of the singlet ground state is highly delayed. By reaction with molecular oxygen it reenters the singlet ground state with the rate k_{ox}.[111]

ON and OFF states can be highly modulated by the chemical constitution of the applied imaging

buffers. The OFF state is favored by an increase of the concentration of the thiols.[115] The concentration of reducing thiolates can be either increased by adding a higher concentration or by an increase of the pH of the imaging buffer.[116] The ON state rate is increased by the application of a 400 - 405 nm violet-light laser, which increases the activation rate and reduces the acquisition time.[111][115] The decrease of the ON rate is achieved by removing oxygen with an oxygen scavenger system. Imaging buffers should be adjusted such that 0.1 - 1.0 fluorophores per µm on each frame are ON.[111]

In the majority of publications Alexa 647 is recommended to be used with the thiol MEA (cysteamine hydrochloride, β-mercaptoethylamine), a relative high pH value of 8.0 - 8.5 and an oxygen scavenger system (e.g. an enzymatic system containing glucose oxidase and catalse).[111][115] Recommendations for Alexa 488 are more diverse. It has been described to work well adding low concentrations of the thiol MEA, 1 - 10 mM, high concentrations of MEA, 50 - 200 mM, or MEA in combination with an oxygen scavenging system.[117][118][111]
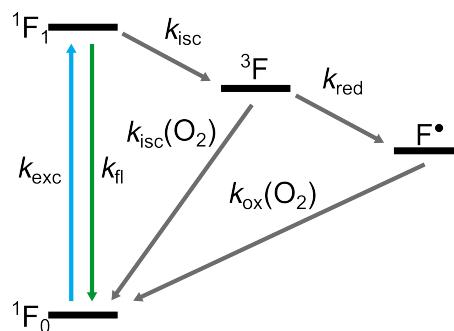
Figure 9: Photoswitching of Alexa dyes. *Modified from*[111].

The resolution is limited by the fluorophore density according to the Nyquist sampling criterion.[110][115] Image quality strongly depends on the number of photons detected per switching cycle and the ON-OFF duty cycle, the time a fluorophore spends in the ON state.[119] For example Alexa 647 has a high number of photons per switching cycle and a low ON-OFF duty cycle and is optimal suitable to resolve small structures.[115]

3 Materials and Methods

3.1 Cell culture

The *C57BL/6N* mice were maintained and provided by the *Tierhaus, Max Planck Institute for Experimental Medicine*. Qv^{3J} mutant mice were provided by *Dr. Nicola Strenzke* and *Gulnara Yamanbaeva, InnerEarLab, The University Medical Center Göttingen*. Breeding of qv^{3J} mutants was performed by the animal caretaker *Daniela Marschall, Zentrale Tierexperimentelle Einrichtung (ZTE), The University Medical Center Göttingen*.

Protocols for hippocampal neuron dissection and cultivation were provided by the technical assistant *Sabine Klöppner, Max-Planck Institute for Experimental Medicine*. General assistance with cell culture was received from the technical assistant *Sabine Klöppner, Max-Planck Institute for Experimental Medicine*.

Preparation of neuronal cultures was performed by myself.

Primary hippocampal cultures were prepared from mice embryos (E17 - 18) (described earlier[120]) (mouse inbred strain *C57BL/6N*) and newborn mice (P0) (described earlier[121]) (qv^{3J} mutant). Hippocampi were isolated. E18 hippocampi were collected in Neurobasal medium (Life Technologies, 12348-017) and P0 hippocampi were collected in Neurobasal-A medium (Life Technologies, 12349-015) with 100 mM HEPES buffer solution (Life Technologies, 15630-056). Afterward hippocampi were digested with Trypsin/EDTA (Biochrom) 0.05 %/0.02 % (w/v) in PBS at 37 ˚C for 15 min.. Trypsin reaction was stopped with 10 % FCS (Biochrom, Cat. 1221) in medium. The hippocampi were transferred to Neurobasal or Neurobasal-A medium with 1:50 B-27 Supplement (Life Technologies, 17504-044), 1:400 Glutamax (Life Technologies, 35050-038) and 0.1 µg/mL bfgf recombinant human protein (Life Technologies, 13256-029). For bfgf stock solution 10 µg powder was diluted in 10 mM TRIS pH 7.6 with 0.1 % BSA. Hippocampi were pipetted up and down, and centrifuged several times until tissue was dissolved.

Wildtype (E17 - 18) derived neurons were seeded on 0.1 mg/mL poly-L-lysine-coated (Sigma-Aldrich, P2636) coverslips (Thermo Scientific, Menzel-Glaeser ø10 mm #1) for wide-field imaging. 200,000 to 250,000 neurons per 2 mL were added in one dish with seven coverslips. For STORM imaging neurons were seeded in polylysine-coated (Sigma-Aldrich, P2636) 4-well chambers (Thermo Scientific nunc, 155383 or Sarstedt, REF94.6190.402); 60,000 to 80,000 neurons per well. Neuron derived from newborn offspring from qv^{3J} mutant were cultivated separately, one offspring per 2 mL and seeded either on slides (6) or in chambers (2 wells). Neurons were cultivated at 37 ˚C with 8.0 % CO_2. Half of the medium was exchanged with freshly prepared medium once a week.

3.2   Genotyping

Genotyping of qv^{3J} mutants was performed by the technical assistants *Sandra Gerke and Christiane Senger-Freitag, InnerEarLab, The University Medical Center Göttingen.*

Breeding of qv^{3J} was performed with heterocygote parent animals and an expected rate of 50.0 % heterocygote, 25.0 % wildtype and 25.0 % mutant offsprings. The obtained offspring were 53.7 % heterocygote, 23.3 % wildtype and 23.0 % mutant and is in agreement with expected ratios.

Genotyping of qv^{3J} P0 offspring was performed using tale biopsies. Primer pairs were F (5'-AGG CAG CGC CTT TGC TGC GTC-3') and R (5'-TCC TGG TCA CAG AGG TCC TTA-3'). Final PCR contained 1.0 µL DNA, 0.2 µL of each primer, 0.4 µL DreamTaq DNA Polymerase (Thermo Scientific, EP0703), and PCR buffer (containing Tris-HCl (pH 8.8), ammonium sulphate (Sigma), MgCl2 (Sigma-Aldrich), 2-mercaptoethanol (Merck), EDTA (pH 8.0) (Sigma), nucleoside triphosphates (dATP, dCTP, dGTP, dTTP) (Promega), BSA (Ambion - Life Technolgies) and H2O).

PCR program:

1. Initial denaturation: 3 min., at 94 ˚C

2. 36 x cycles of

    (a) Denaturation: 30 sec., at 94 ˚C

    (b) Annealing: 30 sec., at 60 ˚C

    (c) Elongation: 60 sec., at 74 ˚C

3. Final elongation: 7 min., at 72 ˚C

PCR product was proved by 2 % gel electrophoresis. Enzymatic digestion was performed with Sty I (10 U/µL) (New England Biolabs, R0500S). Product was separated by 3 % gel electrophoresis. Figure 10 shows an example of a gel from genotyping the qv^{3J} offspring. The bands are clearly visible at 250, 350 and 600 (wildtype +/+ 600 bp, heterocygote +/- 600 bp + 350 bp + 250 bp, mutant -/- 350 bp + 250 bp) indicating a high quality of the gel.
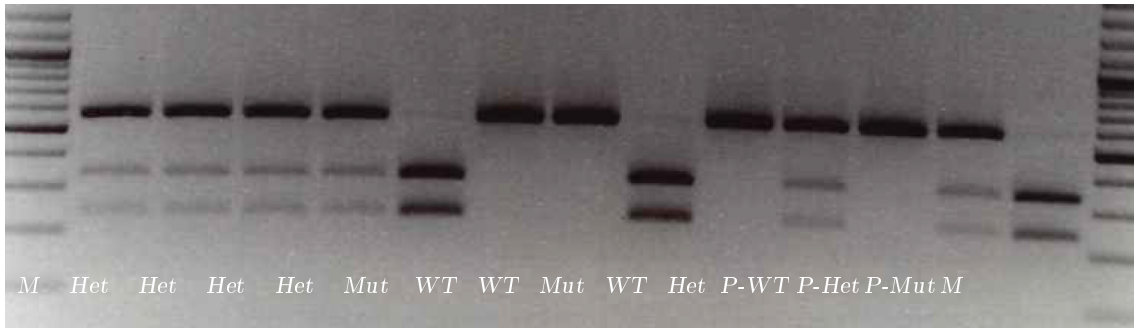
Figure 10: Example of genotyping results from qv^{3J} mutant. M = Marker, WT = wildtype, Mut = mutant, Het = heterocygote, P-WT = positive control wildtype, P-Mut = positive control mutant, P-Het = positive control heterocygote. *Obtained by Sandra Gerke and Christiane Senger-Freitag.*

3.3   Immunohistochemistry

The immunohistochemistry protocol was provided by *Elinor Lazarov, Hebrew University Jerusalem, Israel.* Neurons were fixed and stained by myself.

Neurons were fixed at different days *in vitro* (*DIVs*) with Microscopy Formaldehyde solution 4 % buffered pH 6.9 (Merck, 100496) at 4 °C for 8 min. and permeabilized in 0.5 % (v/v) Triton-X-100 (Sigma-Aldrich, X100) at room temperature for 5 min., followed by a 1.5 h blocking with buffer (3 % (w/v) BSA (Sigma-Aldrich, A0281) in 1x PBS (Life Technologies, 18912-014) and 0.1 % (v/v) Tween20 (Sigma-Aldrich, P7949)). The samples were incubated with primary antibodies (list: 11.2) in blocking buffer at 4 °C overnight. Afterward they were washed and stained with secondary antibodies (list: 11.2) in blocking buffer at room temperature for 45 min.. Coverslips were mounted with ProLong Gold antifade reagent with DAPI (Molecular Probes, P36935) to glass slides and stored at 4 °C. Cultures in chambers were postfixed with Microscopy Formaldehyde solution 4 % at room temperature for 5 min., washed several times with 1x PBS and stored in 1x PBS at 4 °C.

3.4   Microscopy

In this thesis two different microscopy methods were applied: Conventional wide-field microscopy and stochastical optical reconstruction microscopy (STORM).

3.4.1   Wide-field microscopy

Images were recorded using an inverted wide-field microscope (Olympus IX-71) equipped with a water-immersion objective lens (Olympus, UPlanSApo, 60x magnification, NA 1.2). UV (excitation 394 nm), cyan (excitation 476 nm), and red (excitation 634 nm) LEDs (Lumencor, Spectra X light engine) were used for excitation of DAPI, Alexa 488 and Alexa 647 (exposure time for Alexa 488 and Alexa 647 0.1 s; exposure time for DAPI 0.02 s), respectively. The fluorescence light was separated from the LED light with a dichroic beam splitter (Chroma Technologies, 59004bs-Chroma Filters) and additional excitation filters (Semrock, BLP01-405R-25 for DAPI; Semrock, FF01-520/35-25 for Alexa 488; and Semrock, BLP01-635R-25 for Alexa 647) before being imaged on an electron multiplying CCD camera (Andor, EMCCD; DU-897-CS0-BV) with an effective pixel size of 160 nm; temperature of camera -50 °C.
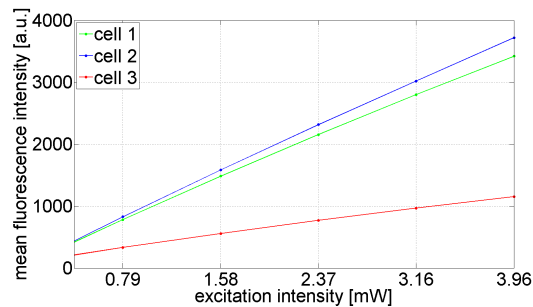
Figure 11: Intensity behavior. Checking for linear intensity behavior of the wide-field (details: 3.4) setup. In some cases, especially high *DIVs*, neurons could not be imaged with a 100 % excitation intensity. In order to ensure that the LED excitation intensity behaves proportional to the emission intensity, calibrations were performed. Three neurons labeled for ankG (C-terminal antibody, sc-28561, 11.2) with Alexa 488 imaged with 2, 4, 10, 20, 30, 40 and 50 % LED intensity. On every image the mean intensity of the same area was determined and plotted. The behavior was approximated as being linear, although in some cases slight deviations were measured.

3.4.2   STORM microscopy

Setup

Images were recorded using an inverted TIRF microscope (Olympus IX-71) equipped with an oil-immersion objective lens (Olympus, UApoN, 100x magnification, NA 1.49, TIRF) and three lasers; a 647 nm laser (PhoxX 647, 140 mW, Omicron Laserage, Germany) and 473/488 nm lasers (MBL-FN-473nm, 500 mW, Changchun New Industries Optoelectronics Tech. Co.; PhoxX 488, 60 mW, Omicron Laserage, Germany). A quad-edge dichroic beam splitter (Di01-R405/488/561/635, Semrock) and a quad-band excitation filter (FF01-446/523/600/677, Semrock) were used to remove the laser light before imaging the fluorescence on an electron multiplying CCD camera (EMCCD; DU-885-CS0-#VP, Andor) with an effec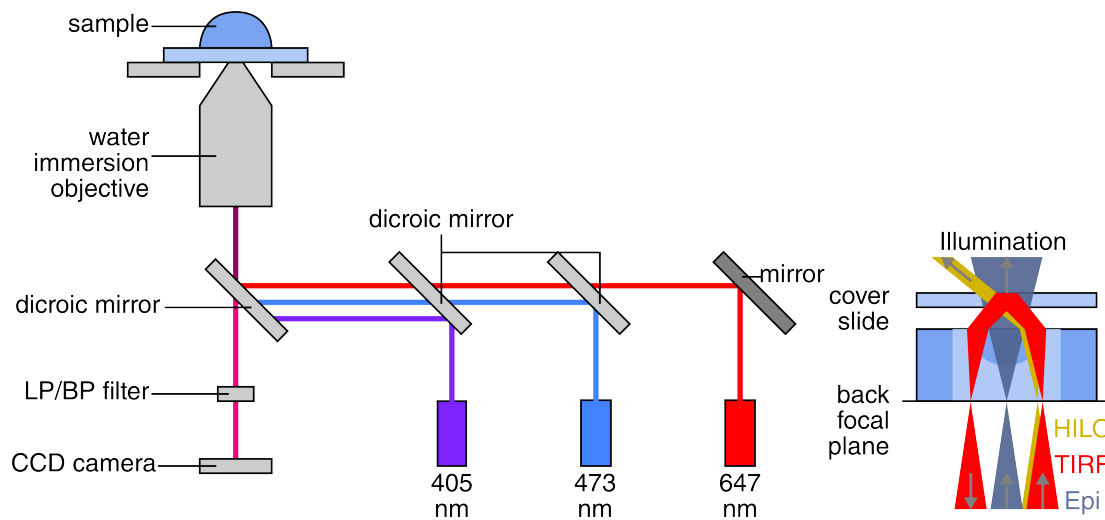tive pixel size of 80 nm. Temperature of camera was -50 °C. Movies typically contained 3,000 - 4,000 images recorded at 30 - 90 Hz.

Figure 12: Simple overview of a common fluorescence microscope setup used for STORM imaging. HILO (highly inclined thin illumination) excitation allows for axonal sectioning.

Buffer

STORM movies were recorded with Alexa 647 labeling. The imaging buffer was 10 mM TRIS containing 100 mM cysteamine hydrochloride (Sigma-Aldrich, M6500), 4.0 mg/mL glucose oxidase (Sigma-Aldrich, G0543), 0.57 mg/mL catalase (Sigma-Aldrich, C40-100MG), and 10 % glucose (Sigma-Aldrich, 49158-1KG-F). Buffer was *modified and adjusted based on* [115] [113] PH was adjusted to the range of pH 8.3 and 8.5 by using 0.3 - 0.5 M NaOH. Chamber wells were completely filled with buffer and sealed air-free by a regular coverslip.

Frame rate

The optimal number of frames used for reconstructing one STORM image was determined by calculating STORM images from different frame numbers. In the progress of this work the number of 3,000 to 4,000 frames was determined as being optimal. Below 3,000 frames per image information are missing. Above 4,000 frames per image no changes are observed. At high frame numbers blinking events get rare and negligible. With an increased recording time, drift increases and resolution decreases. Images at different time points are presented in figure 13.
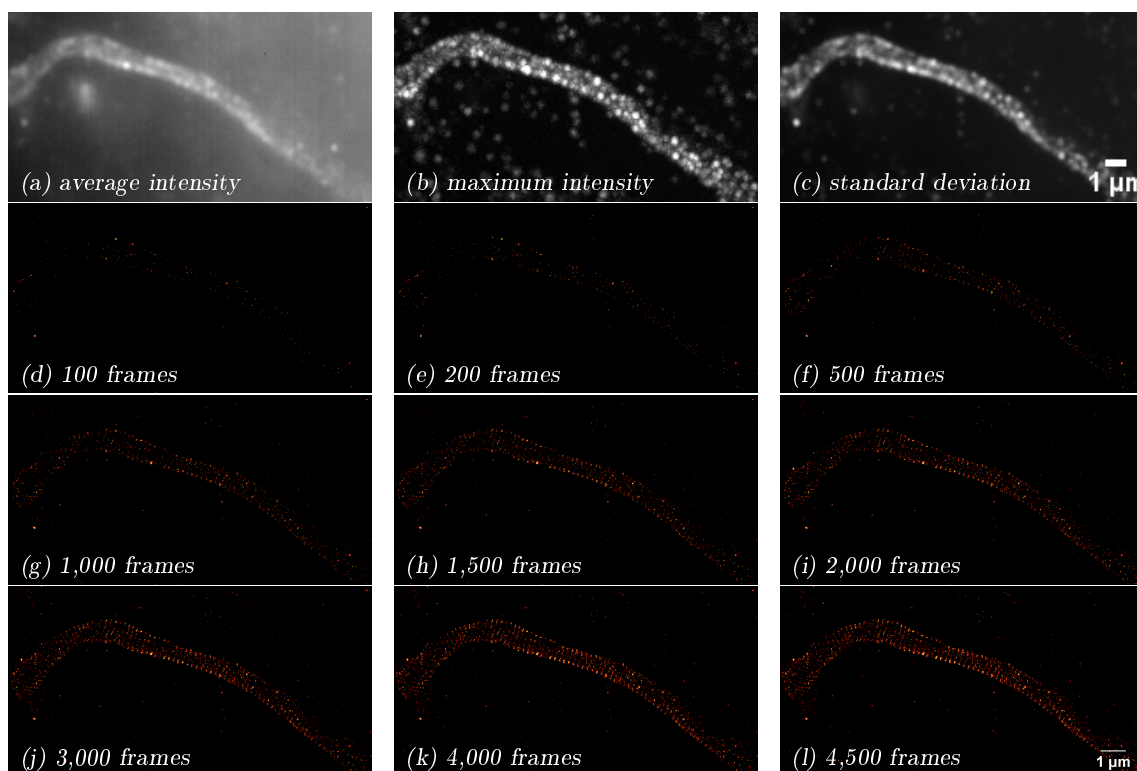
Figure 13: Which frame rate is suitable? The movie was recorded with an exposure time of 0.008 s and 4,700 frames. (a) The average intensity of the complete movie. (b) The maximum intensity of the complete movie. (c) The standard deviation of the complete movie. (d) - (l) STORM images calculated from different numbers of frames. Comparison of 2,000 and 3,000 frames shows structural differences, whereas no differences between 4,000 and 4,500 frames are observed.

Drift

Stability of the setup was determined by using a zero mode waveguide (ZMW). Nanoholes of different sizes were filled with Alexa 647 diluted 10^{-6}. Several movies with different exposure times and number of frames were recorded. The recording conditions, identically to the one of the cellular imaging (method: 3.4.2), 3,000 frames with an exposure time of 0.008 s, did not reveal a measurable drift. For 10,000 frames recording with an exposure time of 0.008 s a drift of about 1.0 pixel, corresponding to 80.0 nm, was determined by principal components analysis (PCA). As a result the drift for cellular STORM images is estimated as 25 to 32 nm.
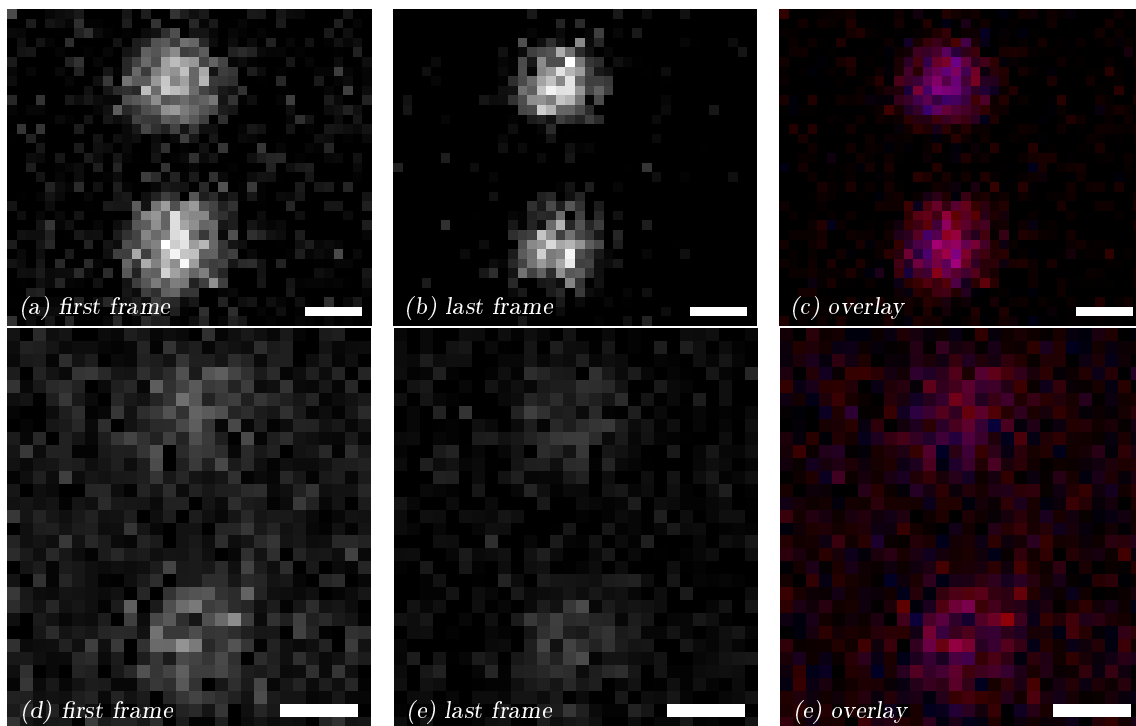
Figure 14: Comparing the first and last frames of movies recorded with an exposure time of 0.008 s. (a) first frame of a 3,000 frame movie. (b) last frame of a 3,000 frame movie (c) overlay of the first (red) and last (blue) frame. (d) first frame of a 10,000 frame movie. (b) last frame of a 10,000 frame movie (c) overlay of the first (red) and last (blue) frame. Scale bar: 0.5 μm.

3.5   Data Analysis

In the following section the methods used for analyzing wide-field and STORM data are described.

3.5.1   Wide-field microscopy

Image display

For visualization colors were assigned to channels and images were merged using ImageJ (software: http://imagej.nih.gov/ij/).

Profiles along the axon initial segment

Mean fluorescence intensities were calculated along the AIS using custom written Matlab code. Start of analysis was the soma or first branching point. A segmented line was drawn along the axon until the next branching point or its fluorescence diminishes indicating the end of the AIS. The length $\|\vec{S}_i\|$ of segment i was determined by subtracting the segment ending $\vec{r}_{i+1}$ from its starting point $\vec{r}_i$,

$$\vec{S}_i = \vec{r}_{i+1} - \vec{r}_i = \begin{pmatrix} \Delta x_i \\ \Delta y_i \end{pmatrix}. \tag{1}$$

The intensity along the ith line segment is now given by $I(\vec{r}_i + \lambda \vec{S}_i)$, with $\lambda = [0 \dots 1]$.
For averaging over the AIS width, a normalized orthogonal vector for each line segment, $\vec{S}_i^{\perp}$, was constructed by swapping x and y coordinates and inverting y,

$$\vec{S}_i^{\perp} = \frac{\begin{pmatrix} -\Delta y_i \\ \Delta x_i \end{pmatrix}}{\left\| \begin{pmatrix} -\Delta y_i \\ \Delta x_i \end{pmatrix} \right\|}, \vec{S}_i^{\perp} \vec{S}_i = 0. \tag{2}$$

To average the line segment intensity over five pixels width, corresponding to circa 1.3 μm, the orthogonal vector was multiplied by -2, -1, 0, 1 and 2 and added to the current line segment position $\vec{r}_i + \lambda \vec{S}_i$. The averaged intensity over the five pixel width is then

$$I_{\text{avg}} = \frac{\sum_{j=-2}^{2} I(\vec{x}_i + \lambda \vec{S}_i + j \vec{S}_i^{\perp})}{5}, \lambda = [0 \dots 1] \tag{3}$$

The mean background was determined at an area not occupied by a neuron and subtracted from the complete profile. For the line profiles, the calculated intensities were averaged and plotted as a function of the distance in μm from the soma or first branching point. A cutoff was made at latest at 70.0 μm in distance. The error, plotted as a light area along the profiles, represents the standard error of the mean (SEM). For double labeling e.g. sodium channel subtype $Na_v 1.2$

with Alexa 488 and ankG at its C-terminus with Alexa 647, the segmented line has been drawn in the ankG channel (marker channel) and projected on the $Na_v 1.2$ channel, in order to ensure the analysis of an exactly identically area.
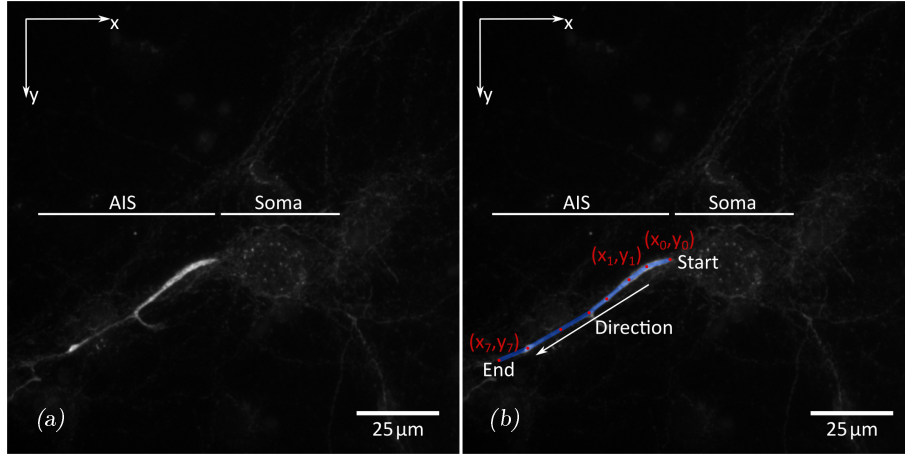
Figure 15: Example for analysis of wide-field images. Pixel location is described by x and y. Identification of soma and AIS. Determine a START (x, y) and END (x7, y7) point of the AIS. Arrow shows direction of analysis. (a) A hippocampal neuron with its soma and AIS. (b) A segmented line (blue) is drawn along the AIS. Segment pieces are shown in red (points).

Bargraphs of mean fluorescence intensity

For bargraphs the mean fluorescence intensity along each AIS was calculated for a distance of 50.0 μm starting from the soma or first branching point. The background of a non-occupied area was determined and subtracted. The average of the region was calculated and plotted using Matlab. The error is the SEM.

Cell-by-cell analysis

From every neuron profiles along the AIS were drawn as described above. The maximum intensity of every profile was determined, max_{AIS}. The mean fluorescence intensity of a defined somatic region was determined, $mean_{soma}$ For every neuron, the maximum fluorescence intensity of the profile was divided by the somatic mean fluorescence intensity. All obtained values (N) were summed and averaged for each maturation stage in order to calculate a factor.

$$factor = \frac{\sum_{i=1}^{N}(max_{\text{AIS}}/mean_{\text{soma}})}{N} \tag{4}$$

3.5.2 STORM microscopy

Image display

The final STORM images were reconstructed by using the Software rapi*d*STORM[122]. For Alexa 647 the PSF FWHM was set as 250 nm. The intensity threshold was chosen as a fixed value of 1,000 ("fixed global threshold"). For image display a fixed minimum localization strength ("minimum localization strength") between 4,000 and 8,000 was chosen. Localizations below this threshold were discarded (details:[122]).

Profiles along the axon initial segment

Relative localization strength profiles were extracted from the AISs using ImageJ (software: http://imagej.nih.gov/ij/). Averaging was performed over ten pixels in thickness, corresponding to 100.0 nm.

Plotting of profiles was performed in Matlab.
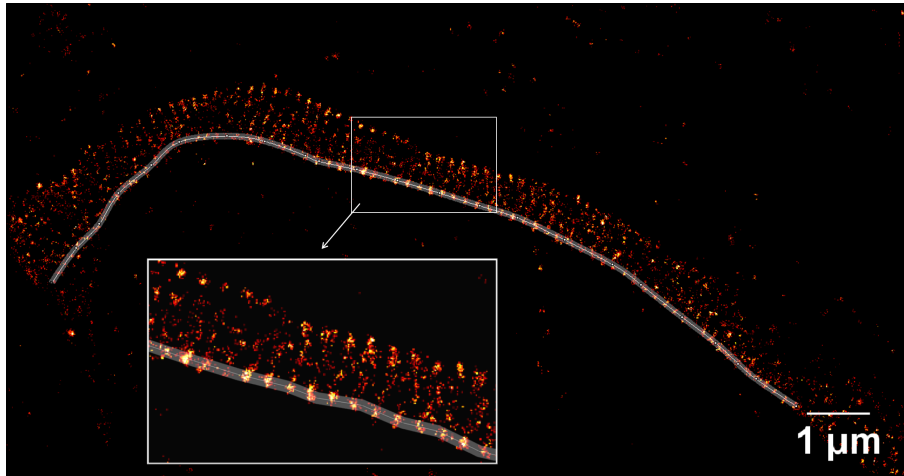
Figure 16: Example for analysis of STORM images. Ten pixel thick segmented lines are drawn along the sides of the AISs. The mean average localization strengths of the ten pixels along the full AIS are extracted. 1.0 µm long example profiles are plotted. Full length data are saved for Fourier analysis (methods: 3.5.2).

Power spectra

The power spectra $P(k)$ were extracted from all line profiles individually by evaluating the amplitude square of their respective Fourier transforms. Each set of power spectra were then averaged as described below. An error estimate for the error of the mean (SEM) for each averaged profile could be determined from the standard deviation directly, due to the stochastical independence of the power spectra.
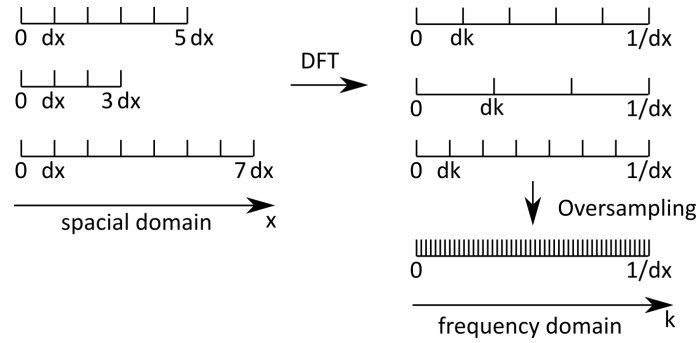
Applying the discrete Fourier transform on the ith line-profile of length L_i results in a Fourier

spacing $\Delta k_i = \frac{1}{L_i}$. To average over line profiles with different Fourier spacing Δk_i, a very fine grid with $\Delta k = \frac{\Delta k_{\min}}{a}$, where $\Delta k_{\min}$ is the smallest Fourier spacing in the respective set of power spectra and a is a factor > 1 that ensures sufficient oversampling (in our case $a = 5$), was chosen. To obtain the values of the power spectra at the new grid points based on the finer Δk spacing, linear interpolation was used. Linear interpolation was sufficient in this case, because even the coarsest grid spacing observed in the data sets is much finer than the discussed features in the power spectra.

This averaging method was preferred over the "sliding window" technique to avoid any bias from different window lengths of the line profiles while accounting for the full amount of data.

For comparison of different power spectra, normalized power spectra $\tilde{P}$ were used, where the normalization was performed over the complete frequency space,

$$\tilde{P}(k) = \frac{P(k)}{\sum_k P(k)\Delta k} \, . \tag{5}$$

Figure 17: Discrete Fourier transforms of data over different lengths in the spacial domain result in differently spaced frequency domains. Averaging of multiple discrete Fourier transforms is performed via interpolation over an oversampled frequency domain.

4 Axon initial segment maturation in hippocampal neurons

The maturation of the AIS was studied by characterizing the density of the cytoskeletal proteins, βIV-spectrin and ankG, and VGSCs, including specifically the subtypes $Na_v 1.2$ and $Na_v 1.6$. The protein density was determined as a function of fluorescence intensity in the AIS of neurons in culture by immunohistochemistry and wide-field microscopy. The time of studying neuronal maturation was limited to their electrophysiologically determined mature stage of three weeks.

4.1 Results

βIV-spectrin, ankG and VGSCs are significantly detected in the AIS.

A high fluoresence intensity is detected at the AIS, when labeling against βIV-spectrin at a N- and C-terminal region (figure: 19 and 18). A weak dendritic fluorescence intensity is detected. It is about 50 a.u. for N-terminal and about 20 a.u. for C-terminal labeling (determined in week 2, background subtracted).

A high label density is observed at the AIS, when labeling against ankG at a N- and C-terminal region (figure: 21). A weak, but pronounced dendritic staining is observed by C-terminal labeling. The mean fluorescence intensity at the AIS (figure: 21, *DIV 12*) is about 13,000 a.u., whereas dendrites have a mean fluorescence intensity of about 3,600 a.u., corresponding to 27.7 % of axonal (discussed in: 9.1.1).

Anti-panNa$_v$ labeling reveals a high label density at the AIS (figure: 23). Within the first week the neurons have a low amount of short branches. The AIS is short and not fully developed, but clearly identifiable. PanNa$_v$ labeling is not excluded from the soma and dendrites. Especially, in mature neurons, when the amount and size of branches increase, dendrites are noticeably labeled.

The mean fluorescence intensities detected for βIV-spectrin, ankG and VGSC labeling at the AISs increase with maturation.

The mean fluorescence intensity of βIV-spectrin labeled N-terminal doubles from the first to the second week, but does not significantly differ between the second and third week in culture. The mean fluorescence intensity of βIV-spectrin labeled C-terminal increases significantly between the first and second, but also second and third week (profiles: 34a). Both βIV-spectrin antibodies reveal a peak in the fluorescence profile at about 10 to 12 μm from the soma or first branching point. The peak is more pronounced by C-terminal labeling. The area of a detected high mean fluorescence is about 30 μm long.

The mean fluorescence intensity of ankG labeled N- and C-terminal increases from the first to the second and third week of maturation. It peaks in the range of 10 to 12 μm from the soma or first branching point (profiles: 22). Afterward the intensity decreases until it reaches a constant value at about 36 to 38 μm.

The mean fluorescence intensity of panNa$_v$ labeled neurons increases from the first to the second and third week (profile: 24). It reaches a peak at about 10 to 13 μm and a constant plateau at about 55 to 60 μm in distance.

The characteristic course of the profiles derived from βIV-spectrin, ankG and VGSC labeled AISs does not shift in distance from the soma or first branching point with maturation.

Normalization reveals that the area of mean fluorescence intensity increase and decrease found in each profile keeps the same distance from the soma or first branching point over the entire three weeks of studied maturation. This implies that its location and size does not change within the time of studied maturation. (figure: 25).

The mean fluorescence intensities of somatic regions and profiles derived from AISs increase simultaneously with maturation.

A detailed cell-by-cell study was performed (as in figure: 27). Thereby, the mean fluorescence intensity of a defined somatic region and the AIS of numerous neurons were determined. The somatic mean fluorescence intensities increase with maturation. This increase is more pronounced between *DIV 7* and *14* than between *14* and *21*. The difference between the profiles derived from the AISs at *DIV 7* and *14* is higher as between *14* and *21* (comparable with the complete averaged data set in figure 24). The trends in the somatic compartment and at the AISs correspond. In both cases the mean fluorescence intensities increase. The factor of the mean maximal fluorescence intensity at the AIS versus the soma is found in the range 8.97:1 for *DIV 7* and 4.98:1 for *DIV 21/21*. From *DIV 7* to *20/21* the proportion of AIS versus soma channel density decreases.

Sodium channel subtype Na$_v$1.2 is detected early on. Sodium channel subtype Na$_v$1.6 is not detected before the second week of neuronal maturation.

For sodium channel subtype Na$_v$1.2 a bright AIS staining is detected from *DIV 6* on (figure: 30). In most cases the subtype Na$_v$1.6 is not detected significantly in the AIS within the first week (figure: 28). Exception, in very dense cultures an AIS staining is observed. Starting at *DIV 10* a bright AIS staining is detected. The profile is smooth over the entire analyzed distance. Additionally, a bright regional nuclei and weaker somatic staining is detected for all time points of

studied maturation.

**The mean fluorescence intensities detected at the AISs labeled for sodium channel subtypes Na$_v$1.2 and Na$_v$1.6 increase with maturation.**

For sodium channel subtype Na$_v$1.2 the mean fluorescence intensity increases from the first to the third week. Within the first two weeks the intensity peaks in the range of 5 - 20 µm. In the third week the mean fluorescence intensity constantly decreases with distance from the soma or first branching point (figure: 31).

For sodium channel subtype Na$_v$1.6 the mean fluorescence profile at *DIV 10* is relatively weak. The profile is smooth and has no distinct maximum (figure: 29). At *DIV 19* and *24* the mean fluorescence is high in the range of about 5 to 55 µm, but has no distinct peak. It doubles from *DIV 10* to *19*. Between *DIV 19* and *24* it increases about 300 % within five days.
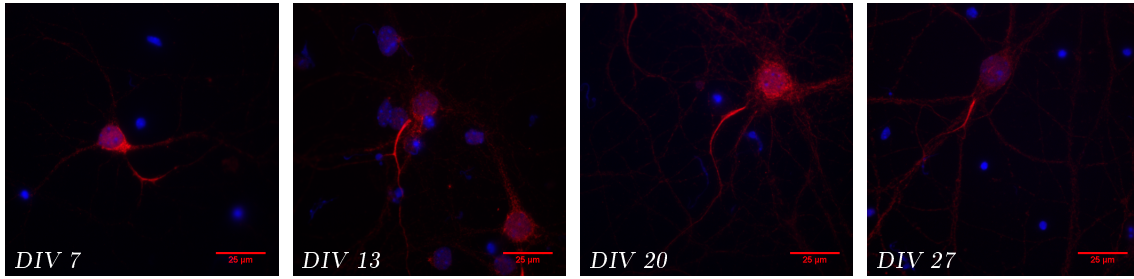
Figure 18: βIV-spectrin (red) labeled at its N-terminus at *DIV 7, DIV 13, DIV 20* and *DIV 27*. Nucleus stained by DAPI (blue). Scale bar: 25.0 μm.
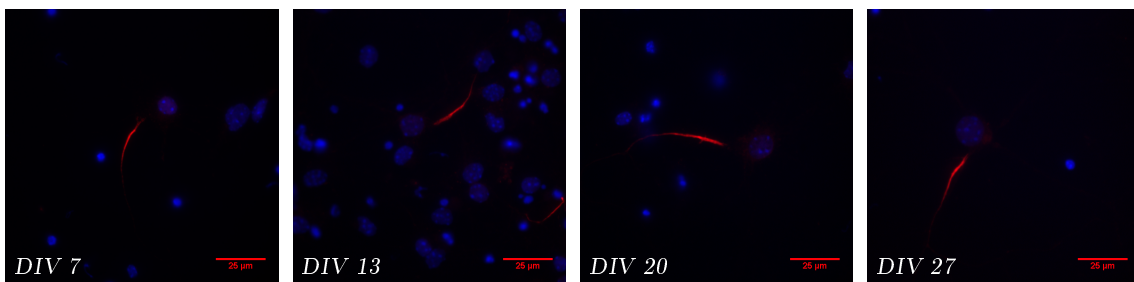
Figure 19: βIV-spectrin (red) labeled at its C-terminus (antibody gift from *Rasband lab, Baylor College of Medicine*) at *DIV 7, DIV 13, DIV 20* and *DIV 27*. Nucleus stained by DAPI (blue). Scale bar: 25.0 μm.
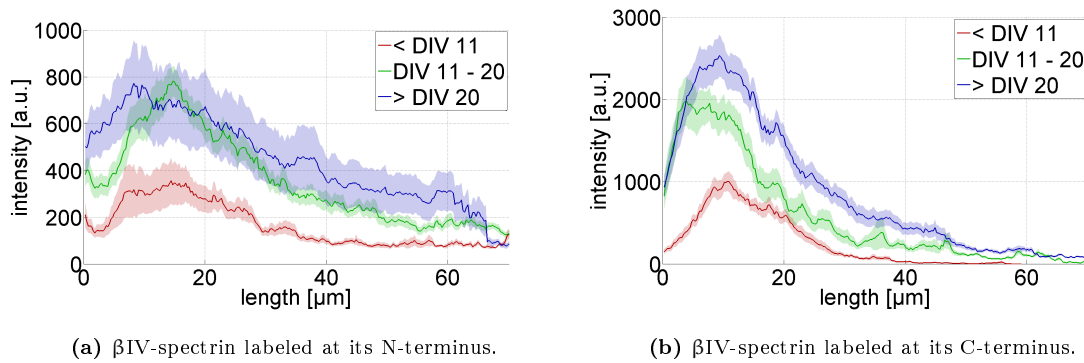
(a) βIV-spectrin labeled at its N-terminus.

(b) βIV-spectrin labeled at its C-terminus.

Figure 20: βIV-Spectrin in development. Profiles show the mean fluorescence intensities [a.u.] along the AIS as a function of distance from the soma or first branching point at several time points within the first, second and third week in development. (a) βIV-Spectrin N-terminal labeled. N = 24, 20, 22. (b) βIV-Spectrin C-terminal labeled (antibody gift from *Rasband lab, Baylor College of Medicine*). N = 24, 18, 35. Error is the SEM.
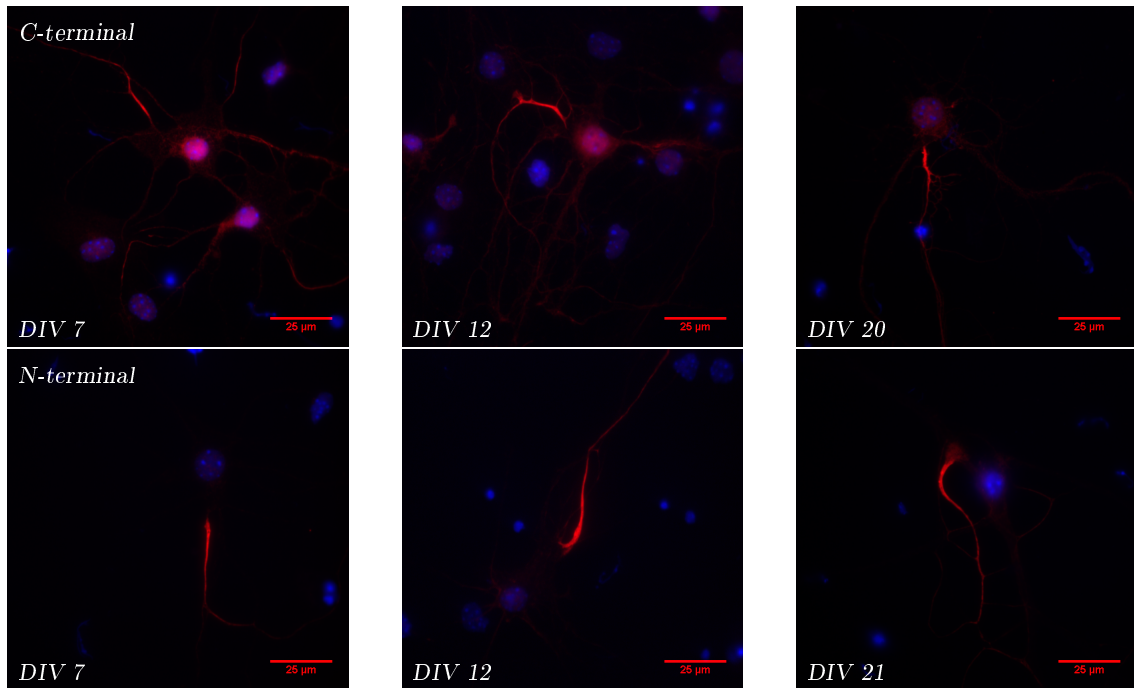
Figure 21: AnkG (red) labeled at its C-terminus (C-terminal antibody, sc-28561, 11.2) (top) and N-terminus (bottom) at *DIV 7, DIV 12* and *DIV 20/21*. Nucleus stained by DAPI (blue). Scale bar: 25.0 μm.

(a) AnkG labeled at its C-terminus.
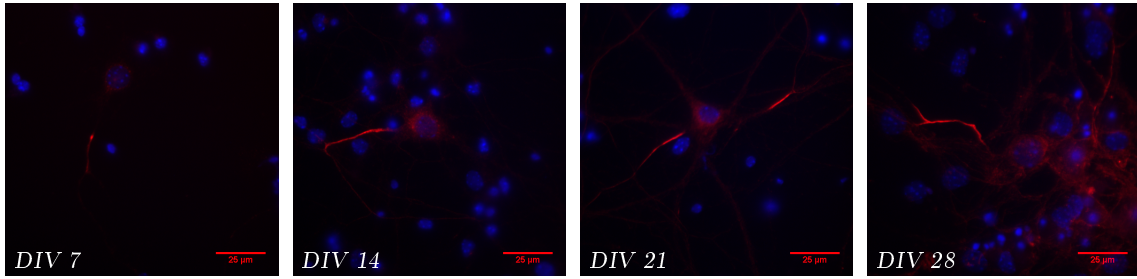

(b) AnkG labeled at its N-terminus.
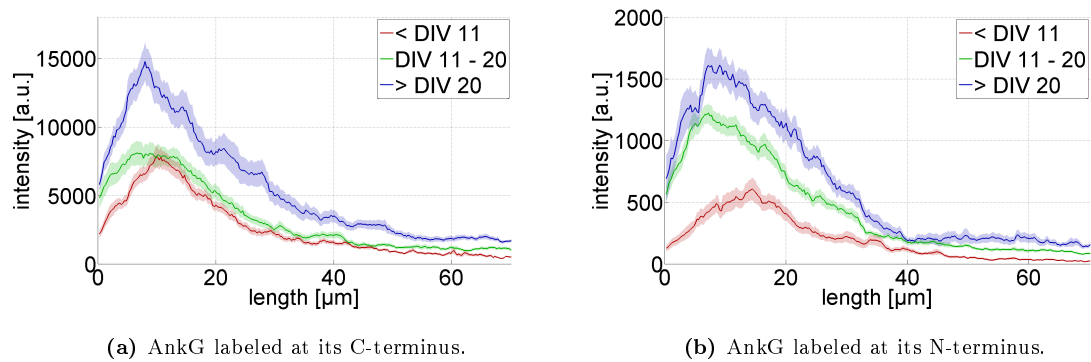
Figure 22: Ankyrin-G in development. Profiles show the mean fluorescence intensities [a.u.] along the AIS as a function of distance from the soma or first branching point at several time points within the first, second and third week in development. (a) AnkG C-terminal labeled (C-terminal antibody, sc-28561, 11.2). N = 41, 39, 37. (b) AnkG N-terminal labeled. N = 23, 43, 26. Error is the SEM.

Figure 23: Voltage-gated sodium channels (red) at *DIV 7, DIV 14, DIV 21* and *DIV 28*. Nucleus stained by DAPI (blue). Scale bar: 25.0 μm.
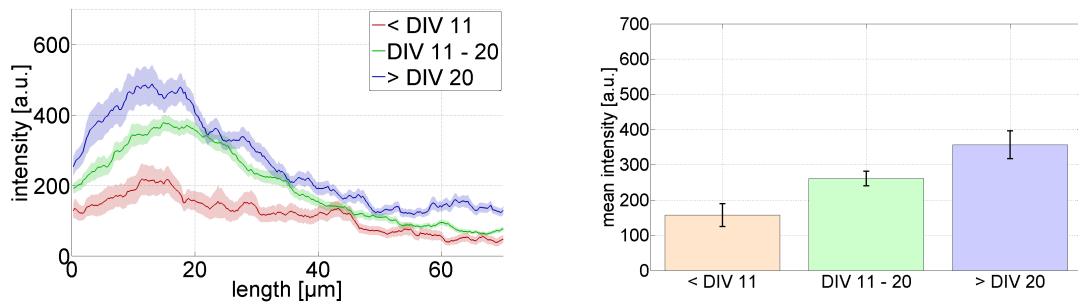
(a) All voltage-gated sodium channel subtypes: Mean fluorescence intensities [a.u.] along the AIS.

(b) All voltage-gated sodium channel subtypes: Mean fluorescence intensities [a.u.]   at the AIS within the distance 0 - 50.0 μm from the soma or first branching point.

Figure 24: Voltage-gated sodium channels in development. (a) Profiles show the mean fluorescence intensities [a.u.] along the AIS as a function of distance from the soma or first branching point at several time points within the first, second and third week in development. (b) Bargraphs show the mean fluorescence intensities [a.u.] at the AIS within the distance 0 - 50.0 μm from the soma or first branching point within the first, second and third week in development. N = 39, 168, 73. Error is the SEM.
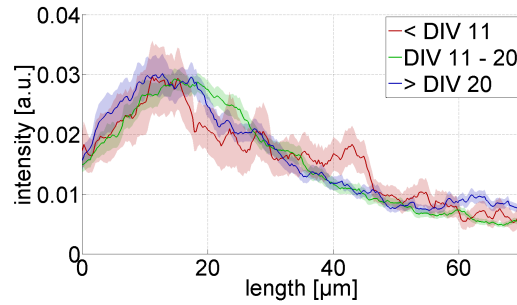
Figure 25: Voltage-gated sodium channels in development. The question if VGSCs change their relative position in the AIS with maturation is determined by normalizing the area below the obtained mean profiles (results: 24) to one. The courses of the profiles do not change and the profiles do not shift within the three weeks of studied maturation. The region of high mean fluorescence intensity does not change with maturation. Error is the SEM.

(a) *DIV 8*

(b) normalized *DIV 8*

(c) *DIV 14*

(d) normalized *DIV 14*

(e) *DIV 21*

(f) normalized *DIV 21*
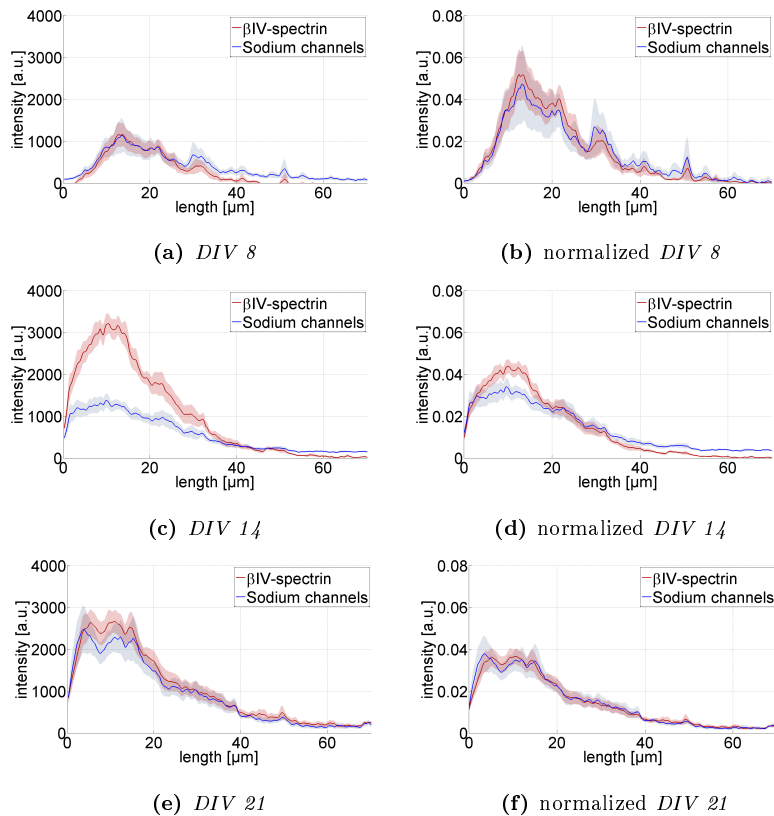
Figure 26: Voltage-gated sodium channels and βIV-spectrin colocalize in maturation. Double stainings of VGSCs and βIV-spectrin (antibody gift from *Rasband lab*, *Baylor College of Medicine*) were performed. Profiles were extracted at three time points: (a) Profiles at *DIV 8*, (c) Profiles at *DIV 14*, (e) Profiles at *DIV 21*. Normalization of the profiles reveals a similar course and areas of high mean fluorescence intensity: (b) Normalized profiles at *DIV 8*, (d) Normalized profiles at *DIV 14*. (f) Normalized profiles at *DIV 21*. N = 10, 11, 12. Error is the SEM.
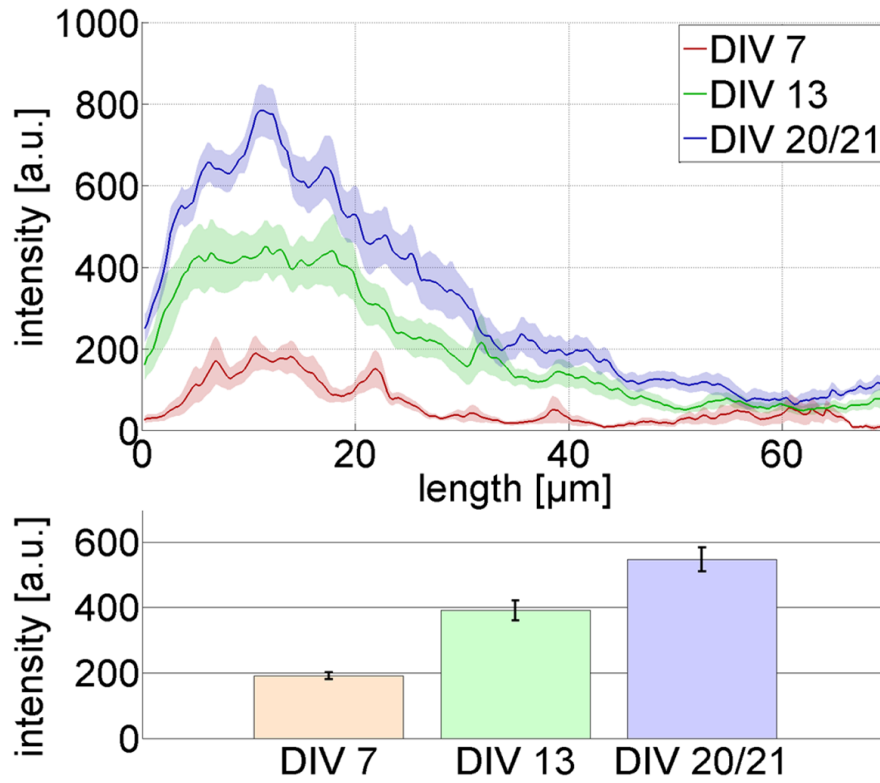
Figure 27: Voltage gated sodium channels labeled by anti-panNa$_v$ and analyzed cell-by-cell in the AIS and soma. Neurons are *DIV 7*, *DIV 13* and *DIV 20/21*. (Top) Profiles show the mean fluorescence intensities [a.u.] along the AIS as a function of distance from the soma or first branching point at three time points. (Bottom) The mean fluorescence intensities [a.u.] for defined somatic regions of the neurons are plotted as bars. The factor of the maximum mean intensity along the AIS versus mean intensity at the soma (factor = intensity (mean max. (AIS)/ mean (soma))) is 8.97 at *DIV 7*, 7.86 at *DIV 13*, and 4.98 at *DIV 20/21*. N = 6, 8, 10. Error is the SEM.

.
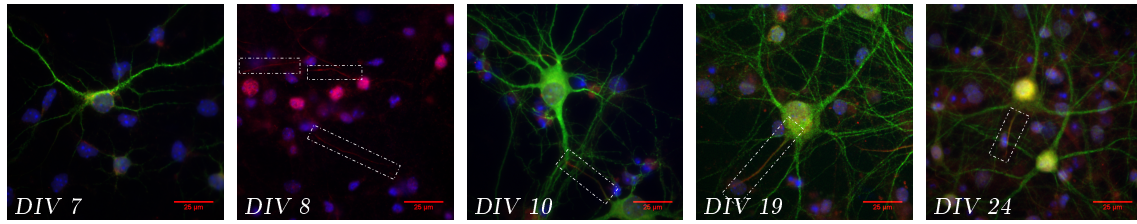
Figure 28: Voltage-gated sodium channel subtype $Na_v1.6$ (red) (boxed) at *DIV 7, DIV 8, DIV 10, DIV 19* and *DIV 24. DIV 7* shows a sparse culture, no significant labeling of subtype $Na_v1.6$ at the AIS. *DIV 8* shows a dense culture and a significant labeling of subtype $Na_v1.6$ at the AIS. At *DIV 10* AISs are mostly $Na_v1.6$ positive. Double labeled with the marker MAP2 (green) at *DIV 10, 19* and *24* highlights the AIS. Nucleus stained by DAPI (blue). Scale bar: 25.0 μm.

(a) Sodium channel subtype $Na_v1.6$: Mean fluorescence intensities [a.u.] along the AIS.

(b) Sodium channel subtype $Na_v1.6$: Mean fluorescence intensities [a.u.] at the AIS within the distance 0 - 50.0 μm from the soma or first branching point.
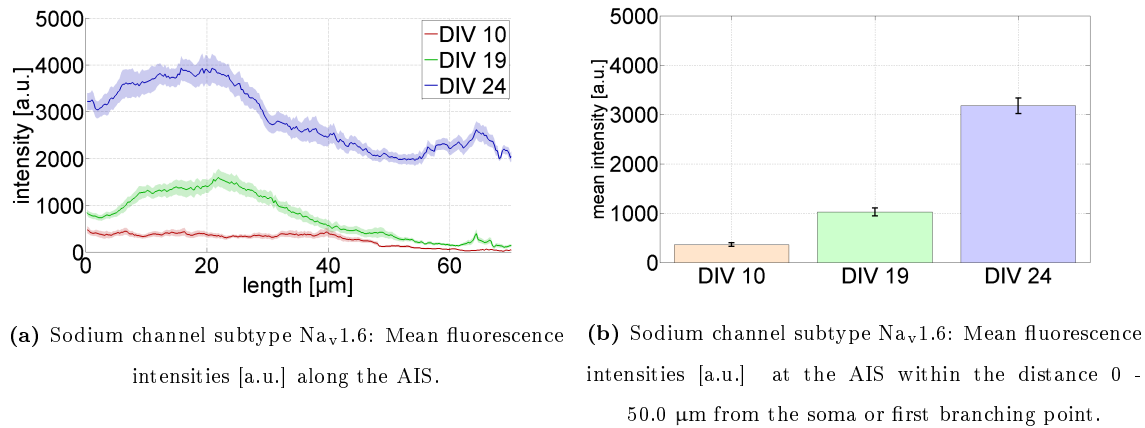
Figure 29: Voltage-gated sodium channel subtype $Na_v1.6$ in development. (a) Profiles show the mean fluorescence intensities [a.u.] along the AIS as a function of distance from the soma or first branching point at several time points within the second, third and fourth week in development. (b) Bargraphs show the mean fluorescence intensities [a.u.] at the AIS within the distance 0 - 50.0 μm from the soma or first branching point within the second, third and fourth week in development. N = 15, 22, 33. Error is the SEM.
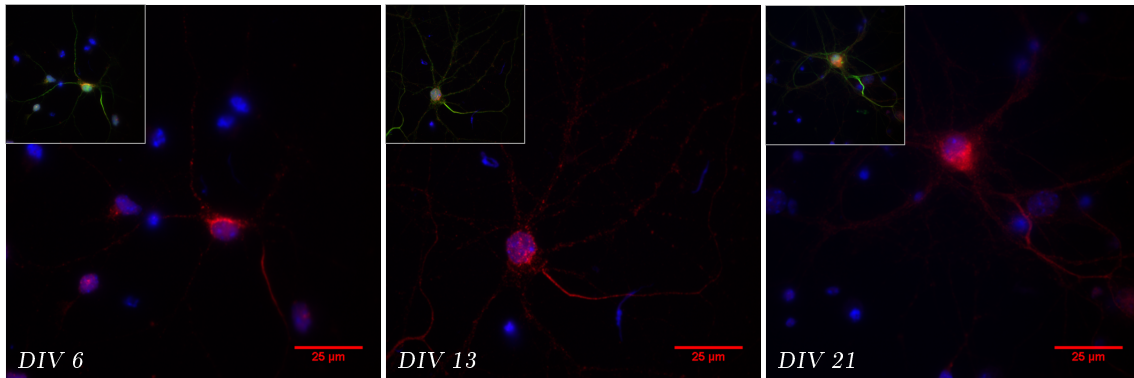
Figure 30: Voltage-gated sodium channel subtype Na$_v$1.2 (red) at *DIV 6*, *DIV 13* and *DIV 21*. Top left: Neurons are shown in double labeling with the marker ankG (labeled at its C-terminus, sc-28561, 11.2) (green) for the identification of the AIS. Nucleus stained by DAPI (blue). Scale bar: 25.0 μm.
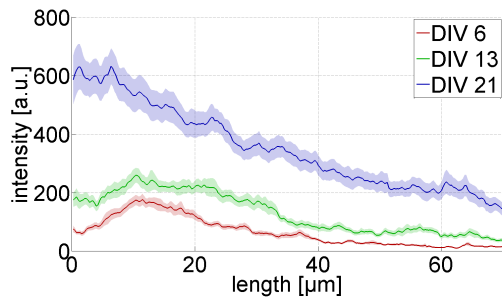
(a) Sodium channel subtype Na$_v$1.2: Mean fluorescence intensities [a.u.] along the AIS.
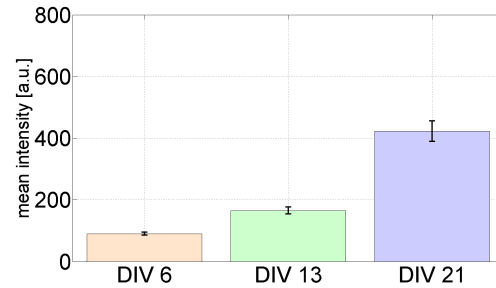
(b) Sodium channel subtype Na$_v$1.2: Mean fluorescence intensities [a.u.] at the AIS within the distance 0 - 50.0 μm from the soma or first branching point.

Figure 31: Voltage-gated sodium channel subtype Na$_v$1.2 in development. (a) Profiles show the mean fluorescence intensities [a.u.] along the AIS as a function of distance from the soma or first branching point at several points within the first, second and third week in development. (b) Bargraphs show the mean fluorescence intensities [a.u.] at the AIS within the distance 0 - 50.0 μm from the soma or first branching point within the first, second and third week in development. N = 26, 24, 34. Error is the SEM.

4.2 Discussion

βIV-spectrin, ankG, and VGSC are enriched in the AIS and mature simultaneously.
βIV-spectrin, ankG and VGSCs are significantly detected in the AIS from the first week on. It is concluded that the proteins are highly enriched in the AIS (as described before:[76],[7],[17]). Profiles, which report the mean fluorescence intensities along the AISs for three mature stages, reveal an increase of the mean fluorescence intensity with maturation. This allows to conclude that the detected proteins increase in their density in the AIS with maturation. Since the mean fluorescence intensity between the second and third week of maturation still increases, it is likely that the proteins are not fully expressed within the three weeks of studied maturation. Exception, βIV-spectrin labeled N-terminal reports a doubling of the mean fluorescence intensity from the first to the second week, but no significant difference between the second and third week. This antibody suggests that the majority of βIV-spectrin is placed in the AIS network in early maturation.
Normalization (details: 4.1) of the profiles reports that none of the proteins shifts in distance from the soma or first branching point within the three weeks of studied maturation. Thus, a shift of the localization of the proteins along the AIS with maturation is unlikely. βIV-spectrin, ankG, and VGSCs are likely to be stabilized within a defined region.
The coexpression and overlapping placement in the AIS of βIV-spectrin, ankG and VGSCs support the role of βIV-spectrin and ankG to stabilize and local enrich VGSCs within a defined region in the AIS.[86]

Chronological expression and differential roles of βIV-spectrin isoforms - βIV$\sum$1 and βIV$\sum$6.
N-terminal labeling of βIV-spectrin shows no significant increase of the mean fluorescence intensity after the second week. C-terminal labeling shows a constant increase of the mean fluorescence intensity over the entire three weeks. Consequently, as mentioned above, does the N-terminal antibody suggest that the majority of βIV-spectrin is placed in the AIS in early maturation, whereas the C-terminal antibody does not suggest a certain maturation stage, where βIV-spectrin is mainly placed in the AIS network. This controversy was examined more closely by performing database research and double labeling experiments on neurons with the N- and C-terminal antibodies.
The database research revealed that the spectrin splice variant 1, referred to as βIV$\sum$1, is targeted by the N- and C-terminal antibody. Only the C-terminal antibody targets an epitope located in βIV$\sum$6. Additionally, the double labeling experiments prove that N- and C-terminal antibodies target different βIV-spectrin isoforms (results: 59, 60). Together these findings suggest that βIV$\sum$1 appears early, whereas βIV$\sum$6 appears later in maturation. Late expression of βIV$\sum$6 has

been described before.[16] Moreover, the results confirm βIV∑1 as a main stabilizer, as described in:[14][15][16][18]. Further, the late expression of βIV∑6 suggests that this isoform might play a major role in VGSC recruitment and even stabilization in the AIS with neuronal maturation.

Na_v1.2 and Na_v1.6 channels are enriched in the AIS and their density increases with maturation. The channel subtypes are enriched at different regions along the AIS. A matural switch from Na_v1.2 to Na_v1.6 channels is not found.

Some cultures (*DIV 8*) displayed neurons, which are strongly positive for Na_v1.6 channel labeling, whereas other cultures (*DIV 7*) revealed not a single neuron with an AIS positive for Na_v1.6 channel labeling. These results suggest the absence and enrichment of Na_v1.6 channels in young neurons. One explanation is the culture density. In most cases no AISs positive for Na_v1.6 channel labeling were found in the first week. The few cultures, which displayed neurons with AISs positive for Na_v1.6 channels in the first week, are very dense. This supports previous observations that neurons in very dense culture mature faster. Furthermore, due to high culture density, these cultures cannot be studied over three weeks of maturation.

Finally at *DIV 10*, a significant fluorescence intensity is observed at the AIS of all neurons. The mean fluorescence profile has a low intensity and appears smooth (figure: 29). This suggests that the Na_v1.6 channels are weakly expressed and evenly distributed along the AIS in early maturation. The high mean fluorescence intensity increase between *DIV 19* and *24* allows to conclude that the density of Na_v1.6 channels highly increases. Moreover, Na_v1.6 channels are mainly found in the AIS of mature neurons (as described before:[99][8]) At *DIV 19* and *24* the mean fluorescence intensity profiles reveal areas of higher and lower intensity, which suggest that Na_v1.6 channels are not evenly distributed in the AIS of mature neurons.

Na_v1.2 are detected in the first week of studied maturation. This allows to conclude that Na_v1.2 channels are expressed early on, as described before:[98][8]. A doubling of the intensity from one to another week suggests that the density of Na_v1.2 channels increases in mature neurons.

In immature neurons an intensity peak at about 10 µm from the soma or first branching point reports Na_v1.2 enrichment. In mature neurons the intensity profile of Na_v1.2 decreases constantly and no intensity peak is observed. Together the findings reveal a proximal Na_v1.2 and distal Na_v1.6 localization in the AIS, as described before:[31]. Moreover, a prominent proximal Na_v1.2 enrichment can be associated with immature neurons and distal Na_v1.6 enrichment can be associated with mature neurons.

The analog increase of Na_v1.2 and Na_v1.6 densities with maturation suggests that there is no replacement of Na_v1.2 by Na_v1.6 with maturation, as observed in noR.[8]

The density of voltage-gated sodium channels increases in somatic regions with maturation.

The mean fluorescence intensity detected by an panNa$_v$ antibody was found to increase in somatic regions with maturation. Anti-panNa$_v$ targets all VGSC subtypes. The subtypes Na$_v$1.2 and Na$_v$1.6 have been found as the main subtypes in the AIS. [31] [25] However, this does not exclude their presence in somatodendritic compartments, as described before[27]. Additionally, other VGSC subtypes, including Na$_v$1.1 and Na$_v$1.3 have been reported in somatodendritic compartments of central neurons (including pyramidal neurons). [123] [69] [26] [3] Here, an increase of the somatic fluorescence intensity is found and allows to conclude that at least one VGSC subtype increases in its density in the somatic compartment of hippocampal neurons with maturation.

No tremendous exceeding of VGSCs in the AIS.

A careful cell-by-cell study with anti-panNa$_v$ labeled neurons was performed. Single neurons were analyzed, whereby the factor from the mean maximal fluorescence intensity at the AIS versus the soma was determined. The relation of the mean fluorescence intensity derived from the AIS and soma is in the range 4.98:1 to 8.97:1. This suggests a 5 to 9 fold difference between the somatic and AIS VGSC density depending on the matural stages.

Compared with recent studies on differences between AIS and somatic VGSCs, it is difficult to estimate the relevance of the obtained values. Both, low (3 fold)[2] and high (35 to 80 fold)[26] [27] differences of the VGSC densities between the AIS and soma have been reported. Hereby, the finding of a 5 to 9 fold difference would support the theory that the VGSC density in the AIS has no tremendous exceed over the somatic densities. Nevertheless, studies revealing more striking differences cannot be ignored. Hereby, one needs to consider that the studies have been performed by using different methodical approaches. Whereas a small 3 fold difference has been reported by a combined electrophysiology-imaging study, a high 35 to 80 fold difference has been reported based on immunogold labeling experiments. [26] [27] Hereby, methodical drawbacks need to be taken into account. In electrophysiological experiments a patch pipette is used, whereby a part of the membrane is sucked in the pipette, likely that VGSCs lose their connection to the cytoskeleton and the number of VGSCs is underestimated. Freeze fracture experiments with immunogold labeling are not free of false-positive detections. Furthermore, it is unknown if the P-face plasma membrane, used to determine non-specific binding, has the same properties and is unrestricted suitable to determine non-specific binding. Besides general experimental challenges[124] [125], such as varying results due to antibody non-specificity or slightly different experimental protocols, immunohistochemistry studies are likely to under- or overestimate the VGSC densities based on the accessibility of the epitopes. For example, epitopes in somatic and axonal regions could

be unequally easy accessed. Furthermore, the choice of the fluorescence imaging technique is critical. The drawback of the here chosen wide-field microscopy technique is a wide focal plane. Consequently, not only fluorescence from a defined area is collected. A calibration to a defined surface area is impossible. Thus, it is likely that the VGSC density is overestimated based on the detected fluorescence intensity. Additionally, the here applied method (description: 3.5.1) to analyze the data based on the maximum intensity of the AIS and mean intensity of the soma is more likely to over- than underestimate the VGSC density in the AIS. Consequently, when considering all drawbacks of the highly sensitive immunohistochemistry experiments (details in chapter: The specificity of immunohistochemistry 9.1), it is unlikely that the here performed cell-by-cell study underestimates the VGSC density in the AIS versus the soma tremendously. This allows to conclude that the VGSC density in the AIS relative to the soma is likely to be even smaller as presented here.

For every method, especially immunohistochemistry experiments, a careful evaluation is necessary in order to estimate the sensitivity of the method and understand the quality of the drawn conclusions. A detailed evaluation of each antibody was performed and is found summarized in the supplements (chapter: 9.1).

5 Structural organization of axon initial segment components in hippocampal neurons

Additionally, to the maturation study, a structural characterization of βIV-spectrin, ankG and VGSCs in wildtype neurons was performed. Thereby, a focus was on the organization of βIV-spectrin isoforms, βIVΣ1 and βIVΣ6, and VGSC subtypes, $Na_v 1.2$ and $Na_v 1.6$. Neurons were characterized at the age of *DIV 11* to *20* using STORM microscopy.

5.1 Results

βIV-spectrin labeled at its N-terminus and at an epitope located centrally on its sequence displays a regular organization.

Recorded images (figure: 32) show a periodically organized structure. Localization strength profiles along the AIS reveal six regular peaks for N-terminal and ten regular peaks for central labeling per 1.0 μm. A frequency of about 190 nm is obtained for N-terminal labeling and a doubled frequency of about 91 nm for central labeling.

βIV-spectrin labeled at its C-terminus displays no regular organization in mature neurons.

Recorded images (figure: 32) of mature neurons show no organized structure. The localization strength profile reveals six irregular peaks per 1.0 μm. No distinct frequency is obtained.

From additional experiments, performed on immature neurons (*DIV 6*), images of structured AISs were obtained (figure and results: 5.1). Localization strength profiles reveal six regular spaced peaks. The power spectrum has a broad peak with a frequency of 192 to 200 nm. The periodic organization is prominent, but less as observed for N-terminal and central labeling.

AnkG labeled at the spectrin-binding domain is periodically organized.

Images (figure: 34) recorded by N-terminal labeling (spectrin-binding domain) reveal an organized structure of the AIS. The structure is prominent, but less pronounced as the one obtained from βIV-spectrin labeled at its N-terminus. No organized structure is observed on images recorded by C-terminal labeling. The localization strength profile for N-terminal labeling reveals five regular peaks. The peaks have no clear maximum and several shoulders, showing broad localizations. Both profiles obtained by ankG labeled C-terminal are irregular. The calculated power spectrum reveals a high power in the frequency range 188 to 201 nm for N-terminal labeling. The peak has two maxima at the frequencies 192 and 196 nm (and a small shoulder at about 189 nm). No distinct

frequency for C-terminal labeling is obtained.

**VGSCs are (semi-)periodically organized in the AIS. Subtype labeling reports diverse results.**

The recorded images (figure: 35) display (semi-)periodic organization for VGSCs. Anti-panNa$_v$ labeling reveals regional highly periodic and non-periodic segments within a single AIS. Images obtained by Na$_v$1.6 subtype labeling show structured, but not prominent periodically organized AISs. In contrast, images obtained by Na$_v$1.2 appear relative unstructured. Extracted localization strength profiles show broad, but regular spaced localizations for VGSCs and subtype Na$_v$1.6. Five localizations per 1.0 µm are found. The extracted profile for the subtype Na$_v$1.2 shows regions without localizations. This behavior is reflected in the corresponding power spectra. VGSCs have a clear frequency of about 182 nm. The spectrum has low noise. Subtype Na$_v$1.6 has a frequency of about 192 nm. The spectrum is more noisy, especially at high frequencies. Subtype Na$_v$1.2 has a frequency peak at about 178 nm, but at higher frequencies peaks with the same power are found. The entire spectrum appears highly noisy, especially at high frequencies. For a more detailed analysis, the power spectrum of each neuron labeled for Na$_v$1.2 was plotted separately (results: 10.3). The dataset shows two subclasses of spectra: Completely noisy spectra and spectra, which have several frequencies with a high power, including at or close to 200 nm. No neuron has a spectrum with a single peak at or close to the frequency of 200 nm and a low level of noise (results: 10.3).
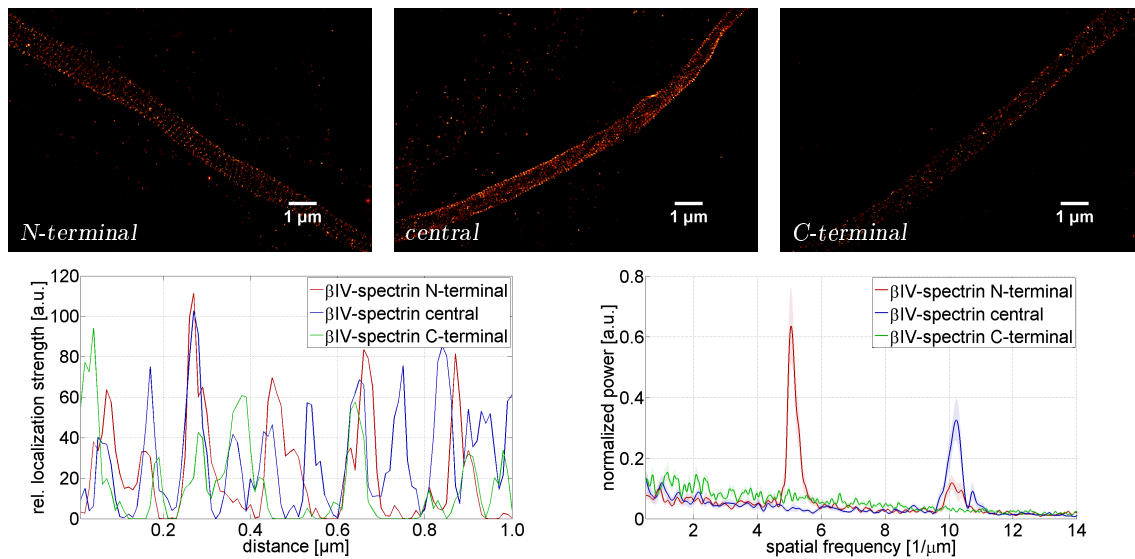
(a) Profiles of 1.0 µm segments extracted from the shown neurons.

(b) Power spectra calculated from the complete βIV-spectrin data sets.

Figure 32: βIV-spectrin organization in the AIS imaged by STORM at *DIV 11 - 20*. Example images of the AIS labeled for βIV-spectrin at an N-terminal, central and C-terminal (C-terminal antibody, sc-131789, 11.2) located epitope. (a) Profiles of 1.0 µm segments extracted from the shown neurons show regularly localizations for N-terminal and central labeling and irregular localizations for C-terminal labeling. (b) Power spectra calculated from the complete βIV-spectrin data sets reveal a periodic organization of about 190 nm for N-terminal labeling and of about 91 nm for central labeling. N(for N-terminal, C-terminal and central) = 24, 30, 18. Error is the SEM.

(a) Profile of 1.0 µm segment extracted from the shown neuron.

(b) Power spectra calculated from the complete βIV-spectrin data sets.
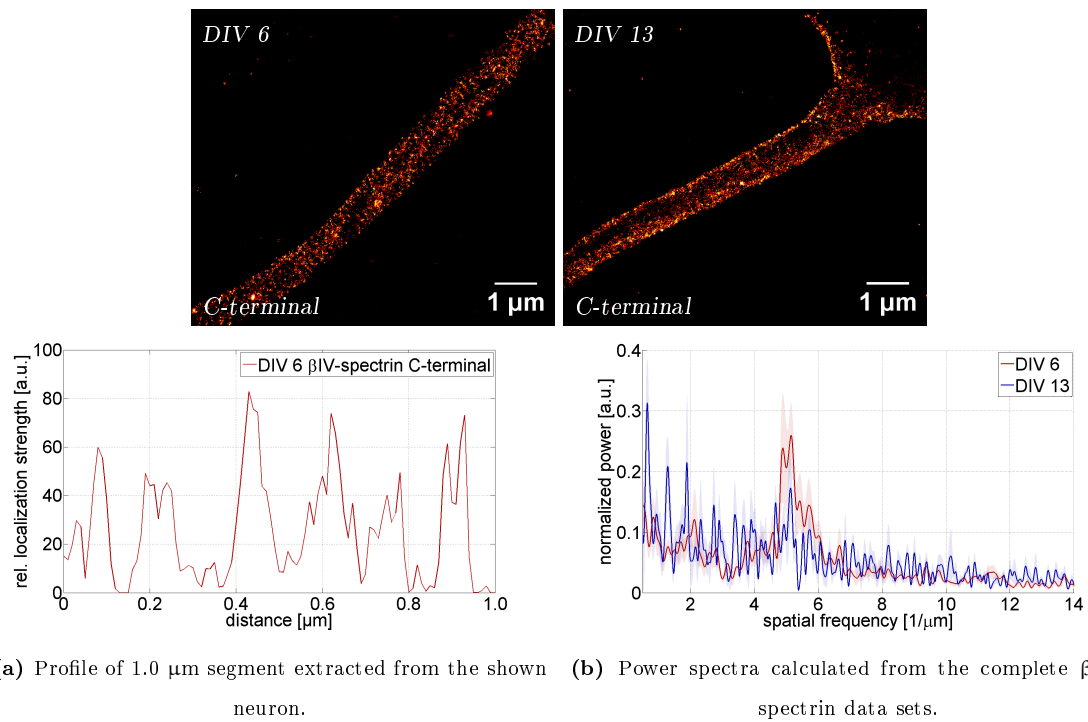
Figure 33: βIV-spectrin organization in the AIS of immature neurons imaged by STORM at *DIV 6* and *13*. Example images of the AIS labeled at a C-terminal (antibody gift from *Rasband lab, Baylor College of Medicine*) located epitope at *DIV 6* and *13*. (a) The profile of a 1.0 µm segment extracted from the shown *DIV 6* neuron shows regular localizations. (c) Power spectra calculated from the complete data sets reaveal a wide, but clear periodic organization of about 192 to 208 nm for *DIV 6* and no organization for *DIV 13*. N(for *DIV 6*, *DIV 13*) = 9, 5. Error is the SEM.

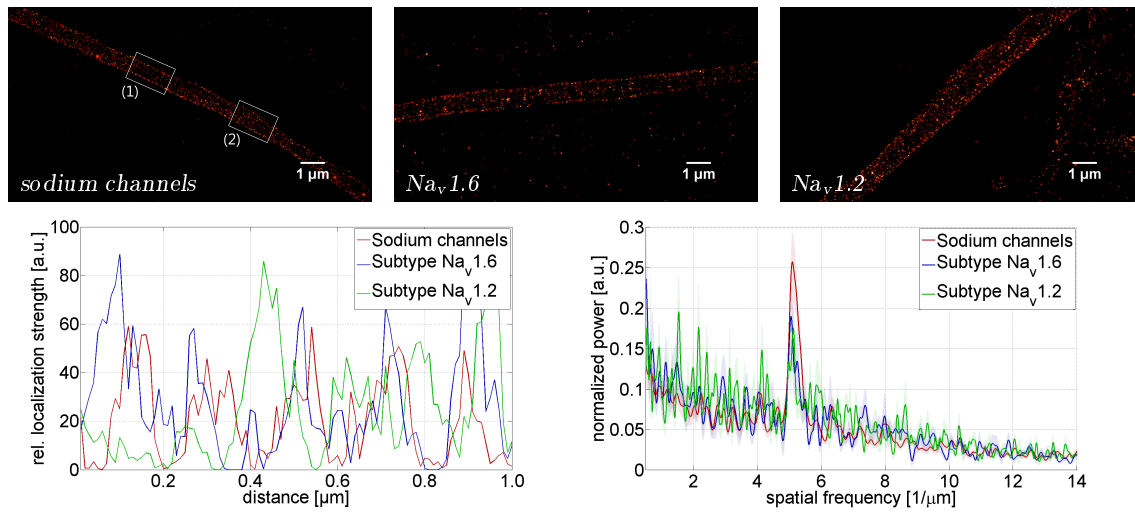**(a)** Profiles of 1.0 μm segments extraced from the shown neurons. **(b)** Power spectra calculated from the complete ankG data set.
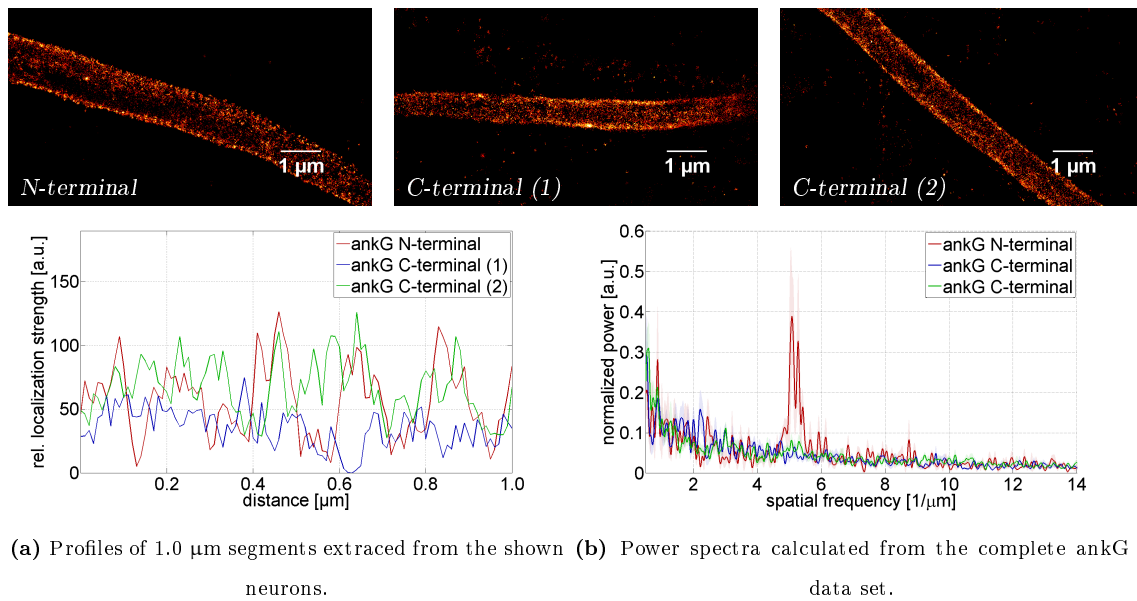
Figure 34: AnkG organization in the AIS imaged by STORM *DIV 11 - 20*. Example images of the AIS labeled for ankG at an N- and two C-terminal located epitopes. (1) C-terminal antibody, sc-28561, 11.2 (2) C-terminal antibody, sc-31778, 11.2. (a) Profiles of 1.0 μm segments extracted from the shown neurons show regular localizations for N-terminal and irregularity for C-terminal labeling. (b) Power spectra calculated from the complete ankG data sets reveal a periodic organization in the range of 188 to 201 nm for N-terminal labeling and no distinct organization for C-terminal labeling. N(for N-terminal, C-terminal (1) and C-terminal (2)) = 5, 12, 15. Error is the SEM.

(a) Profiles of 1.0 µm segments extracted from the shown   **(b)** Power spectra calculated from the complete VGSC,
neurons. $Na_v1.6$ and $Na_v1.2$ data sets.

Figure 35: VGSC organization in the AIS imaged by STORM *DIV 11 - 20*. Example images of the AIS labeled for VGSCs, subtype $Na_v1.6$ only and subtype $Na_v1.2$ only. VGSCs show periodically organized areas (Box (1)) and non-periodically organized areas (Box (2)). (a) Profiles of 1.0 µm segments extracted from the shown neurons show regular localizations for VGSCs and subtype $Na_v1.6$. Irregular localizations are observed for subtype $Na_v1.2$. (b) Power spectra calculated from the complete VGSC, $Na_v1.6$ and $Na_v1.2$ data sets reveal a periodic organization of about 182 nm for VGSCs and 192 nm for $Na_v1.6$. No clear periodic organization is revealed for $Na_v1.2$. N(for VGSCs, $Na_v1.6$ and $Na_v1.2$) = 36, 12, 13. Error is the SEM.

5.2   Discussion

βIV-spectrin N-terminal labeled reports periodic organization.

For N-terminal labeled βIV-spectrin a clear spatial frequency of about 196 nm was obtained. This states that βIV-spectrin is found as periodically organized when labeled at its N-terminus. The obtained results by N-terminal labeling agree with previously published data, where the periodic structure has been described as 190 nm. (figure: 2)[11] Additionally, here the periodic organization is found to be maintained throughout the studied maturation from *DIV 11 - 20*. To conclude, within the period of studied maturation the βIV-spectrin N-terminus is highly organized in the AIS and maintains its position.

βIV-spectrin central labeled confirms its tetrameric structure.

Additionally to previous work, βIV-spectrin was labeled at an epitope located centrally on the βIV-spectrin amino acid sequence. A frequency of about 91 nm was obtained. This frequency corresponds with the tetrameric structure of βIV-spectrin (figure: 2). Each βIV-spectrin tetramer consists of two βIV-spectrin heterodimers. These heterodimers have their N-termini directed towards the actin-adducin rings and form a tetramer through a region close to their C-termini (figure: 2, introduction: 2.2). Consequently, for N- and C-terminal targeting the antibody binding positions on two tetramers overlay with each other and cannot be resolved. For centrally located binding regions, two binding positions at one tetramer are resolved, resulting in the doubled frequency of about 91 nm. Together, the findings obtained by N-terminal and central labeling of βIV-spectrin support the tetrameric structure of the βIV-spectrin molecule.
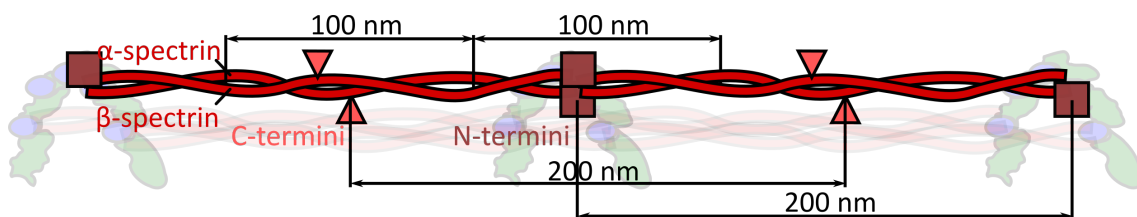
Figure 36: A schematic view of anti-βIV-spectrin antibodies binding to the βIV-spectrin tetramers organized in the AIS. N- and C-terminal binding positions are two overlaying positions, one per heterodimer and thus the distance is about 200 nm. Central located binding positions of heterodimers do not overlay and appear with a distance of about 100 nm.

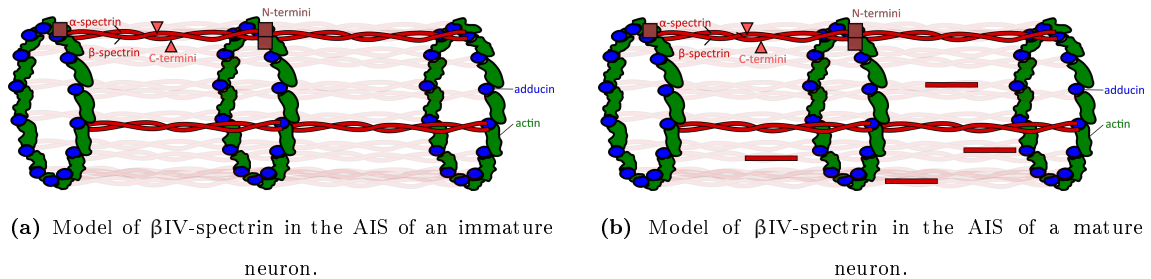**βIV-spectrin C-terminal labeled reports diffuse distribution in mature AIS.**

Based on the tetrameric structure, for C-terminal labeling the same frequency as for N-terminal labeling is expected. Recently, a non-prominent periodic organization in rat neurons (*DIV 12*) has been published and assumed to be due to a freely moving C-terminal region of βIV-spectrin

molecules within the periodic network.[12] These findings have not been investigated further.
Here, experiments with immature and mature neurons were performed. βIV-spectrin labeled C-
terminal in immature neurons (results: 5.1, *DIV 6*) is found to be periodically organized. In
mature neurons no periodic organization is found.

**The obtained results suggest βIV∑6 as a non-periodically organized splice variant
appearing in mature neurons.**
βIV-spectrin has multiple splice variants. Database research and double labeling experiments
reveal that the N- and C-terminal antibodies target different splice variants of βIV-spectrin (results:
60), whereas βIV∑1 is targeted by both antibodies and βIV∑6 only by the C-terminal antibody.
βIV∑1, the main isoform and expressed from early on,[16] [17] is organized in a periodic matter, here
confirmed by labeling experiments at an N-terminal and central located epitope. βIV∑6 has been
described as appearing later in maturation[16]. This suggests that a high density of βIV∑1, but no
or only a low density of βIV∑6, is detected by C-terminal labeling at *DIV 6*. Consequently, similar
structures for βIV-spectrin labeled N- and C-terminal in young neurons are resolved. In mature
neurons an increasing irregularity is detected by C-terminal labeling. It is likely that an increasing
density of βIV∑6 is integrated in the existing network in a non-periodic matter. Summarized,
the findings suggest that a non-periodically organized splice variant, βIV∑6, is the reason for
irregular βIV-spectrin organization detected by C-terminal labeling. Presumably, its non-periodic
organization is due to the lack of an actin-binding domain, which is required for the transfer of the
periodic organization from the underlying network.[126] The theory of a freely moving C-terminal
region of βIV-spectrin is rejected.

(a) Model of βIV-spectrin in the AIS of an immature neuron.

(b) Model of βIV-spectrin in the AIS of a mature neuron.

Figure 37: Model of βIV-spectrin organization in the AIS. Spectrin tetramers connect actin-adducin rings with
each other. (a) Immature neurons consist of αII/βIV∑1-spectrin tetramers, which form a highly organized AIS.
(b) Mature neurons consist of αII/βIV∑1-spectrin tetramers and the additional splice variant of spectrin, βIV∑6.
αII/βIV∑1-spectrin tetramers form a highly structural organized AIS. βIV∑6 lacks an actin-binding domain and
integrates in the existing network in a non-periodic matter.

AnkG organization is mediated by binding to the underlying periodically organized network.

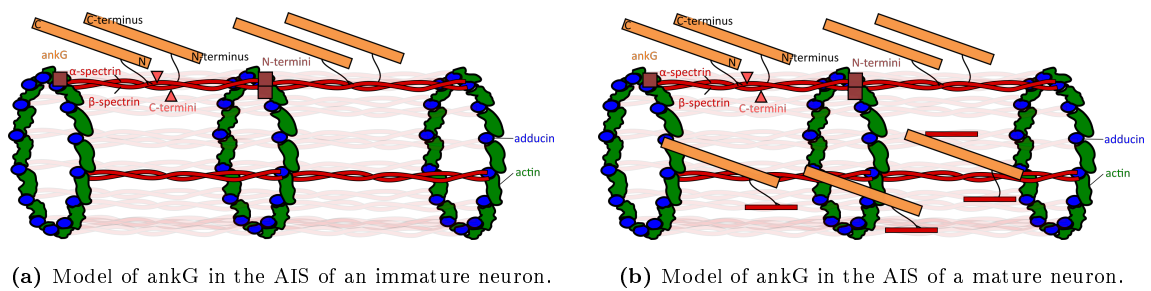AnkG has a spectrin-binding domain and has been found to bind βIV-spectrin. [45] [72] [16] Consequently, it is likely that the periodic organization of the underlying network is transferred to ankG. (figure: 2). The used N-terminal ankG antibody targets the spectrin-binding domain and thus it is most likely to reveal an organized pattern. Here, its organization was found in a frequency range between 188 to 201 nm. This has been lately described for neurons derived from rats. [12] The identified frequency is not surprising. Three factors are likely to reduce the periodic appearance of ankG (in comparison to βIV-spectrin). (i) Since ankG is not a part of the underlying periodic network and has a certain distance to the network, it is likely that the periodic organization is not fully transferred and a less pronounced periodic organization is found. (ii) Additionally, ankG has multiple binding positions on a single βIV-spectrin tetramer, [62] [53] [63] [57] [19] which are located close to each other, but do not overlap. As a consequence, not all available binding sites might be occupied with ankG molecules and not all ankG molecules might be targeted by an antibody (e.g. due to steric hindrance and low affinity). As a result, depending on which positions are targeted and imaged, the distance between two resolved ankG molecules varies, possibly in the range of 160 to 240 nm (figure: 38). The small distance between two ankG binding positions on a single βIV-spectrin tetramer cannot be resolved by STORM microscopy (introduction: 2.6), thus further investigations were not feasible. (iii) Further, βIV∑6 lacks an actin-binding domain [16], but does not lack an ankyrin-binding domain. Thus, especially in mature neurons, where βIV∑6 is likely to be highly expressed, its non-periodic organization is transferred to ankG and a less pronounced organization of ankG is expected to be found.

AnkG labeled C-terminal is found to be non-periodically organized in mature neurons (results for immature neurones: 10.2). This is in agreement with recent findings made in neurons derived from rats. [12] The targeted C-terminal epitope has no proximity to the spectrin-binding domain and thus is less likely to reveal a periodic organization based on the underlying network. Especially, when deliberating that giant ankG is a 480 kDa protein and has a length of nearly 150 nm. [73] 150 nm is about 75 % of the length of a βIV-spectrin tetramer. Consequently, a single ankG molecule has the length of two-thirds of the spacing between two actin-adducin rings connected by βIV-spectrin tetramers. Thus it is likely that the underlying cytoskeletal periodic pattern could only be revealed by C-terminal labeling if all ankG molecules would be organized in the same direction.
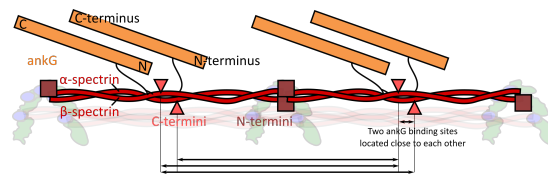
Figure 38: A schematic view of the βIV-spectrin tetramer and its binding sites to ankG. AnkG binds (here shown with its spectrin-binding domain) close to the C-terminal region of the βIV-spectrin tetramer. As a consequence two binding positions are located close to each other. AnkG molecules can differ in distance (demonstrated by arrows): Depending on (i) whether all ankG binding positions on the βIV-spectrin tetramer are occupied or (ii) each ankG is targeted by an antibody.

(a) Model of ankG in the AIS of an immature neuron.

(b) Model of ankG in the AIS of a mature neuron.

Figure 39: Model of ankG organization in the AIS. (a) Immature neurons consist of αII/βIV∑1-spectrin tetramers. AnkG has two organized binding positions at each αII/βIV∑1-spectrin tetramer. (b) Mature neurons consist of αII/βIV∑1-spectrin tetramers and the additional splice variant of spectrin, βIV∑6, which is found as non-periodically integrated. AnkG has two binding positions at each αII/βIV∑1-spectrin tetramer and at least one binding position at each non-periodically integrated βIV∑6 molecule.

VGSC organization is (semi-)periodic.

In VGSCs binding sites to ankG have been identified.[68] [5] The adapter protein ankG and the linker protein βIV-spectrin mediate the contact between the VGSCs and the underlying cytoskeleton (figure: 2). Here, a frequency of about 182 nm for VGSCs is identified. A similar organization has been lately found in neurons derived from rats.[11] Highly periodic and irregular areas are found (figure: 35) within a single AIS. This (semi-)periodic organization is not surprising, since VGSCs bind to ankG. As a consequence, a less pronounced periodic organization of ankG is transferred to the organization of VGSCs. VGSCs have an even (i) further distance to the underlying periodic network than ankG. Additionally, (ii) the adapter protein ankG has multiple binding positions on a single βIV-spectrin, which is likely to result in slight deviations in the distance between two ankG molecules and thus between VGSCs. Also, not all ankG molecules must be necessarily occupied by VGSCs. Further, (iii) the non-periodic organization of βIV∑6 is likely to be transferred to VGSC organization.

(Semi-)periodic Na$_v$1.6 organization confirms findings obtained from VGSCs labeled by anti-panNa$_v$.

So far, studies on subtypes have not been published. Here, a mean frequency of about 192 nm is found for Na$_v$1.6 organization. This confirms the findings obtained within this thesis for the organization of all VGSC subtypes located in the AIS (results: 35) and fits to previously published data[11] obtained in experiments with neurons derived from rats. Locally, the distance between two molecules is found to be higher than about 192 nm (high power at high frequencies in the power spectrum (figure: 35)). The factors (i) to (iii), mentioned above for VGSCs detected by anti-panNa$_v$, play also a role for Na$_v$1.6 organization. Additionally, labeling and imaging artefacts cannot be excluded.

Na$_v$1.2 organization cannot be definitely determined.

Since the subtypes Na$_v$1.6 and Na$_v$1.2 share a common binding motif (figure: 5)[5] the same organization of the two subtypes is expected. The power spectra appear similar and a frequeny of about 187 nm was obtained by labeling for the subtype Na$_v$1.2. This frequency is in the range under the consideration that the ankyrin-binding positions between on the spectrin molecules are closer than 200 nm to each other. Furthermore, the size of ankG molecules mediate a certain distance between the Na$_v$1.2 channels and the periodic network. Nevertheless, the spectrum obtained for Na$_v$1.2 labeling appears highly noisy. Especially, at high frequencies similar power values as at the frequency of 187 nm are found. An analysis cell-by-cell did not reveal more clear results. Thus, the data are not sufficient to subscribe or exclude a (semi-)periodic organization for Na$_v$1.2. Biological and experimental causes are eligible to explain the uncertainty of the data. Biologically, (i) different expression or affinities of the two channel subtypes between *DIV 11* to *20* cannot be excluded. If Na$_v$1.6 expression is higher than Na$_v$1.2 expression, Na$_v$1.6 channels are more likely to occupy binding positions. Experimentally, (ii) localizations for Na$_v$1.2 are likely to miss, due to failures of labeling and imaging. The labeling of VGSC subtypes was found to be challenging. For a final statement additional experiments are necessary (as discussed in 8).

6   Axon inital segment maturation in hippocampal neurons derived from qv^{3J} mutant mice

Impaired information encoding in qv^{3J} mutant hippocampal neurons [3], asked for an investigation of their VGSC density with maturation. Based on the certainty that the qv^{3J} mutation is a frameshift mutation in the cytoskeletal protein βIV-spectrin, abnormalities in AP waveforms are believed to be mediated by defects within the cytoskeletal component βIV-spectrin. Consequently, the expression pattern of βIV-spectrin and adjunct cytoskeletal components is monitored in control (wildtype and heterocygote) and qv^{3J} mutant hippocampal cultures (sibling cultures) over three weeks of maturation.

6.1   Results

βIV-spectrin, ankG and VGSCs are detected with a reduced mean fluorescence intensity in the AIS of qv^{3J} mutant neurons.

Results obtained from labeling control neurons for βIV-spectrin agree with previous experiments (figure: 18, 19). A significant AIS staining is observed over the three weeks of studied maturation using N-terminal and central labeling. βIV-spectrin is weakly, but significantly detected in the AIS of some immature qv^{3J} mutant neurons using N-terminal labeling (figure: 42). After the first week no neurons with a significant AIS staining are found. For central and C-terminal labeling no significant AIS staining is observed at any time point. The bright local somatic staining of the central antibody remains in qv^{3J} mutant neurons (figure: 58).

N- and C-terminal labeling of ankG is significantly detected in the AIS of control and qv^{3J} mutant neurons (figure: 44). The mean fluorescence intensity in the AIS of qv^{3J} mutant neurons is lower as in control neurons.

VGSCs are found in the AIS of control and qv^{3J} mutant neurons. The number of qv^{3J} mutant neurons positive for VGSCs decreases with maturation. Meaning, whereby 92 % show a significant VGSC staining at *DIV 10*, only 34 % show a significant VGSC staining at *DIV 19* (statistics: 40).

---

[3] Previous work: Electrophysiology measurements on control (wildtype/heterocygote) and qv^{3J} mutant neurons were performed by Elinor Lazarov, *Hebrew University of Jerusalem, Israel* during her PhD thesis. Manuscript: (2) Elinor Lazarov, Melanie Dannemeyer, Michael Gutnick, Fred Wolf, Andreas Neef "Reduced Nav channel density in the axon initial segment slows down the action potential onset and impairs high frequency encoding."
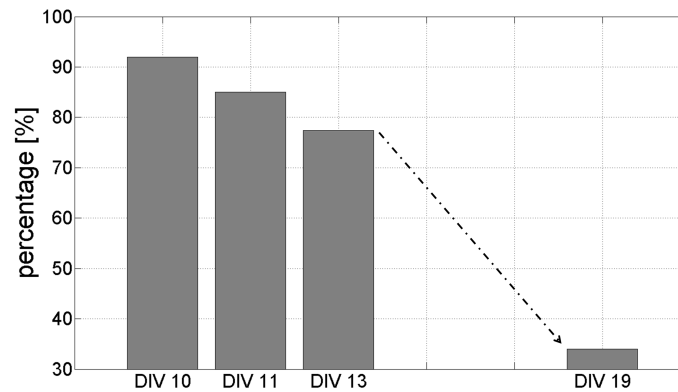
Figure 40: VGSC expression in qv^{3J} mutant neurons. Percentage of ankG positive AISs positive for VGSCs e.g. 92 % at *DIV 10* and 34 % at *DIV 19*. N = 12, 13, 84, 35.

βIV-spectrin, ankG and VGSC: Mean fluorescence intensity does not increase with maturation. The proteins do not locally enrich in the AIS.

Profiles (figure: 43) extracted from control neurons labeled for βIV-spectrin N-terminal and central have the same behavior as previous obtained results from wildtype neurons (results: 34a). With maturation the mean fluorescence intensity increases. In the first and second week it increases strongly, whereas only a small increase from the second to the third week of studied maturation is observed. After the first week the intensity peaks at about 10 - 12 µm from the soma or first branching point. In qv^{3J} mutants βIV-spectrin is not detected after the first week.

In control neurons, ankG labeled C-terminal shows no intensity increase over the three weeks of studied maturation. The mean fluorescence intensity peaks at about 10 - 12 µm. The mean fluorescence intensity of ankG labeled N-terminal shows an increase between the first and second week of studied maturation. Afterward, the mean fluorescence intensity stays constant. A peak is observed at about 10 - 12 µm. The results differ from previous once obtained in the wildtype study (results: 22). AnkG labeled C- and N-terminal in qv^{3J} mutant neurons has no significant mean fluorescence intensity increase in mature neurons. The profiles stay similar and appear relative smooth. A small intensity peak around 10 - 12 µm is observed (figure: 45).

Immature neurons derived from control and qv^{3J} mutant mice show only a small difference of the mean fluorescence intensity using N- and C-terminal ankG labeling. Starting the second week ankG in control and qv^{3J} mutant neurons differs significantly. Whereas, ankG in control neurons is detected with a high fluorescence intensity, stays ankG labeled in qv^{3J} mutant neurons at a constant low fluorescence intensity.

Labeling against VGSCs in control neurons displays the same behavior as observed in previous experiments with wildtype neurons (results: 24). At the AIS, qv^{3J} mutant neurons have a lower mean fluorescence intensity from early on and do not reveal a peak. The profiles, obtained from

VGSC positive neurons, show a constant mean fluorescence intensity with maturation.

Somatic mean fluorescence intensity in the AIS of control and qv^{3J} mutant neurons does not differ.

The mean fluorescence intensity in the AIS increases in control, but not in qv^{3J} mutant neurons with maturation. In qv^{3J} mutant neurons the mean fluorescence intensity stays at a low level. When looking at the mean fluorescence intensity of defined somatic regions in the same neurons the intensity is found to increase in control and qv^{3J} mutant neurons with maturation. Between the groups (e.g. at *DIV 9*) of control and qv^{3J} mutant neurons small, but non-significant differences are observed. A factor (method: 3.5.1) for presenting the relation between AIS and somatic mean fluorescence intensity was calculated. The mean fluorescence intensity in the AIS exceeds the somatic mean fluorescence intensity in control neurons 5 to 9 fold, whereas the exceed in mutant neurons is found at about 3 fold.

**The number of qv^{3J} mutant neurons found $Na_v1.2$ and $Na_v1.6$ positive in the AIS is reduced.**

Control neurons detected positive for ankG labeling are found positive for VGSCs, subtype $Na_v1.2$ and subtype $Na_v1.6$ at *DIV 14* to *21*. Though, at *DIV 13* only about 77.4 % of qv^{3J} mutant neurons are found VGSC positive. At *DIV 14* about 92 % are found positive for subtype $Na_v1.2$. Three days later, at *DIV 17* only 14 % are found $Na_v1.6$ positive.
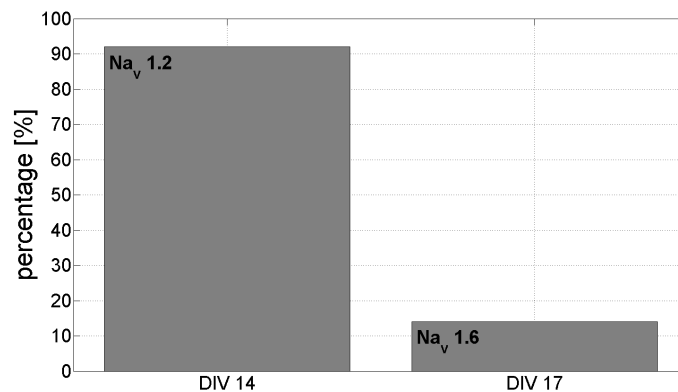
Figure 41: VGSC subtype expression in qv^{3J} mutant neurons. Percentage of ankG positive AISs positive for VGSC subtypes. *DIV 14* neurons were chosen to be tested for $Na_v1.2$ channels and *DIV 17* for $Na_v1.6$ channels based on results obtained from wildtype measurements, which demonstrate that *DIV 14* neurons are highly positive for $Na_v1.2$ channels (results $Na_v1.2$: 30, 31) and older neurons are more likely positive for $Na_v1.6$ channels (results $Na_v1.6$: 28, 29,). 92 % of ankG positive qv^{3J} neurons were found positive for $Na_v1.2$. 14 % of ankG positive qv^{3J} neurons were found positive for $Na_v1.6$. N = 26, 8.
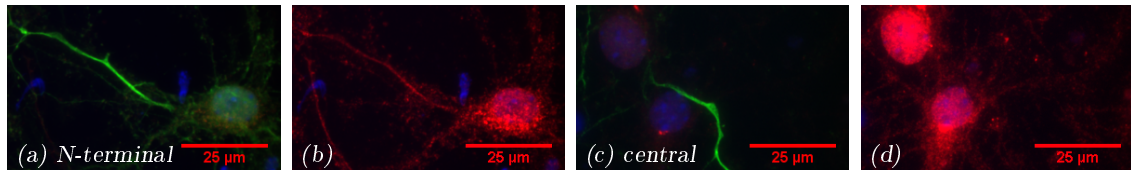
Figure 42: βIV-spectrin (red) labeled at *DIV 7* in qv^{3J} mutant. Double labeling with ankG at its N-terminus (green) in order to identify the AIS. Nucleus stained by DAPI (blue). (a) Merged images of βIV-spectrin labeled at its N-terminus and ankG. (b) βIV-spectrin channel only. Contrast adjusted in order to make AIS visible. The mean fluorescence intensity along the AIS is about 90 a.u. after the subtraction of dendritic fluorescence. (c) Merged images of βIV-spectrin labeled at a centrally located epitope and ankG. (d) βIV-spectrin channel only. Contrast adjusted in order to make potential labeled AIS visible. Scale bar: 25.0 μm.
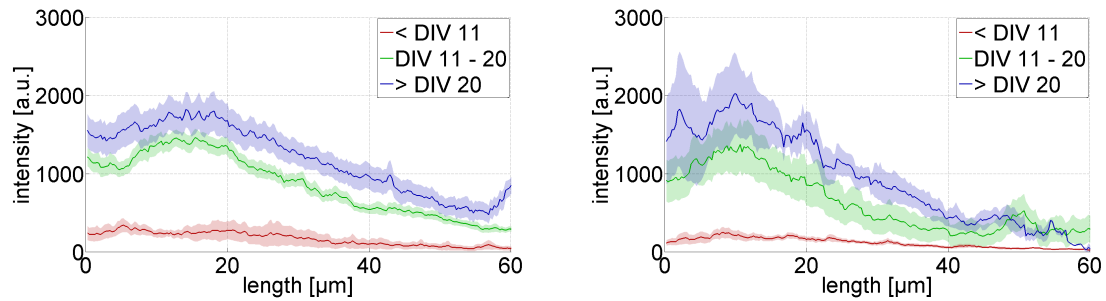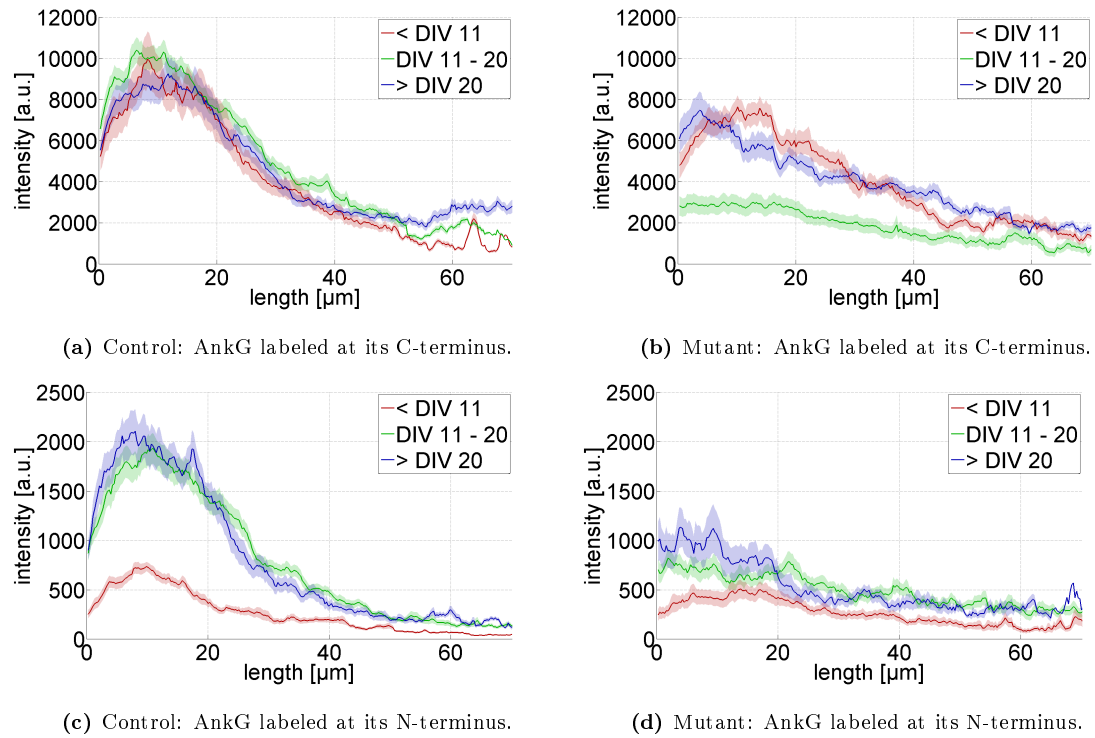

(a) Control: βIV-spectrin labeled at its N-terminus.

(b) Control: βIV-spectrin labeled at a central located epitope.

Figure 43: βIV-spectrin in development. Profiles show the mean fluorescence intensities [a.u.] along the AIS as a function of distance from the soma or first branching point at several time points within the first, second and third week in development. (a) βIV-spectrin N-terminal labeled. N = 6, 42, 27. (b) βIV-spectrin central labeled. N = 11, 20, 9. Error is the SEM.
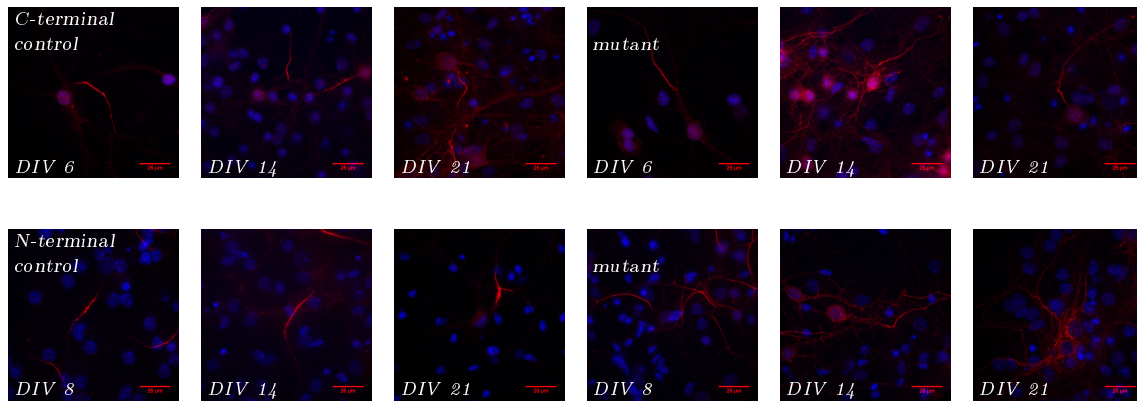
Figure 44: AnkG (red) labeled at its C-terminus (top row) (C-terminal antibody, sc-28561, 11.2) and N-terminus (bottom row) at *DIV 6/8*, *DIV 14* and *DIV 21* in control and qv^{3J} mutant neurons. Nucleus stained by DAPI (blue). Scale bar: 25 μm.

(a) Control: AnkG labeled at its C-terminus.

(b) Mutant: AnkG labeled at its C-terminus.

(c) Control: AnkG labeled at its N-terminus.

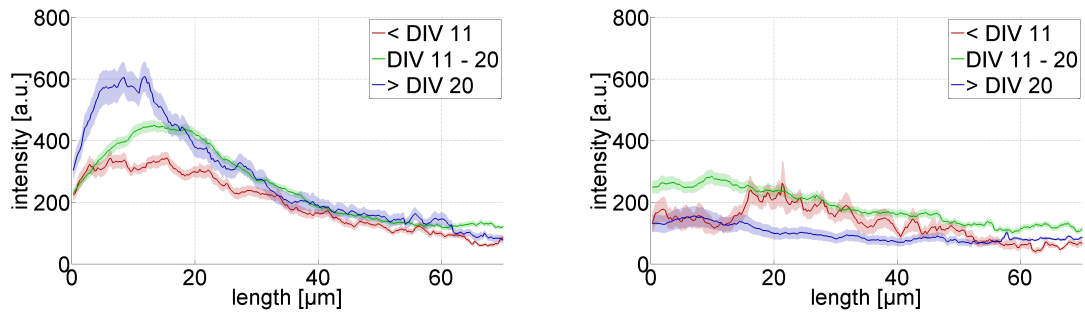**(d)** Mutant: AnkG labeled at its N-terminus.

Figure 45: AnkG in development. Profiles show the mean fluorescence intensity along the AIS as a function of distance from the soma or first branching point at several time points within the first, second and third week in development. (a) Control C-terminal labeled (C-terminal antibody, sc-28561, 11.2). N = 38, 69, 53. (b) Qv^{3J} mutant C-terminal labeled (C-terminal antibody, sc-28561, 11.2). N = 35, 56, 44. (c) Control N-terminal labeled. N = 27, 38, 24. (d) Qv^{3J} mutant N-terminal labeled. N = 23, 19, 11. Error is the SEM.
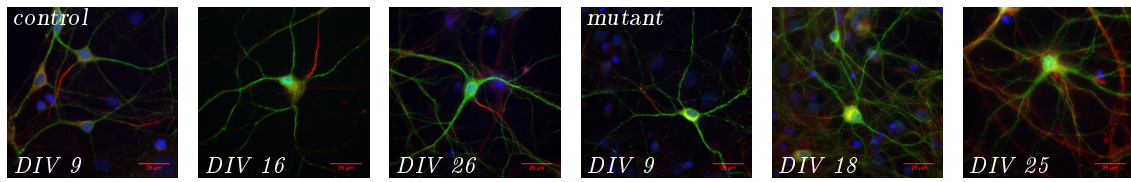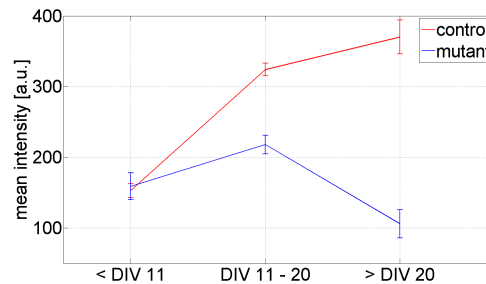
Figure 46: Voltage-gated sodium channels (red) at *DIV 9*, *DIV 16/18* and *DIV 25/26* in control and qv^{3J} mutant neurons. Double labeled with the marker MAP2 (green) at *DIV 9*, *DIV 16/18* and *DIV 25/26* highlights the AIS. Nucleus stained by DAPI (blue). Scale bar: 25 µm.
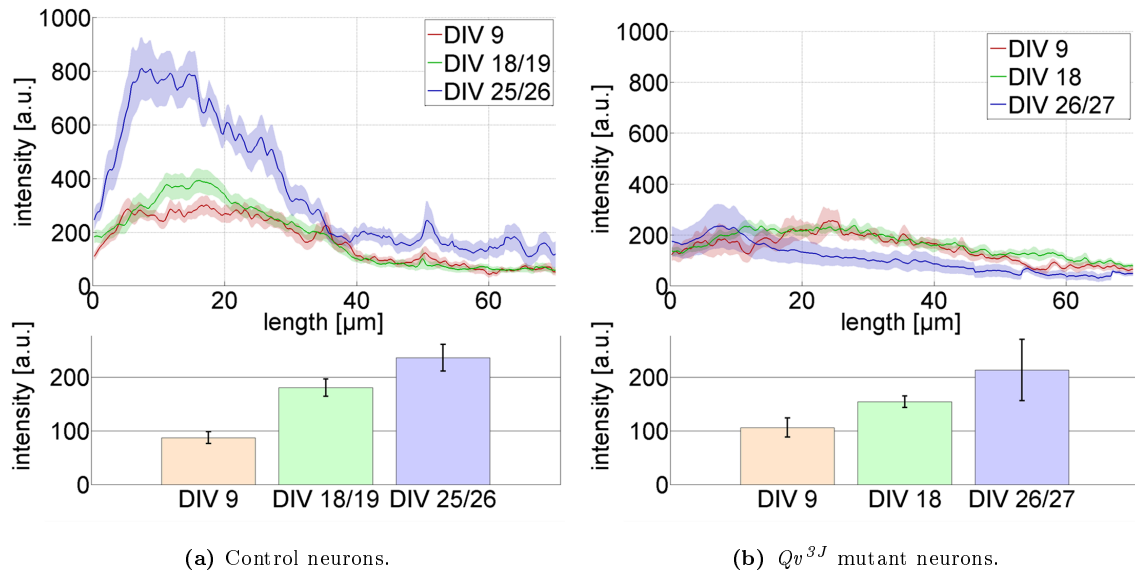

(a) Control: Mean fluorescence intensities [a.u.] along the AIS.

(b) Mutant: Mean fluorescence intensities [a.u.] along the AIS.

(c) Control and mutant: Mean fluorescence intensities [a.u.] at the AIS within the distance 0 - 50.0 µm from the soma or first branching point.

Figure 47: Voltage-gated sodium channels in development. Profiles show the mean fluorescence intensites [a.u.] along the AIS as a function of distance from the soma or first branching point at several time points within the first, second and third week in development: (a) Control. N = 56, 260, 67. (b) VGSC positive qv^{3J} mutants. N = 9, 88, 33. The profiles reveal a differential density and distribution of VGSCs in control and mutant neurons. (c) The graphs show the mean fluorescence intensities [a.u.] at the AIS within the distance 0 - 50.0 µm from the soma or first branching point within the first, second and third week in development for control and qv^{3J} mutant neurons. The graphs reveal that VGSCs are differentially enriched along the AIS in control and mutant neurons. Within the first week the mean fluorescence intensity of anti-panNa$_v$ labeling barely differs. After the first week, the mean fluorescence intensity increases for control and decreases for qv^{3J} mutant neurons. Error is the SEM.

(a) Control neurons.

(b) Qv^{3J} mutant neurons.

Figure 48: Voltage gated sodium channels labeled by anti-panNa$_{\text{v}}$ and analyzed cell-by-cell in the AIS and soma. (a) Control, N = 13, 26, 11 (b) Qv^{3J} mutant, N = 7, 10, 8. Control neurons are *DIV 9, DIV 18/19* and *DIV 25/26* and qv^{3J} mutant neurons are of similar age, *DIV 9, DIV 18* and *DIV 26/27*. (Top) Profiles show the mean fluorescence intensities [a.u.] along the AIS as a function of distance from the soma or first branching point at three time points. (Bottom) The mean fluorescence intensities [a.u.] for defined somatic regions of the neurons are plotted as bars. The factor of the maximum mean intensity along the AIS versus mean intensity at the soma (factor = intensity (mean max. (AIS)/ mean (soma))) is for (a) control neurons 9.16 at *DIV 9*, 4.98 at *DIV 18/19*, and 5.55 at *DIV 25/26* (b) qv^{3J} mutant neurons 3.0 at *DIV 9*, 3.1 at *DIV 18* and 3.2 at *26/27*. Error is the SEM.

6.2 Discussion

Frameshift mutation qv^{3J} eliminates βIV∑1 in early maturation and destabilizes the complete network.

As previously described, and here confirmed by N-terminal and central labeling, the majority of βIV∑1 is integrated in the cytoskeletal network from early on (discussion: 4.2). In some qv^{3J} mutant neurons a low density of βIV-spectrin is found in immature neurons. This is not surprising, since the mutation is located after the epitope targeted by the antibody. The relatively weak staining can be explained by an incomplete formation and destabilization of βIV∑1. Later on, destabilization results in a complete loss of βIV-spectrin. Destabilization of the βIV-spectrin network in mice lacking only βIV∑1 has been described before.[18] Also, a loss of βIV-spectrin in qv^{3J} mutant neurons has been described before.[8] [107] N-terminal and central antibodies target the same isoforms (figure: 56). An AIS labeling within the first week by central labeling is expected. This is not the case, e.g. due to different specificities of the antibodies. The staining observed in the somatic region next to the nucleus (figure: 58) remains in qv^{3J} mutant neurons (discussed: 9.1). The C-terminal antibody targets an epitope located after the frameshift mutation. As expected, no significant AIS labeling was observed from early on, confirming an improperly βIV∑1 formation. Further, C-terminal labeling targets βIV∑6, appearing later in maturation. Since no βIV-spectrin is detected in mature neurons, βIV∑6 might be (i) improper formed, (ii) not stabilized, and (iii) not recruited, due to the lack of βIV∑1. Again, this supports a later appearance of βIV∑6 in the AIS.

Lack of βIV-spectrin results in a reduced ankG density. Recruitment of ankG is impaired. Remaining ankG is stabilized by βII-spectrin.

AnkG density in control and qv^{3J} mutant neurons has a small difference within the first week, but differs significantly in mature neurons. From these findings it can be concluded that ankG is affected by the qv^{3J} mutation. The small difference in immature neurons might be due to remaining βIV-spectrin. Afterward, βIV-spectrin stabilizes and possible recruits ankG in control neurons, whereas qv^{3J} mutant neurons lack the mechanism. Nevertheless, remaining ankG is stabilized in mature qv^{3J} mutant neurons (measurements were performed until *DIV 24*, figure: 73), suggesting that the ankG stabilization depends not only on βIV-spectrin. Previously, βII-spectrin has been found to function as a binding partner for ankG, although it has no role in recruiting ankG and VGSCs.[127] [17] Its binding capability is likely stabilizing ankG in mature qv^{3J} mutant neurons. A rescue mechanism of βIV-spectrin by βII-spectrin, as described previously[78], is excluded (results: 10.1). No increase of βII-spectrin (and ankG) density, while βIV-spectrin density decreases, is observed. This suggests its functionality as an exclusive stabilizing component.

Previously, it has been published that ankG targeting and enrichment in qv^{3J} mutant neurons is non-affected.[1] [64] However, since no maturation studies have been performed and ankG is detected significantly in the AIS of mature neurons, an effect of the mutation on ankG might have been overseen within these studies.

Lack of βIV-spectrin destabilizes VGSCs in the AIS. Constant decrease of VGSCs, but not ankG, suggests a direct association with βIV-spectrin. AnkG is not sufficient for VGSC stabilization.

The obtained data for control neurons match with wildtype results (figure: 47 and 24). Within the first week VGSC density in the AIS of qv^{3J} mutant neurons as a total are not reduced, but lack differential regional enrichment in the AIS. Channels are likely attached by ankG to the remaining βIV-spectrin. With maturation the number of neurons positive for ankG, also positive for VGSCs, constantly decreases (results: 6.1). It is likely that the VGSCs cannot be stabilized throughout qv^{3J} mutant maturation. The constant ankG density (results: 6.1), suggests that VGSC stabilization depends not only on ankG binding, but requires an additional connection to the underlying cytoskeleton. Direct associations between β-spectrins and membrane proteins have been described.[37] [128] [129]

A constant increase of the VGSC density in the somatic region supports the hypothesis that destabilization and recruitment limitations of VGSCs are due to the effects of the qv^{3J} mutation on βIV-spectrin. Furthermore, abnormalities in VGSC expression can be excluded. This allows to conclude that the functionality of βIV-spectrin is important for maintaining high densities of VGSCs in the AIS.

Lack of βIV-spectrin destabilizes $Na_v1.2$ and prohibits $Na_v1.6$ recruitment.

At *DIV 14* 92 % of the AISs positive for ankG are found positive for $Na_v1.2$. Consequently, $Na_v1.2$ is found to be the main subtype in the AIS of qv^{3J} mutant neurons. At *DIV 17* $Na_v1.6$ is largely not detectable and thus likely absent. Since VGSC positive AISs were found to decrease in number, it is concluded that $Na_v1.2$ channels cannot be stabilized in the AIS, due to a lack of βIV-spectrin, and $Na_v1.6$ cannot be recruited in the AIS, due to a lack of the ankG-βIV-spectrin complex. These findings support the double role of βIV-spectrin as a stabilizer and recruiter.

7 Structural organization of axon initial segment components in hippocampal neurons derived from qv^{3J} mutant mice

A structural study is necessary to understand the mechanism, which leads to the impaired information encoding [4] in qv^{3J} mutant neurons.

Two antibodies targeting βIV-spectrin at an epitope located before the frameshift mutation (figure: 56) were evaluated. Only one, the N-terminal βIV-spectrin antibody, showed a weak AIS staining within the first week (results: 6.1, discussion: 6.2). Thus, N-terminal βIV-spectrin labeling was chosen to study the structure of βIV-spectrin in qv^{3J} mutant neurons.

AnkG was found to be expressed at a constant density, independently from the labeling position. Only N-terminal labeling revealed a periodic organization in wildtype neurons (results: 5.1, discussion: 5.2), although N- and C-terminal antibodies target the same splice variants. Consequently, the structure of ankG in qv^{3J} mutant neurons was studied using the N-terminal antibody.

AISs positive for VGSCs were found throughout the entire time of studied maturation (results: 6.1). A structural study between *DIV 11* and *19* was performed.

Since ankG is constant expressed in qv^{3J} mutant neurons, it was found to be most suitable as an AIS marker. It was used for double labeling with anti-βIV-spectrin and anti-panNa$_v$ in order to identify the AIS.

7.1 Results

βIV-spectrin is rare in the AIS of qv^{3J} mutant neurons. Remaining βIV-spectrin lacks periodic organization.

Sibling control and qv^{3J} mutant derived neurons were imaged (figure: 50). Control neurons show a periodicity of about 196 nm, comparable to 190 nm observed in wildtype neurons. As described before (results: 6.1), most qv^{3J} mutant neurons are negative for βIV-spectrin. Below *DIV 10* some AISs are found weakly positive for βIV-spectrin (figure: 50, example at *DIV 7*). Localizations within βIV-spectrin positive qv^{3J} mutant neurons are rare. The extracted example profile displays only three localizations (figure: 50). A noisy power spectrum without an outstanding power at any frequency is obtained.

---

[4] Previous work: Electrophysiology measurements on control (wildtype/heterocygote) and qv^{3J} mutant neurons were performed by Elinor Lazarov, *Hebrew University of Jerusalem, Israel* during her PhD thesis. Manuscript: (2) Elinor Lazarov, Melanie Dannemeyer, Michael Gutnick, Fred Wolf, Andreas Neef "Reduced Nav channel density in the axon initial segment slows down the action potential onset and impairs high frequency encoding."

**AnkG in qv^{3J} mutant neurons is highly regularly organized.**

AnkG labeled N-terminal in control neurons is comparable with previously obtained results (results: 5.1). An even more prominent periodic pattern is observed in the AIS of qv^{3J} mutant neurons. Example profiles of 1.0 μm segments (profiles: 51a) were extracted. At *DIV 11* the profile of a qv^{3J} mutant neuron shows five defined localizations. The control neuron does not show defined localizations. Overlapping localizations cannot be explicit distinguished. At *DIV 13/14* and *19* a similiar behavior is found. Whereas the qv^{3J} mutant neurons display clearly defined localizations, appear the control neurons less structured.

The extracted power spectrum from control neurons at *DIV 11* reveals a small, broad peak at the spatial frequency of about 190 to 200 nm. At higher frequencies the spectrum is noisy. The qv^{3J} mutant does not have a distinct power maximum. At least two maxima between the spatial frequencies of 190 and 200 nm are found. At *DIV 13/14* both power spectra appear less noisy. For qv^{3J} mutant neurons a distinct peak at a frequency of about 192 nm is observed. For control neurons the peak appears less defined and has multiple shoulders. Additionally, especially the spectrum of the control neurons appears noisy at high spatial frequencies. At *DIV 19*, control and qv^{3J} mutant neurons appear with a distinct power maximum at the spatial frequencies of about 190 to 200 nm.

Organization of remaining VGSCs in qv^{3J} mutant neurons is maintained.

Neurons were labeled for ankG C-terminal (C-terminal antibody, sc-28561, 11.2) and VGSCs. Neurons were chosen by being ankG positive. All AISs of control neurons positive for ankG are positive for VGSCs. For qv^{3J} mutant neurons two subgroups of ankG positive neurons are found: (i) positive and (ii) negative for VGSCs.
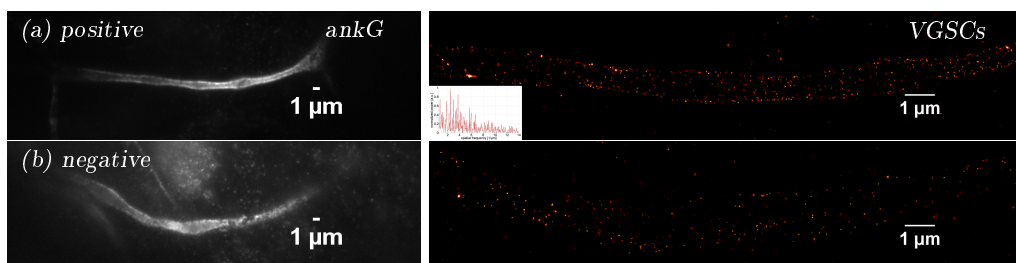

Figure 49: Sodium channels in qv^{3J} mutant neurons. Example images at *DIV 19*. (a) AnkG (wide-field image, grey) positive AIS is VGSC (STORM image) positive. Corresponding power spectrum is shown. (b) AnkG (wide-field image, grey) positive AIS is VGSC (STORM image) negative.

The number of ankG positive AISs of qv^{3J} mutant neurons, positive for VGSCs decreases with

maturation (statistics: 40).

Qv^{3J} mutant neurons, which are highly positive for VGSCs, show a clear dense appearance of localizations in the STORM image and are undistinguishable from control neurons (figure: 49 (a)). Qv^{3J} mutant neurons with AISs negative for VGSCs show no or a very low amount of localizations in the STORM image. The number of localizations is not sufficient for identifying a structure (figure: 49 (b)).

From VGSC positive AISs of qv^{3J} mutant and control neurons the power spectra are calculated. At *DIV 10/11* control and qv^{3J} mutant neurons have a peak at a spatial frequency of about 200 nm. Comparable power values are found at higher frequencies. At *DIV 13/14* the control has a high power peak at about 200 nm. Again similar power values are observed at higher frequencies. The qv^{3J} mutant neurons indicate a small power peak at 200 nm, which is covered by high power values at higher frequencies. At *DIV 19* a distinct power peak at about 200 nm for the control neurons is observed, but the mean spectrum of qv^{3J} mutant neurons appears strongly noisy.
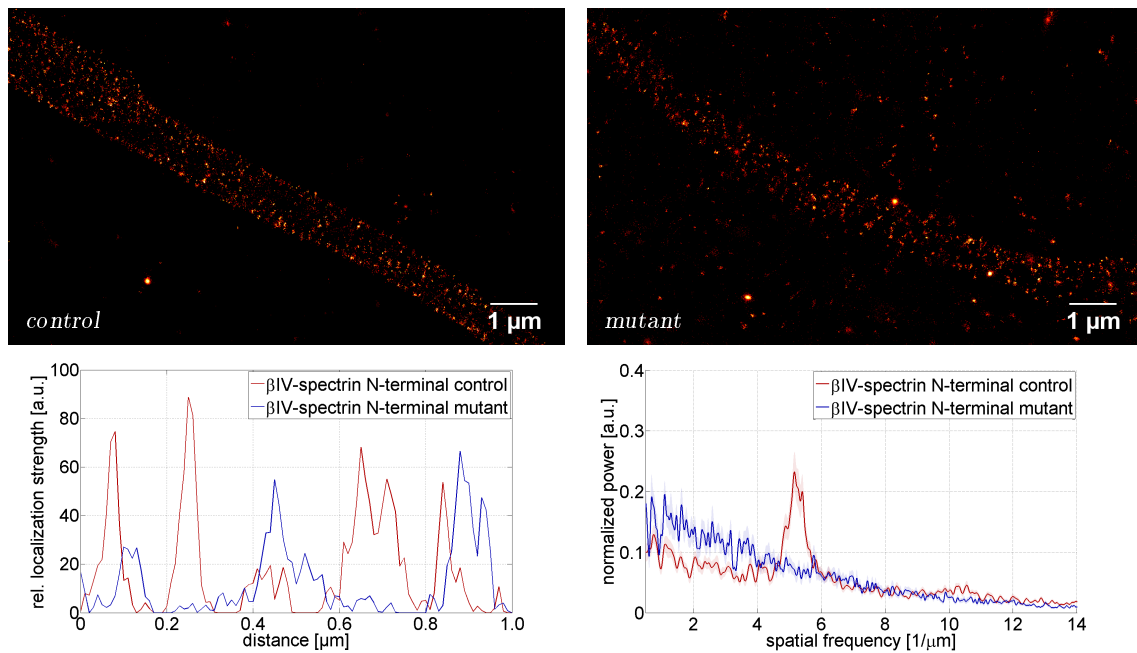
(a) Profiles of 1.0 μm segments extracted from the shown neurons.

(b) Power spectra calculated from the complete βIV-spectrin data set.

Figure 50: Structural comparison of βIV-spectrin in control and qv^{3J} mutant neurons at the age $< DIV\ 11$ by STORM imaging. (a) Profiles of 1.0 μm segments extracted from the shown neurons show regular localizations for control and sparse localizations for qv^{3J} mutant neurons. (b) Power spectra calculated from the complete βIV-spectrin data sets reveal a periodic organization of about 196 nm for control neurons and no defined structure for qv^{3J} mutant neurons. N = 52, 32. Error is the SEM.
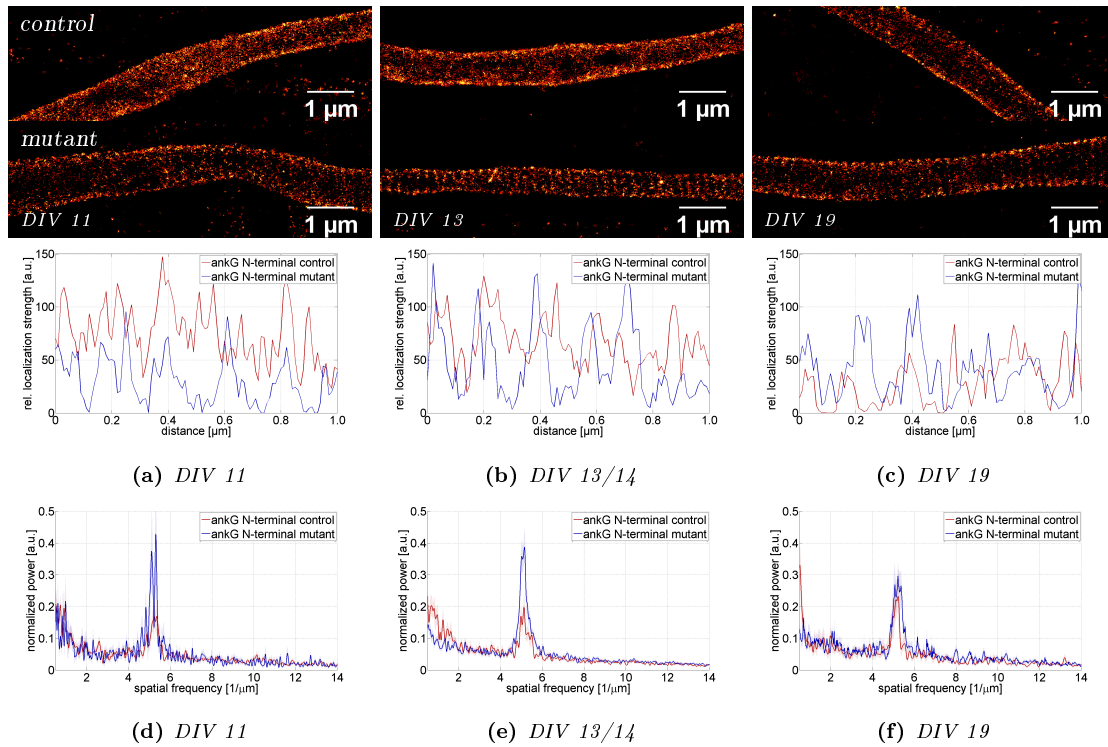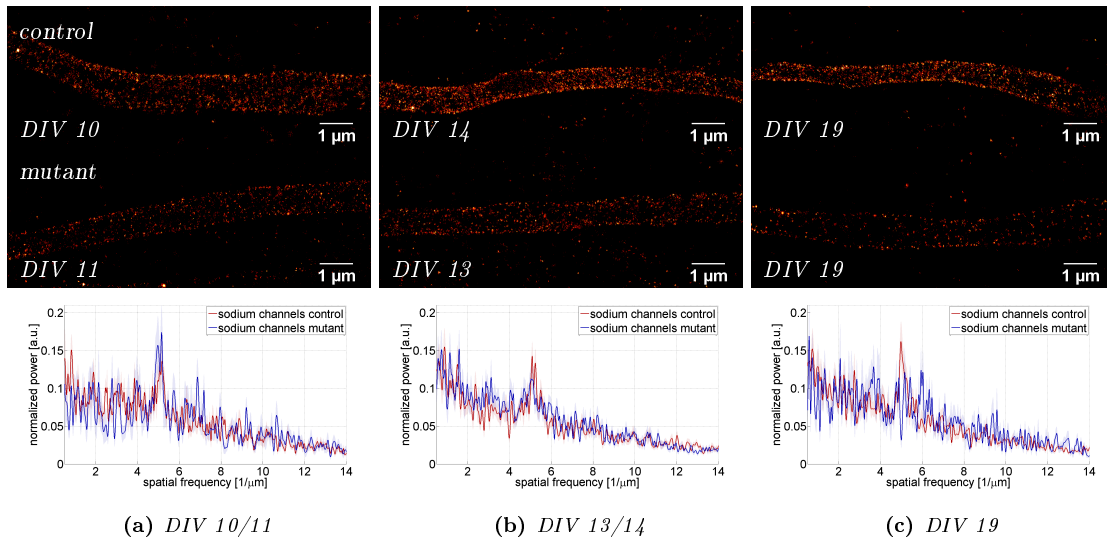
Figure 51: Structural comparison of ankG in control and qv^{3J} mutant neurons at *DIV 10/11, 13/14* and *19* by STORM imaging. (a - c) Profiles of 1.0 µm segments extracted from the shown neurons, show overlapping localizations for control neurons and defined single localizations for qv^{3J} mutant neurons. (d - f) Power spectra calculated from the complete ankG data sets for control and qv^{3J} mutant neurons at *DIV 10/11, 13/14* and *19* reveal a periodic organization of about 190 to 200 nm. N(control) = 17, 28, 14; N(mutant) = 9, 53, 22. Error is the SEM.
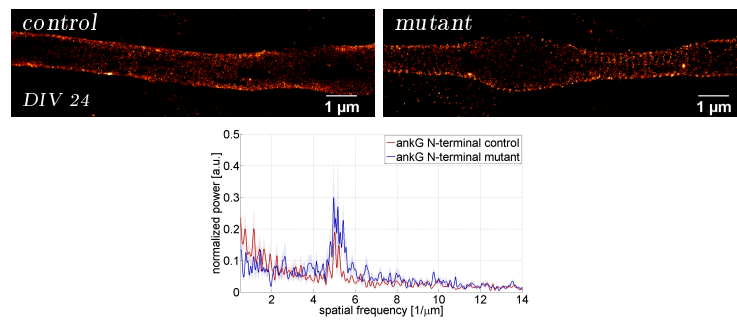
(a) Power spectra calculated from
the complete ankG data sets.

Figure 52: Structural comparison of ankG in control and qv^{3J} mutant neurons by STORM imaging at *DIV 24* in order to investigate, if the effect of the qv^{3J} mutation on ankG proceeds with maturation. (a) Power spectra calculated from the complete ankG data sets for control and qv^{3J} mutant neurons at *DIV 24* reveal a pronounced periodic organization of about 200 nm for qv^{3J} mutant neurons and a less pronounced organization for control neurons. AnkG periodicity is maintained throughout the fourth week in qv^{3J} mutant neurons. N = 12, 10. Error is the SEM.

(a) *DIV 10/11*   (b) *DIV 13/14*   (c) *DIV 19*

Figure 53: Structural comparison of VGSCs in control and qv^{3J} mutant neurons at *DIV 10/11, 13/14* and *19* by STORM imaging. (a - c) Power spectra calculated from the complete VGSC data sets for control and qv^{3J} mutant neurons at *DIV 10/11, 13/14* and *19* reveal a (semi-)periodic organization of about 200 nm. N(control) = 20, 33, 33. N(mutant) = 10, 29, 12. Error is the SEM.

7.2 Discussion

βIV-spectrin lacks its periodic organization from early on, suggesting frameshift qv^{3J} mutation is severe.

βIV-spectrin is highly affected by the frameshift qv^{3J} mutation.[1] [18] A weak staining within the first week, using an N-terminal antibody, is detectable. The structural imaging of the remaining βIV-spectrin, does not reveal an organized network (figure: 50).

The actin-binding domain is located before the frameshift qv^{3J} mutation. Consequently, the binding of βIV-spectrin (specifically βIV∑1) to the underlying periodic actin-adducin ring cytoskeleton could be unaffected. For spectrin tetramer formation an interaction with the β-spectrin repeat 17 takes place.[59] [16] [19] The repeat is located behind the frameshift mutation and likely to be incomplete. Consequently, no complete spectrin tetramers can be formed, resulting in an incomplete periodic organization and insufficient network stabilization.

AnkG is stabilized by βIV- and βII-spectrin: A periodic βIV-spectrin isoform (βIV∑1) within the network mediates periodic ankG placement. A non-periodic βIV-spectrin isoform (βIV∑6) within the network mediates non-periodic ankG placement. βII-spectrin is an additional binding partner for ankG and mediates periodic ankG organization.

In control neurons (figure: 34, 5.2) ankG appears organized, but does not have a striking periodic pattern as observed for βIV-spectrin labeled N-terminal (figure: 32). This was explained by the circumstance that ankG is not a part of the underlying cytoskeletal ring-structured network and periodic organization is only mediated by binding to the structure (details: 5.2). AnkG is affected by the βIV-spectrin frameshift mutation, but is found at a constant density. Surprisingly, remaining ankG is found more prominently periodically organized in the qv^{3J} mutant, than in control neurons. Since βIV-spectrin is gone after the first week in qv^{3J} derived neurons, it is concluded that ankG has another additional binding partner (discussion: 6.2). Here βII-spectrin is suggested. βII-spectrin has been believed earlier to bind, but not recruit, ankG[127] [62] [17] and thus is a candidate as an ankG stabilizer within the network. This is likely, since βII-spectrin is, identically to βIV∑1, periodically organized.[11]

Concluding, in qv^{3J} mutant neurons ankG binds in immature neurons to βIV∑1 and βII-spectrin. In mature qv^{3J} mutant neurons ankG binds only to βII-spectrin. Also, no additional ankG molecules can be recruited. As a consequence, ankG density does not increase. In control neurons, ankG binds to βIV∑1, βII-spectrin and starting within the second week to the non-periodic βIV∑6. Additional ankG molecules can be recruited and the density increases. Thus, a partly non-periodic ankG organization is found in control and a complete periodic organization in

qv^{3J} mutant neurons (figure: 54).

(a) AnkG organization in mature qv^{3J} mutant neurons.

(b) AnkG organization in mature control neurons.
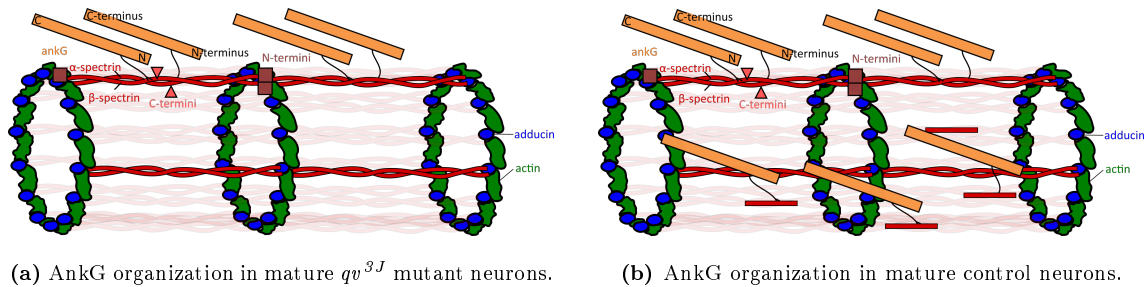
Figure 54: Potential ankG binding partners. (a) In mature qv^{3J} mutant neurons βIV-spectrin is lost. αII/βII-spectrin tetramers remain, are periodically organized and are binding partners for ankG. The model shows ankG bound to αII/βII-spectrin tetramers with the spectrin-binding domain located about one fourth from the N-terminal end of the ankG sequence. (b) In the control neurons αII/βIV-spectrin is found in two splice variants. αII/βIV∑1-spectrin tetramers are periodically organized and besides αII/βII-spectrin tetramers a periodically organized binding partner for ankG. The non-periodically organized βIV∑6, which lacks an actin-binding domain, disrupts the clear organization of ankG molecules in controls.

(Semi-)periodic VGSC organization remains in VGSC positive qv^{3J} mutant neurons. At *DIV 11* the control and qv^{3J} mutant neurons have a comparable VGSC organization with a mainly 200 nm spacing. Additionally, areas with higher frequencies and thus sparser VGSC density are found. Consequently, the VGSCs appear (semi-)periodic (previous findings:[11]). It has to be considered that VGSCs are not fully expressed at *DIV 11*, which explains higher distances between VGSC localizations (results: 24, previous findings:[12]).

In control neurons no changes between *DIV 11* and *13/14* are observed. In qv^{3J} mutant neurons the organization is less pronounced. At *DIV 19* control neurons have an even more prominent (semi-)periodic organization, than at *DIV 13/14*. The qv^{3J} mutant neurons have a low level of organization, due to the low number of remaining VGSCs. The findings support the hypothesis that remaining VGSCs do not lose their organization. Simply, their density decrease leads to a higher distance between the VGSCs. To conclude, the effect of the qv^{3J} mutation on the VGSC stabilization in mature neurons is protruding. Since βIV-spectrin lacks as a mediator between periodically organized actin-adducin rings and VGSCs, another component, likely βII-spectrin, is the linker between the cytoskeleton and VGSCs.

8   Conclusion

AIS maturation and structural constitution is still not fully understood. Previous studies are diverse and models kept simple. Cytoskeletal proteins, actin, adducin and spectrin are believed to constitute to a periodic network. Within this model the proteins actin and adducin form rings, which are connected by spectrins. The adapter protein ankG has multiple binding positions on the spectrin molecules and functions as an adapter for membrane associated and integral proteins. Thus, a (semi-)periodic organization is transferred to membrane proteins, such as VGSCs.[11]

Within this thesis, the basic constitution of the structural AIS model is confirmed.[11] Detailed studies on βIV-spectrin isoforms support that it is important for stabilization and recruitment of AIS proteins. Not all isoforms are build in a periodic matter in the network. βIV∑1 has an actin-binding domain[18] and is found to form spectrin tetramers connecting actin-adducin rings. It is fully expressed early, stabilizes the cytoskeletal network and recruits AIS proteins. Experiments with qv^{3J} mutant neurons showed that a functional C-terminus is crucial for stabilization and recruitment of AIS proteins. βIV∑6 lacks an actin-binding domain[126], its organization does not base on the actin organization, which leads to an irregular appearance. It is expressed largely starting the second week. At this time point it is believed to take over a major role in VGSC recruitment and local enrichment in the AIS. Especially the enrichment of $Na_v1.6$ channels, which density increases tremendously between the second and third week of maturation, is likely linked to βIV∑6 expression.

The incomplete periodic βIV-spectrin organization is transferred on βIV-spectrin binding proteins, such as ankG, and thus on their binding partners, the membrane proteins. Previously, ankG has been described as periodic, but with less prominence, due to multiple close located binding positions on each spectrin tetramer.[12] This might play a role, however its binding to the non-periodically organized βIV∑6, which increases in density with maturation, leads to an increase of the density of non-periodical organized ankG.

Now that it is known that βIV-spectrin isoforms underlie different organization, expression and have different roles, the question arisis if ankG isoforms appear in a similar way. First of all the lack of βIV-spectrin, but the constant ankG density suggests an additional binding partner for ankG. Further, ankG in mice lacking βIV-spectrin appears more pronounced periodic. Together these findings suggest that ankG binds to another periodically organized structure than βIV-spectrin. The constant ankG density suggests that this binding partner stabilizes, but does not recruit ankG. Here it is concluded that βII-spectrin is a stabilizer of ankG. It has been earlier suggested to bind,

but not recruit ankG. [127] [62] [17]

Recently, a new study on ankG binding has been published.[73] A mutation in the spectrin-binding domain (www.uniprot.org, Q12955) of giant 480 kDa ankG showed no effect on βIV-spectrin recruitment and enrichment.[73] This suggests that giant 480 kDa ankG recruits and locally stabilizes βIV-spectrin with another binding motif. Experiments revealed a serine, located at amino acid region 1900. The 1900 amino acid region is missing in the 270 kDa ankG splice form. Their experiments support that this isoform does not recruit βIV-spectrin. Consequently, the spectrin-binding domain (ZU 5) in giant 480 kDa and 270 kDa ankG does not function as a recruitment domain for βIV-spectrin.[73]

In future work it would be interesting to investigate if differential binding mechanisms of ankG isoforms are present in the AIS. Implying, if both ankG isoforms bind to βIV-spectrin and βII-spectrin. This aspect can be investigated by ankG isoform specific labeling in control and βIV-spectrin lacking qv^{3J} mutant neurons. Simple wide-field microscopy allows to determine if both isoforms are present in qv^{3J} mutant neurons. If giant 480 kDa and 270 kDa ankG bind to βII-spectrin, both are expected to be detected in qv^{3J} mutant neurons. The binding of both isoforms to βII-spectrin is likely, since both have a spectrin-binding domain. Giant 480 kDa ankG has been shown not to recruit βIV-spectrin by the spectrin-binding domain, but a serine motif, consequently the spectrin-binding domain is even more likely to function as a binding motif for ankG stabilization by βII-spectrin. 270 kDa ankG has been shown to have no serine motif and failed to recruit βIV-spectrin in the AIS[73], thus it is likely that also 270 kDa ankG binds to βII-spectrin, rather than βIV-spectrin, by the spectrin-binding domain. This leads to the hypothesis that βIV-spectrin is only found to bind giant 480 kDa ankG. Thereby a reduced, but constant density of giant 480 kDa ankG is expected to be found in qv^{3J} mutant neurons. Otherwise a similar density of 270 kDa ankG is expected to be detected in wildtype and qv^{3J} mutant neurons. Further, STORM imaging is suitable to reveal structural differences. If 270 kDa ankG binds only to βII-spectrin it is expected to be prominently periodically organized in the AIS at all ages, including in mature neurons. On the other hand, binding to βIV-spectrin should display a decrease of periodic organization with maturation. In this case giant 480 kDa ankG should display a decrease of periodic organization with an increase of the βIV∑6 density.

The density of βII-spectrin was measured similarly in wildtype and qv^{3J} mutant neurons. This allows to conclude that βII-spectrin plays a role in the cytoskeletal stabilization of the AIS, but does not rescue for βIV-spectrin absence.[78] Additionally, the constant expression of ankG supports that βII-spectrin does not take over the recruitment function of βIV-spectrin. Thus rescue mechanims between β-spectrins cannot be supported by these findings.

(Semi-)periodic organization has been described for VGSCs.[11] The (semi-)periodic, but not pronounced periodic organization was explained by lacking a direct binding to the underlying periodic cytoskeleton, but binding to the irregularly spaced ankG molecules. Again, the non-periodically organized βIVΣ6 needs to be taken into account. A differential organization of subtype $Na_v1.2$ and $Na_v1.6$ has not been questioned. Within this thesis, a comparable organization of sodium channels labeled by anti-panNa$_v$ and subtype $Na_v1.6$ was revealed, whereas $Na_v1.2$ organization could not be definitely revealed, although, $Na_v1.2$ and $Na_v1.6$ share a common ankG binding motif.[68] It needs to be mentioned that subtype specific labeling has been found challenging (results: 9.1.4, 9.1.3). For future work it would be of interest to prove differential VGSC organization by subtype specific knockout mice. This implies that labeling of VGSCs in $Na_v1.6$ and $Na_v1.2$ knockout mice is performed by the same anti-panNa$_v$ antibody. If $Na_v1.2$ and $Na_v1.6$ are organized in the same way, then the structure revealed by anti-panNa$_v$ labeling in $Na_v1.2$ and $Na_v1.6$ knockout mice is expected to be identical. In contrast to subtype specific labeling, the usage of the same antibody ensures that antibody properties, such as different affinities and low labeling success, do not influence the results.

Experiments with βIV-spectrin lacking neurons show a decrease of VGSC density at a constant ankG density. This suggests that ankG is not the only connection between channels and the underlying cytoskeleton. Since direct interactions of spectrins and membrane proteins have been described before, a direct interaction of VGSCs with βIV-spectrin has to be taken into account. Looking specifically at the subtypes $Na_v1.2$ and $Na_v1.6$, $Na_v1.2$ density decreases slowly with maturation, whereas $Na_v1.6$ is not detected from early on. It is suggested that both subtypes bind to both ankG isoforms, but the lack of βIV-spectrin does not allow for stabilization of $Na_v1.2$ and recruitment of $Na_v1.6$ with maturation. This supports the role of βIV-spectrin as a stabilizer and recruiter of VGSCs. Additional experiments with isoform specific ankG knockout mice labeled either for $Na_v1.6$ or $Na_v1.2$, would allow a direct proof, if both channel subtypes bind to both ankG isoforms or a differential mechanism needs to be taken into account.

So far, an extended model is presented in figure 55. For example, explicit results support matural and structural differentiation of βIV-spectrin isoforms. Other suggestions, such as structural differentiation of ankG isoforms still need to be examined more closely. Additionally to the presented results, which allowed the extension of a basic model, the thesis demonstrates how much more questions within the field of AIS functionality, maturation and structural organization are unanswered and have not been considered within any study.
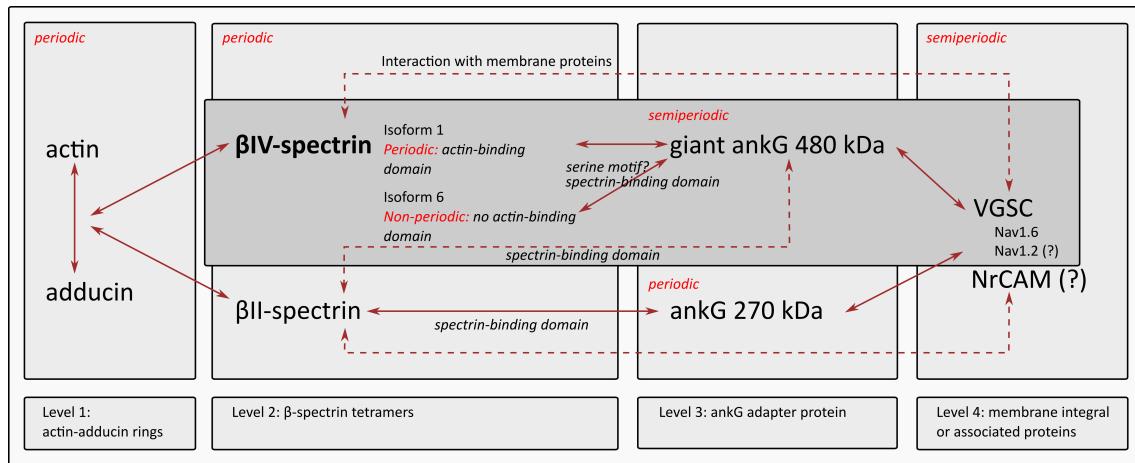
Figure 55: Extended model of AIS proteins and their relationship (dark red arrows) to each other. Four levels of organization (light grey boxes) and their structural organization (red: "periodic", "semiperiodic" and "non-periodic") are highlighted. **Level 1:** Cytoskeletal network composed of actin-adducin rings, forming the underlying periodic network.[11] **Level 2:** β-spectrin tetramers[16][53] connecting actin-adducin rings with each other.[11] βIV-spectrin is highlighted with its main neuronal isoforms, βIV∑1 and 6.[16][18] β-spectrins have been found organized in a periodic matter, except for βIV-spectrin C-terminal labeling. Persuming periodically organized main βIV∑1,[18][11] due to an actin-binding domain, and non-periodically organized βIV∑6, due to a lack of an actin-binding domain.[126] This isoform transfers its non-periodic placement to Level 3 and 4. **Level 3**: Adapter protein ankG[45] found in a periodic and non-periodic matter. This is persumable due to the different βIV-spectrin isoforms and binding positions of ankG on the βIV-spectrin tetramer. Further, differential binding of the two main isoforms giant 480 kDa and 270 kDa ankG to periodic βII-spectrin, βIV∑1 and non-periodic βIV∑6. **Level 4**: Membrane integral and associated proteins with an ankyrin-binding domain. The organization of sodium channels and specifically the subtype $Na_v1.6$ has been found as (semi-)periodic,[11] transferred from an incomplete periodic spectrin network. $Na_v1.2$ and NrCAM have not explicit been revealed as periodically or (semi-)periodically organized (marked by question marks). Additionally, direct interactions of VGSCs and NrCAM with spectrins are marked (VGSCs:[37], NrCAM[130]). **Mutation:** βIV-spectrin, the place of frameshift mutation is highlighted (bold style).[1] Dark grey box highlights the affected protein sequence located in Level 2 - 4, whereas a different influence on different membrane integral and associated proteins is observed. Disruption of the network, due to a βIV-spectrin lack, affects ankG (contrariwise:[1],[64]) and is transferred to some ankG binding proteins, such as VGSCs, but not NrCAM.

9   Appendix A: Experimental procedure

## 9.1   The specificity of immunohistochemistry

One common method to test for antibody specificity is to use multiple antibodies against the same protein, but targeting different epitopes.[124][125] In this work four different antibodies against βIV-spectrin, three against ankG, three against the channel subtype $Na_v1.6$ and two against the channel subtype $Na_v1.2$ were tested.

9.1.1   βIV-spectrin antibodies

Four polyclonal antibodies were used to target different epitopes of βIV-spectrin (list: 11.2).

1. *OriGene*, N-terminal sequence aa2-14

2. *ATLAS*, central located sequence aa1142-1235

3. *Rasband lab, Baylor College of Medicine*, C-terminal sequence aa2237-2253

4. *Santa Cruz*, C-terminal sequence aa2350-2400
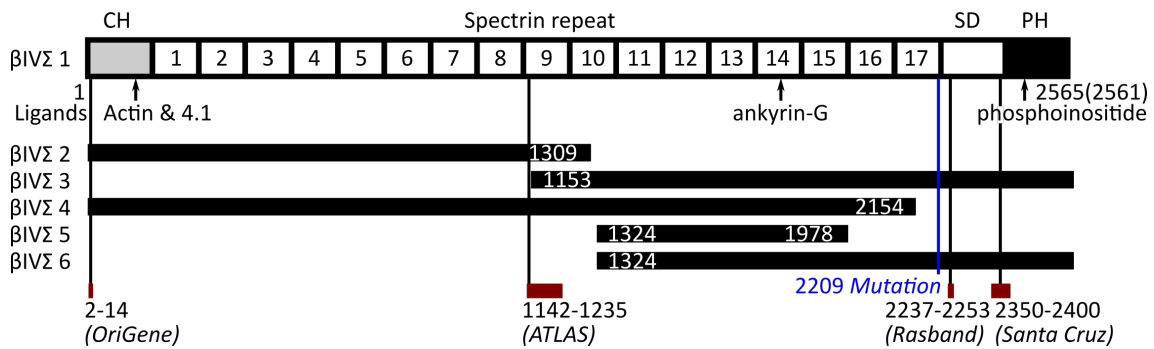
Figure 56: A schematic view of the βIV-spectrin isoforms. βIV∑1 is shown in detail. βIV∑2 - βIV∑6 aligned to βIV∑1. Amino acid sequences of isoforms do not correspond completely. Short insertions, deletions and extensions of βIV∑2 - βIV∑6 relative to βIV∑1 are ignored. White numbers indicate the relative starting and ending amino acid of each isoform in relation to βIV∑1. Ligand binding sites are marked. CH, calponin homology domain; SD, specific domain; PH, pleckstrin homology domain, *modified and extended* [18] *Uniprot.org: Q9H254 , Q8VBX2.* Sequence parts, where antibodies are raised against, are displayed (red) (list: 11.2. Position of qv^{3J} frameshift mutation is marked (blue).

βIV-spectrin antibodies have overlapping AIS labeling. Minor non-specific properties are found.

All double labelings show a significant overlaying staining at the AIS (figure: 57). The central antibody results in a fluorescent dot in the nuclear region of the neuron (figure: 58). Also, in qv^{3J}

mutant neurons, which lack βIV-spectrin, the fluorescent dot remains. This suggests that it is non-specific. The structure looks similar to structures known from cilia, which indicates that the βIV-spectrin antibody targets a homologe sequence. This was not investigated further.

All βIV-spectrin antibodies reveal a weak somatodendritic staining. First of all, it is important to determine the fluorescence intensity of the dendrites staining. This was performed for three out of the four antibodies (N-terminal, central, C-terminal labeled (*antibody gift from Rasband lab, Baylor College of Medicine*)). Control neurons labeled against βIV-spectrin reveal mean fluorescence intensities in the dendrites: N-terminal labeled 47 a.u., central labeled 28 a.u. and C-terminal labeled (*antibody gift from Rasband lab, Baylor College of Medicine*) 17 a.u. (calculated from N = 5, dark background subtracted). Previously, βIV-spectrin has been described as being exclusively found in the AIS. This conclusion is based on immunohistochemistry experiments in slices among others derived from the hippocampal brain region. A strong staining of the AIS, but not dendritic, was observed.[16] It is unknown, if a detailed evaluation of the dendritic labeling has been performed, or if the conclusion is only based on observations. The label specificity, more precise the specificity of the applied antibody against the βIV-spectrin antigen, was proven by using a competitive antigenic peptide. However, no experimental proof has been performed, if βIV-spectrin is restricted to the AIS. Consequently, it cannot be finally excluded that βIV-spectrin is found at a low concentration in the dendrites. Helpful are the experiments performed with the qv^{3J} mutant neurons. Here βIV-spectrin is found to be gone in the AIS of *DIV 14* neurons. The dendritic labeling is found: N-terminal labeled 6 a.u., central labeled 128 a.u. und C-terminal labeled (*antibody gift from Rasband lab, Baylor College of Medicine*) 70 a.u. (calculated of N = 5, dark background subtracted). The comparison of the dendritic labeling in control and mutant neurons reveals small differences. For N-terminal labeling a slight decrease, but for C-terminal and central labeling a slight increase is observed. If one assumes that βIV-spectrin would be part of the dendrites, then a clear reduction or even an absence of βIV-spectrin labeling in mutant dendrites would be expected, due to βIV-spectrin loss in qv^{3J} mutant neurons. This is not the case and allows to suggest a βIV-spectrin absence in dendrites. Moreover, the results suggest that the antibodies have a low level of non-specific binding. Furthermore, autofluorescence of the neurons needs to be considered. To conclude, the comparison of the mean fluorescence intensities in the dendrites and AIS reveals that the intensities in dendrites of 6 to 47(128) a.u. are minor.
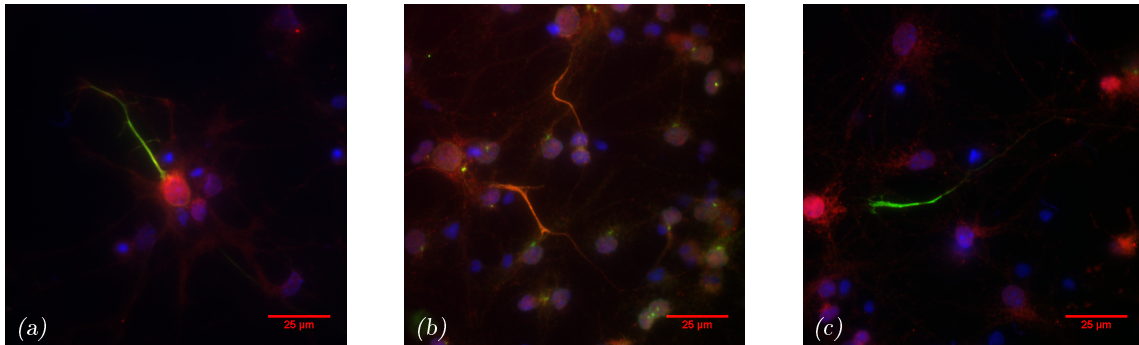
Figure 57: Example images of βIV-spectrin double labeling. (a) N-terminal (red) and C-terminal (antibody gift from *Rasband lab, Baylor College for Medicine*) (green) at *DIV 13*, (b) N-terminal (red) and central (green) at *DIV 20*, (c) C-terminal (C-terminal antibody, sc-131789, 11.2) (red) and C-terminal (antibody gift from *Rasband lab, Baylor College for Medicine*) (green) at *DIV 13*. Nucleus stained by DAPI (blue). Scale bar: 25.0 μm.
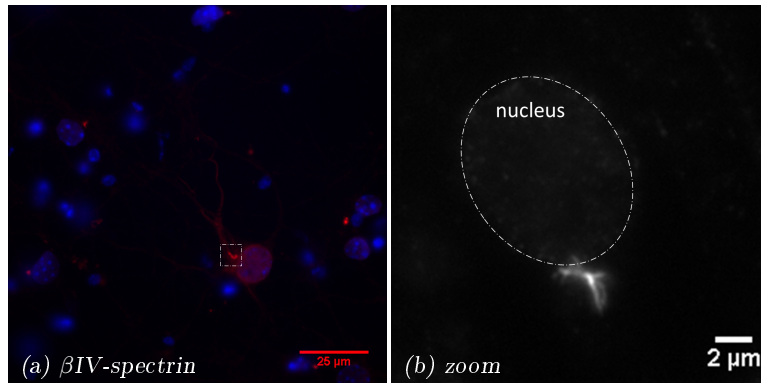

Figure 58: Example image of a hippocampal neuron at *DIV 20*. (a) Wide-field image of βIV-spectrin labeled central (red) and nucleus stained by DAPI (blue). Area of uncertain fluorescence is boxed. (b) Zoom in a neuron. Nucleus is marked by dashed lines. Area of uncertain fluorescence close to the nucleus (somatic located). Scale bar: 25.0 μm.

βIV-spectrin antibodies target different splice variants.

The four antibodies target different splice variants of βIV-spectrin. This was examined more closely by performing double labeling and extracting the profiles (method: 3.5.1).

(a) *DIV 8* (b) *DIV 13* (c) Profiles divided
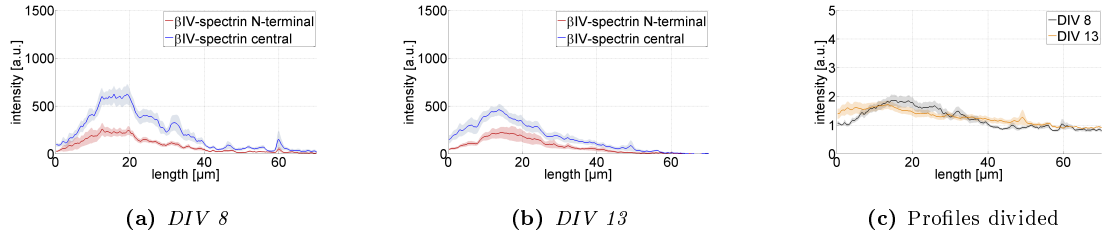
Figure 59: Double labeling of βIV-spectrin at an N-terminal and a more central located sequence part. (a) *DIV 8*, N = 12. (b) *DIV 13*, N = 9. (c) Profiles divided: βIV-spectrin central by N-terminal. Error is the SEM.

(a) *DIV 8* (b) *DIV 13* (c) Profiles divided
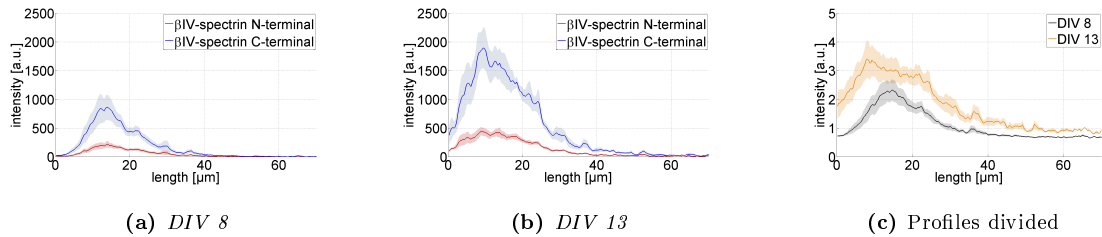
Figure 60: Double labeling of βIV-spectrin at a N-terminal and C-terminal (antibody gift from *Rasband lab, Baylor College for Medicine*) located sequence part. (a) *DIV 8*, N = 15. (b) *DIV 13*, N = 11. (c) Profiles divided: βIV-spectrin C-terminal by N-terminal. Error is the SEM.

In the two weeks the profiles (figure: 59, 60) look as expected. Profiles along the AIS with areas of high mean fluorescence intensities are found, which suggests an enrichment of βIV-spectrin. With maturation the βIV-spectrin density increases. Double labeling allows to determine if the antibodies target the same structures. Profiles were divided neuron by neuron. Afterward, the mean profile and the standard error of the mean (SEM) was calculated (method: 3.5.1). After division of profiles, central labeled by N-terminal labeled, the mean profile appears smooth (figure: 59). Concluding, the antibodies target the same splice variant (βIV$\sum$1). After division of the profiles from double labeling N- and C-terminal an uneven profile remains. To conclude, the antibodies target different structures. Both target the βIV$\sum$1, but only the antibody directed against a C-terminal located sequence targets the βIV$\sum$6.

9.1.2 Ankyrin-G antibodies

The adapter protein ankG is known to be highly enriched in the AIS. Three different antibodies against ankG were evaluated (all from *Santa Cruz Biotechnology*, list: 11.2).

1. Monoclonal, spectrin-binding domain, synthetic peptide aa982-1107

2. Polyclonal, C-terminal, aa4150-4200

3. Polyclonal, C-terminal, aa4163-4377

AnkG antibodies show overlapping AIS labeling.
The N- and C-terminal antibodies result in a bright AIS and additional somatic staining (figure: 61). AnkG has been found to be a major part of the AIS, but not excluded from the soma (e.g. [82] [83]). The C-terminal antibodies display higher somatic fluorescence intensities than the N-terminal antibody. This is not surprising, since the N-terminal antibody is a high specific monoclonal antibody, whereas the C-terminal antibodies are polyclonal.

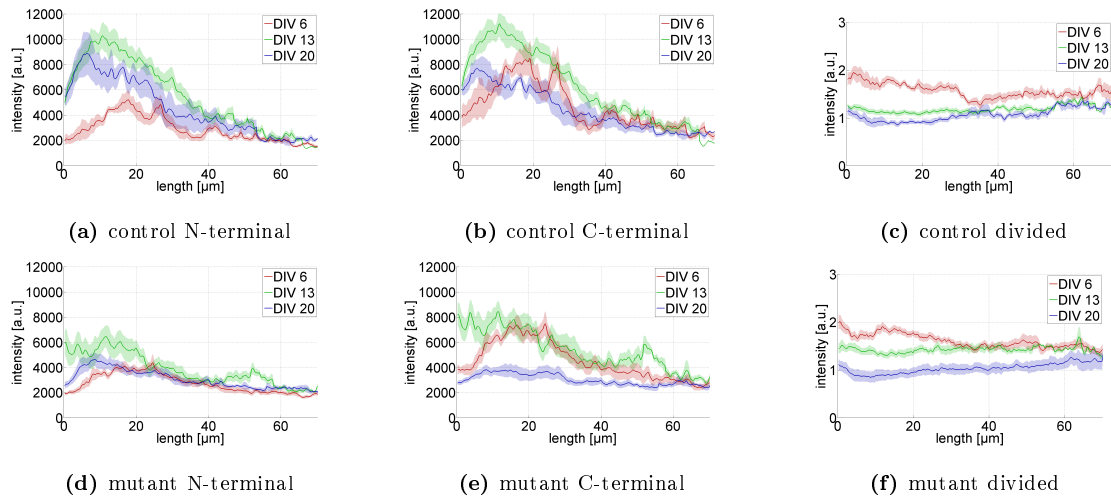(a) N-terminal   (b) C-terminal   (c) N- and C-terminal
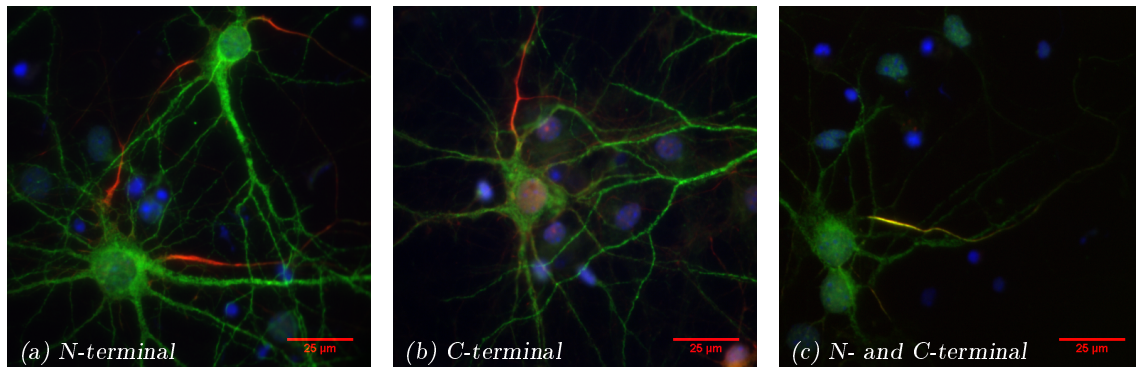
Figure 61: Comparison of two ankG (red) antibodies targeting either a more N- or C-terminal (C-terminal antibody, sc-28561, 11.2) located region. Nucleus stained by DAPI (blue). (a) and (b) double labeling with MAP2 (green) to identify the AIS. (c) Overlapping fluorescence at the AIS: C-terminal (green) and N-terminal (red).

AnkG antibodies target the same splice variants.
Database research (www.uniprot.org, Q12955, W6PPA1) (data not shown) reveals that the neuronal ankG isoforms (270 kDa, 480 kDa) differ significantly in sequence length, but share a common N- and C-terminal region. The alignment (tool: EMBL-EBI EMBOSS) shows that the three antibody epitopes are found in both ankG isoforms.
Double labeling was performed for control and qv^{3J} mutant neurons (figure: 62) . The qv^{3J} mutant neurons have a significant lower ankG density (results: 6.1). The profiles divided cell-by-cell appear smooth. Consequently, confirmed by control and qv^{3J} mutant neurons, the antibodies target all splice variants.

(a) control N-terminal

(b) control C-terminal

(c) control divided

(d) mutant N-terminal

(e) mutant C-terminal

(f) mutant divided

Figure 62: Double labeling of ankG at a N-terminal and C-terminal (C-terminal antibody, sc-28561, 11.2) located sequence part over three weeks of maturation at *DIV 6*, *DIV 13*, and *DIV 20*. (a) Control labeled N-terminal: AnkG is enriched in the AIS. (b) Control labeled C-terminal: AnkG is enriched in the AIS. (c) Control divided profiles, C-terminal by N-terminal: Profiles appear smooth. Antibodies target the same structures. (d) Mutant labeled N-terminal: A weak, but constant ankG density is found. (e) Mutant labeled C-terminal: A weak, but constant ankG density is found. (f) Mutant divided profiles, C-terminal by N-terminal: Profiles appear smooth. Antibodies target the same structures. N(control) = 8, 13, 6. N(mutant) = 12, 9, 5. Error is the SEM.

9.1.3   Subtype Na$_v$1.6 antibodies

VGSC subtype labeling is known to be a challenging field. Here three different antibodies against the sodium channel subtype Na$_v$1.6 were evaluated (list: 11.2).

1. Polyclonal, from *Alomone*, epitope corresponding to the aa1042-1061 of Na$_v$1.6 in rats. This sequence is located in the intracellular loop between the domains II and III.

2. Monoclonal, from *Neuromab*, raised against a synthetic peptide corresponding to the aa459-476 of Na$_v$1.6 in rats. This sequence is located in the intracellular loop between the domains II and III.

3. Gift from the *Rasband lab, Baylor College of Medicine.*

The antibodies were tested under different conditions, including a wide range of concentrations, two different immunohistochemistry protocols and antigen retrieval methods, SDS and pepsin treatment. Changes in immunohistochemistry protocols and antigen retrieval did not improve the staining quality or led to different results (data not shown).
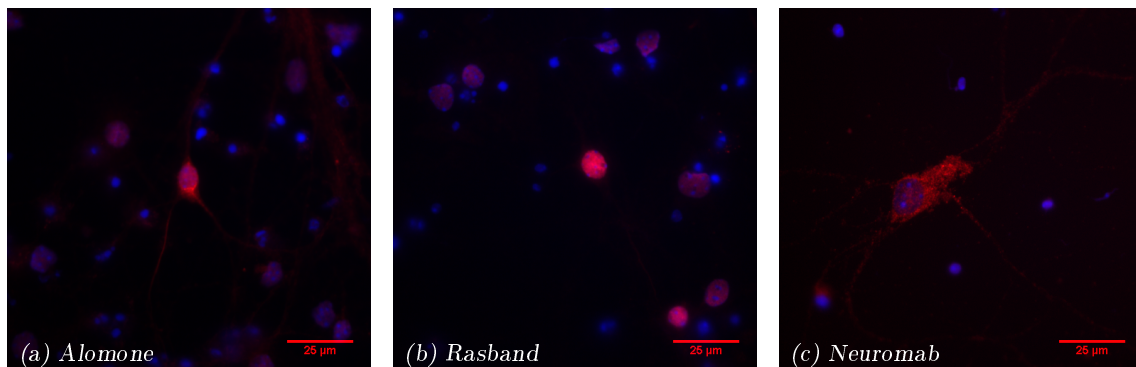
Figure 63: Comparison of three different anti-Na$_v$1.6 (red) antibodies at *DIV 20*. Nucleus stained by DAPI (blue). (a) Polyclonal Na$_v$1.6 antibody from *Alomone* (b) Na$_v$1.6 antibody from *Rasband lab* (c) Monoclonal Na$_v$1.6 antibody from *Neuromab*.

Diversity of staining pattern suggests non-specific binding of the antibodies.
Major differences between the antibodies were observed.
In most cases the *Alomone* antibody shows a significant AIS staining (identified by double labeling with anti-MAP2, anti-panNa$_v$ or anti-ankG). A weaker staining is observed for somatodendritic compartments. Na$_v$1.6 channels have been described in the AIS and somatic compartment before.[26][27] However, a bright nucleus staining, as obtained by this antibody, seems inappropriate. Moreover, this staining has been found to remain in Na$_v$1.6 knockout mice (*conversations with Anja Scheller, University of Saarland*). This suggests that it is non-specific. Additionally, when

analyzing the fluorescence intensity in the somatic region an overestimation needs to be considered, since the bright nucleus staining might influence the somatic mean fluorescence intensity.

The antibody, which was obtained as a gift from the *Rasband lab, Baylor College on Medicine* displays a bright nucleus staining and a weak staining of neuronal branches. No images with a significant AIS staining were obtained. The bright nucleus and very weak neurite staining indicate that it is non-specific. Especially, the bright nucleus suggests a similar non-specific binding, as described for the *Alomone* antibody.

The monoclonal antibody from *Neuromab* shows a very diverse staining. In some cases the staining failed completely and in other cases an evenly staining of the neurons was observed. [131] In these cases a significant somatic staining was obtained. This seems appropriate, since $Na_v1.6$ channels have been described in somatic compartments before. [26] [27] Dendrites and AIS could not be distinguished. This cannot be supported with previous findings, because $Na_v1.6$ channels have been described as being enriched in the AIS. [29] [31] However, the obtained staining pattern agrees with an earlier publication. [131]

The epitopes of the *Alomone* and *Neuromab* antibodies are located in the same intracellular loop between the domains II - III. Similar staining pattern of these antibodies are expected.

Due to the fact that the *Alomone* antibody has been best described and its non-specific binding properties have been evaluated in detail, it appears most suitable to be used for the experiments in this thesis.

9.1.4   Subtype Na$_v$1.2 antibodies

The VGSC subtype Na$_v$1.2 was targeted with two antibodies.

1. Polyclonal, from *Alomone*, raised against the region aa467-485 of Na$_v$1.2 in rats.

2. Monoclonal, from *Neuromab*, raised against aa1882-2005 of Na$_v$1.2 in rats. The sequence is located at the cytoplasmic C-terminus.

The polyclonal antibody from *Alomone* shows a bright staining at or close to the nucleus. A weak staining is observed for the neuronal branches. Dendrites and axon cannot be distinguished. The monoclonal *Neuromab* antibody shows a brighter and in most cases significant AIS staining. This seems appropriate, since Na$_v$1.2 channels have been described as being enriched in the AIS. [29] [31] One explanation for the difference is that the polyclonal has a lower specificity than the monoclonal antibody. Moreover, masking of one or the other epitope in the AIS cannot be excluded. Identification of the AIS was performed by double labeling with anti-MAP2 or anti-ankG. The monoclonal anti-Na$_v$1.2 antibody from *Neuromab* was chosen for the project.

(a) Alomone   (b) Neuromab   (c) Neuromab, MAP2
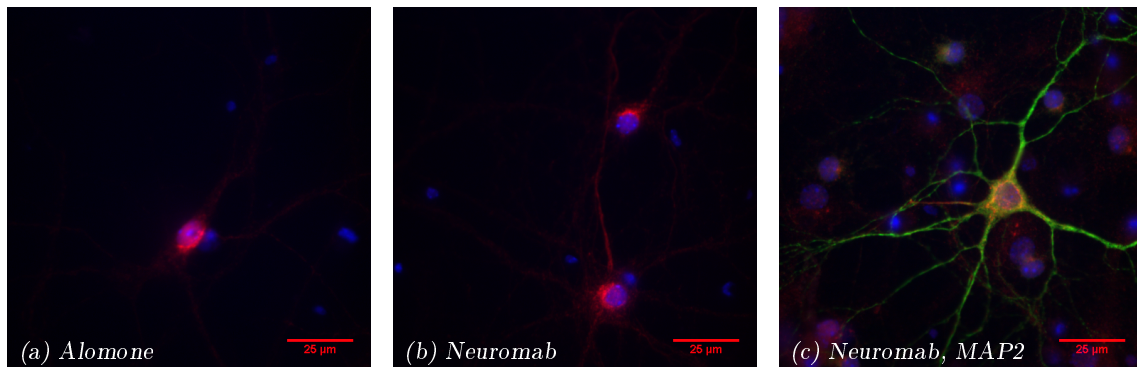
Figure 64: Comparison of two different anti-Na$_v$1.2 (red) antibodies at *DIV 13*. (a) Polyclonal Na$_v$1.2 (red) antibody from *Alomone* (b) Monoclonal Na$_v$1.2 (red) antibody from *Neuromab*. (c) Double labeling of Na$_v$1.2 (red) antibody from *Neuromab* with anti-MAP2 (green) for AIS identification.

10 Appendix B: Results

The following appendix section displays additional results, which are not shown in the main part of the thesis, but support the discussion section and drawn conclusions.

10.1 βII-spectrin

βII-spectrin does not rescue for βIV-spectrin deficiency.

βII-spectrin belongs to the spectrin family.[127] [132] Rescue mechanisms between spectrins have been described before.[78] Thus, the question arises if the loss of βIV-spectrin in the qv^{3J} mutation has an effect on βII-spectrin density.

The AIS was identified by double labeling with ankG (C-terminal antibody, sc-28561, 11.2). The images (figure: 65) do not show a reduced staining of βII-spectrin in qv^{3J} mutant neurons. The average intensity of the AISs was determined. Control and qv^{3J} mutant neurons have a high βII-spectrin density in the first week. While βIV-spectrin increases only in control neurons, βII-spectrin decreases[11] and behaves similar in control and qv^{3J} mutant neurons. Consequently, βII-spectrin does not function within a rescue role for βIV-spectrin.
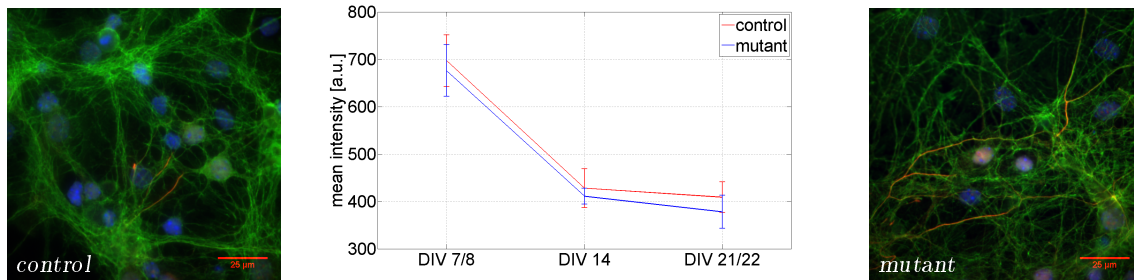
Figure 65: βII-spectrin in control and qv^{3J} mutant neurons. Double labeling of βII-spectrin (green) and ankG (red) (C-terminal antibody, sc-28561, 11.2) at *DIV 8*. Nucleus stained by DAPI (blue). Scale bar: 25.0 µm. Graph: βII-spectrin expression in control and qv^{3J} mutant neurons at three maturation stages. The graphic shows the mean fluorescence intensities [a.u.] at the AIS within the distance 0 - 50.0 µm from the soma or first branching point. N(control) = 36, 22, 27. N(mutant) = 32, 11, 22. The error is the SEM.

**Periodic organization of βII-spectrin is not restricted to the AIS.**

βII-spectrin is not exclusively expressed in the AIS, but a major component of somatodendritic compartments. [127] [132] The AISs of mature neurons have a clear periodic organization of βII-spectrin (figure: 66). The spatial frequency is about 190 nm and agrees with previous findings. [11] Here, a detailed analysis revealed periodic organized branches, negative for βIV-spectrin and ankG, which indicates that these are not AISs. Extracted power spectra confirm the periodic organization. Previously periodicity has been described as being confined to the AIS [11], later this has been rejected and periodicity has been described in dendrites. [12] Here a clear periodic βII-spectrin organization in dendrites is found.
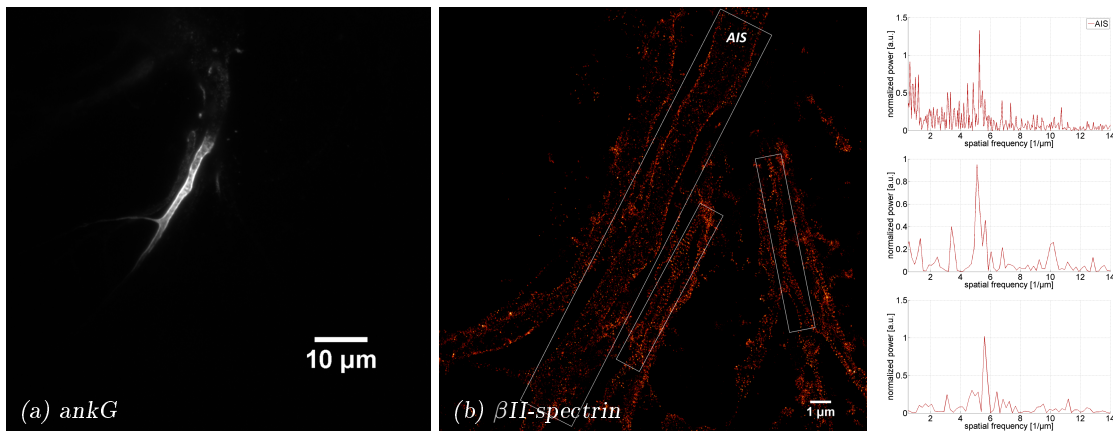
Figure 66: Structure of βII-spectrin in neurites of control neurons. (a) AnkG (C-terminal antibody, sc-28561, 11.2) identifies the AIS. (b) Complete STORM image of a hippocampal neuron at *DIV 13* stained for βII-spectrin. The AIS and two potential dendrites are marked. The corresponding power spectra reveal frequencies in the range of 165 - 192 nm. (AIS: top, Dendrites: bottom)

Qv^{3J} mutation does not disrupt the βII-spectrin structure.

Imaging was performed on *DIV 13* neurons. Control and mutant neurons have periodically structured AISs (figure: 67) and similar power spectra. In both spectra, broad peaks within the range of 180 to 205 nm are observed (figure: 67). There is no influence of the qv^{3J} mutation on the βII-spectrin structure.
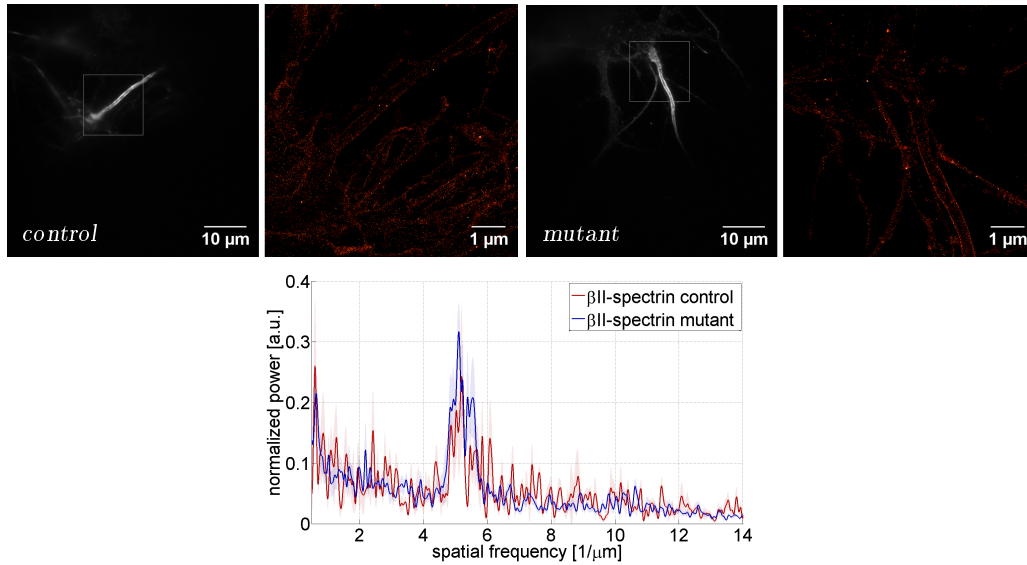
(a) Calculated power spectra from the complete βII-spectrin data sets.

Figure 67: Structural comparison of βII-spectrin in control and qv^{3J} mutant neurons at *DIV 13*. AnkG channel (C-terminal antibody, sc-28561, 11.2) shown in grey. Boxed region of interest was imaged for βII-spectrin in control and qv^{3J} mutant neurons. (a) Power spectra calculated from the complete data sets. N = 25, 14. Error is the SEM.

10.2   The structure of ankG targeted C-terminal in immature neurons

Previously, βIV-spectrin was described as appearing periodic in immature, but not in mature neurons, when labeled at a C-terminal located epitope (results: 34). Analog, ankG is investigated by C-terminal labeling in immature neurons.

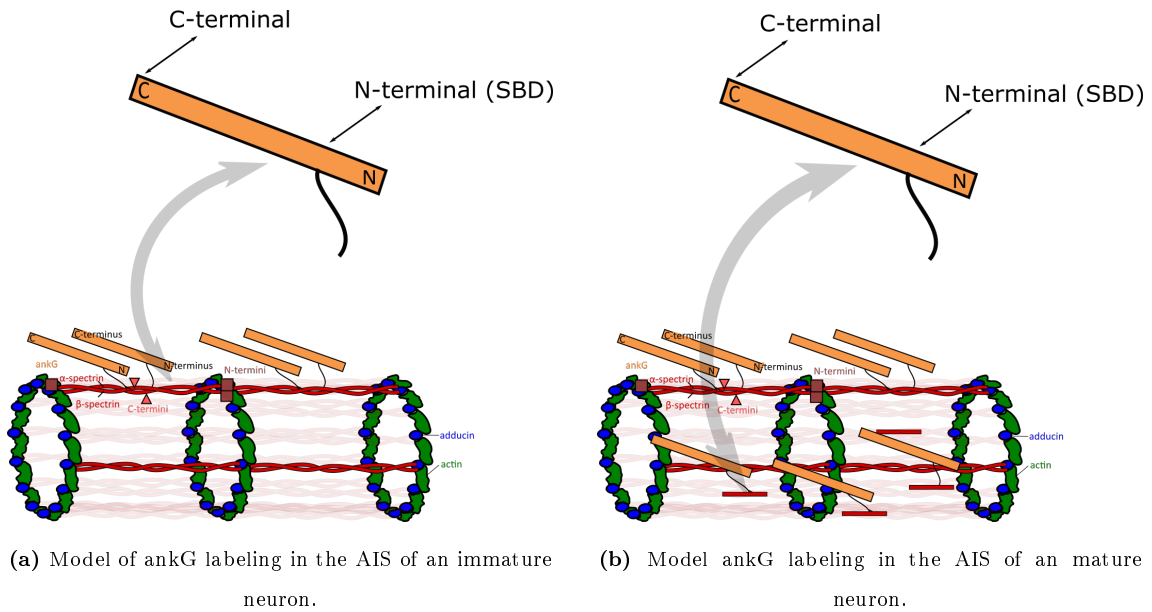**Low level of periodically organized ankG in immature control and qv^{3J} mutant neurons.**

The extracted power spectra are noisy (figure: 69). High power values are prominent at high frequencies. Between the frequencies 172 and 238 nm display control and qv^{3J} mutant neurons a peak in the power spectrum, which indicates that some AISs or regions have a periodic organization. The pattern is more prominent in qv^{3J} mutant than in control neurons (as observed for βIV-spectrin labeled N-terminal (results: 51, discussion: 7.2)). Contrariwise, in mature wildtypes no periodic organization of ankG, labeled C-terminal, was observed (results: 69).

The obtained data set is classified in three groups:

1. Subgroup 1: Prominent 200 nm organization (Control neurons 4.5 %, mutant neurons 37.0 %).

2. Subgroup 2: Partly 200 nm organization. Partly the spacing between localizations is above 200 nm (Control neurons 13.6 %, mutant neurons 18.5 %).

3. Subgroup 3: Noise only (Control neurons 81.8 %, mutant neurons 44.4 %).

Here arisis the question, why ankG labeled at its C-terminus displays a partly periodic organization, especially in qv^{3J} mutant neurons. AnkG has been described to have two possible binding domains for spectrin. The common spectrin-binding domain, located about one fourth from the N-terminus and the more central located serine[73] (details: 2.3). In both cases ankG has multiple options for its orientation. At *DIV 8* to *10* the density of irregular βIV$\sum$6 is very low and allows for a more regular organized ankG based on βIV$\sum$1. Further, wide-field data (results: 22 6.1) show that ankG is not necessarily fully expressed within the first week. At the age of *DIV 8* to *10* a relative small number of molecules is placed into the network. The sparse molecule placement might allow, despite the tremendous size of giant 480 kDa ankG[73], to resolve partly periodic areas. An even more sparse placement of ankG molecules in qv^{3J} mutant neurons, due to the low density of βIV$\sum$1, might enhance the periodic pattern. Further, it is assumed that the lower ankG density in qv^{3J} mutant neurons has a relative higher density of 270 kDa ankG to giant 480 kDa ankG (discussed in: 8). Since, 270 kDa ankG is much smaller than giant 480 kDa ankG the

C-terminal labeling position is located closer to the underlying spectrin network.

(a) Model of ankG labeling in the AIS of an immature neuron.

(b) Model ankG labeling in the AIS of an mature neuron.

Figure 68: Model of ankG organization in the AIS. Labeling positions of the N- and C-terminal antibodies are illustrated on the giant 480 kDa ankG molecule. Whereas N-terminal labeling targets the spectrin-binding domain, targets C-terminal labeling the furthest possible position from the spectrin molecules. (a) Immature neurons consist of αII/βII- and αII/βIV∑1-spectrin tetramers, which form a highly organized AIS. In immature qv^{3J} mutant neurons αII/βIV∑1-spectrin tetramers are highly reduced or even absent and the structure is maintained only by αII/βII-spectrin tetramers. A low pronounced, but significant periodic organization of ankG transferred from the underlying network, can be revealed by far distance C-terminal labeling. (b) Mature neurons consist of αII/βII- and αII/βIV∑1-spectrin tetramers and an additional βIV-spectrin splice variant, βIV∑6. This increases not only the density of spectrin molecules in mature neurons, but also integrates in a non-periodic matter. The organization of ankG appears largely unorganized.
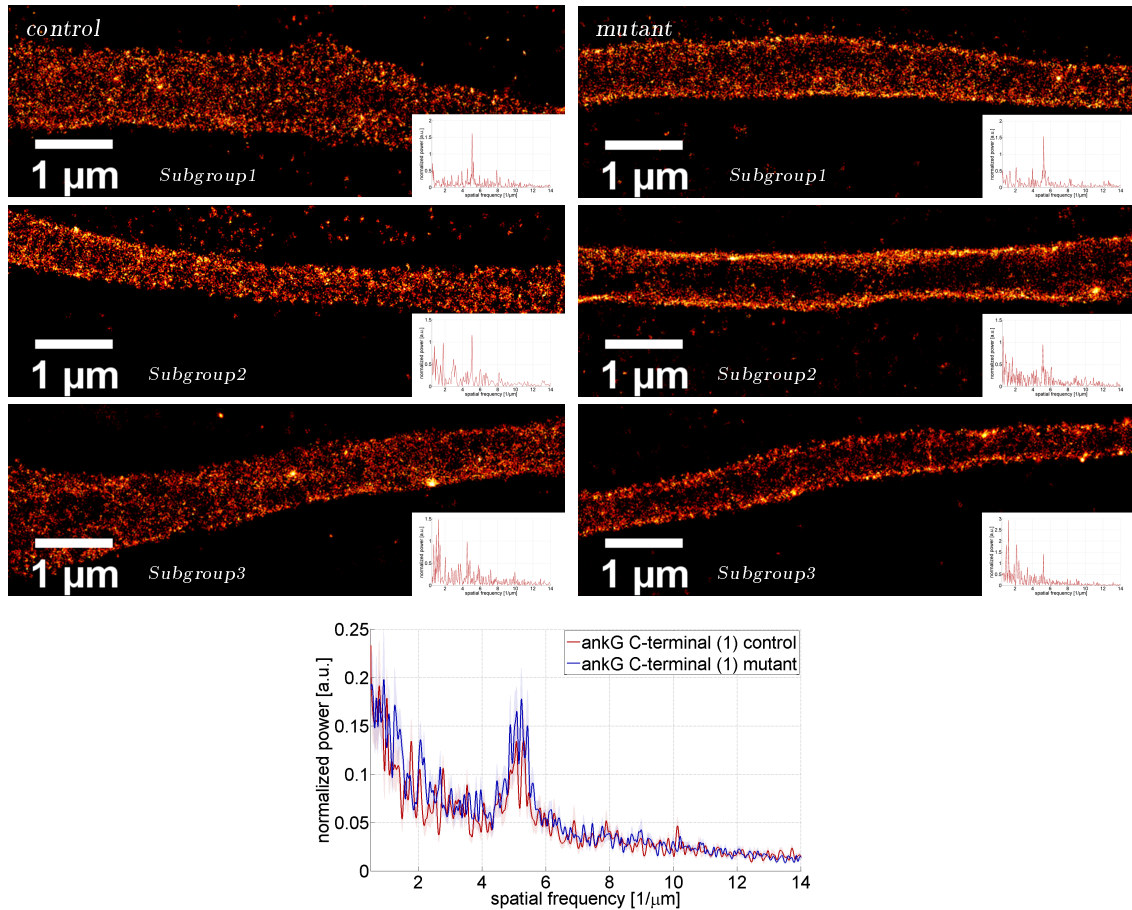
(a) Calculated power spectra from the complete data set.

Figure 69: Structural comparison of ankG (C-terminal antibody, sc-28561, 11.2) in control and qv^{3J} mutant neurons at *DIV 8 - 10* by STORM imaging. Example images from three subgroups of the data set and their corresponding power spectra. Subgroup1: Prominent 200 nm periodic pattern. Subgroup2: Partly areas of 200 nm periodic organization. Subgroup3: Noise only. (a) Power spectra calculated from the complete data sets for control and qv^{3J} mutant neurons. Low level of 200 nm periodic organization, more prominent in qv^{3J} mutant neurons. N = 22, 27. Error is the SEM.

10.3   Details of voltage-gated sodium channel subtype $Na_v1.2$

The obtained data set (*DIV 14*) revealed no clear periodic pattern for $Na_v1.2$ channels (results: 5.1). The mean power spectrum shows several peaks at high frequencies. This includes a frequency of about 200 nm, which was identified as the periodic pattern for VGSC organization by anti-panNa$_v$[11] and anti-Nav1.6 (figure: 35) labeling. $Na_v1.2$ and $Na_v1.6$ share a common ankG binding motif, which leads to the expectation that their organization in the AIS does not differ.

The distribution of the data set is studied in more detail. The power spectra were extracted for each neuron and classified into two groups (figure: 70):

1. Spectra, which have a high power at the spatial frequency of about 200 nm and at additional higher frequencies.

2. Spectra, which appear noisy and have no peak at about 200 nm.

The groups are equally sized. None of the spectra has a defined frequency of about 200 nm. Thus, averaging of the power spectra is not the reason why no clear pattern of $Na_v1.2$ organization is found (discussed in: 5.2).

(a) AnkG C-terminal.   (b) $Na_v1.2$ STORM.   (c) Power spectra.
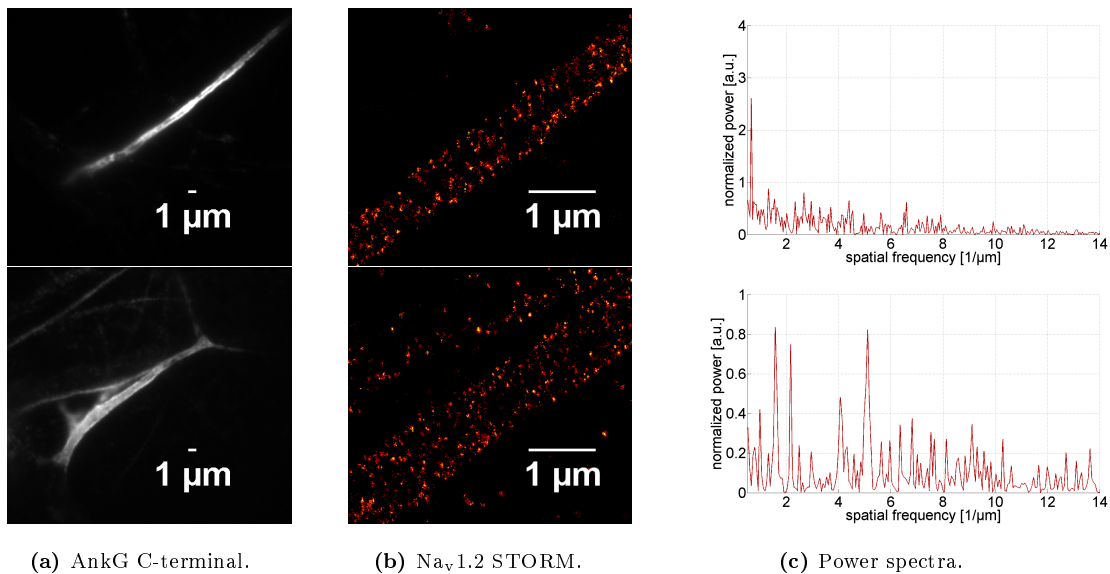
Figure 70: Details of $Na_v1.2$ structural organization by STORM imaging. Example images represent the two identified groups within the data set. (a) AIS identification by ankG (C-terminal antibody, sc-28561, 11.2) wide-field image. (b) Zoom in $Na_v1.2$ STORM image. (c) Corresponding power spectra for the full length of the AIS.

10.4   NrCAM

The neuronal cell adhesion molecule (NrCAM) is a major component expressed in the AIS. It is involved in neuron-neuron adhesion and has, like many other proteins, an ankyrin-binding site. AnkG was described as being affected by the frameshift mutation qv^{3J} (results: 6.1). Consequently, NrCAM could also be affected.

NrCAM displayed a dense network in both cultures (figure: 71). Double labeling with ankG (labeled at its N-terminus, list 11.2) allowed the AIS identification.

**The qv^{3J} mutation does not affect the NrCAM density.**

The mean intensities were determined for three maturation stages (figure: 71). In immature neurons control neurons have a higher NrCAM density. Within the second week the difference decreases. In the third week of studied maturation, the NrCAM density in qv^{3J} mutant neurons appears to be higher than in control neurons. The higher NrCAM density in qv^{3J} mutant neurons within the third week seems inappropriate, since the effect of the mutation was observed to be minor in immature neurons and major in mature neurons (dicussion: 7.2). Possibly, the culture density falsifies the results (figure: 71). No further experiments were performed in order to investigate, if there is an additional role of NrCAM within qv^{3J} mutant neurons.
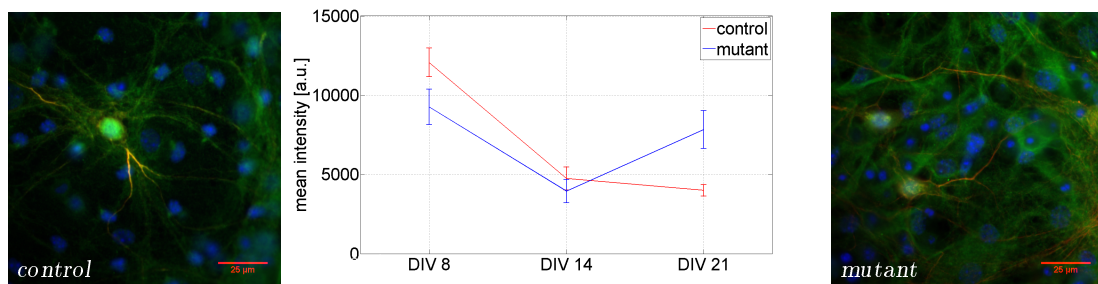

Figure 71: NrCAM in control and qv^{3J} mutant neurons. Double labeling of NrCAM (green) and ankG (C-terminal antibody, sc-28561, 11.2) (red) at *DIV 21*. Nucleus stained by DAPI (blue). Scale bar: 25.0 µm. Graph: NrCAM expression in control and qv^{3J} mutant neurons at three maturation stages. The graphic shows the mean fluorescence intensities [a.u.] at the AIS within the distance 0 - 50.0 µm from the soma or first branching point. N(control) = 12, 11, 12. N(mutant) = 10, 10, 9. The error is the SEM.

**NrCAM organization in wildtypes is regionally periodic.**

The neuronal cell adhesion molecule (NrCAM) binds ankG by a cytoplasmic binding domain (FIGQY) regulated by phosphorylation.[88] [133] The binding of NrCAM to ankG leads to the expectation of a similar organization as found for VGSCs (organized (semi-)periodic). Mainly, NrCAM appears non-periodically organized, only small periodic regions are found. The power spectra are noisy. The mean power spectrum has a small, non-significant power peak at the frequency of about 200 nm. Likely, the large distance between the extracellular labeling positions at the NrCAM molecules and the underlying periodic cytoskeleton does not allow to resolve the underlying periodic structure. A more prominent organization might be obtained by an antibody targeting a cytoplasmic located epitope.
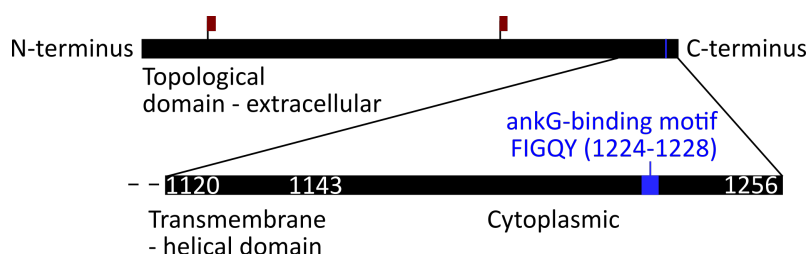
Figure 72: Schematic view of NrCAM isoform1. NrCAM has a large extracellular domain (1120 aa), a small transmembrane domain (23 aa) and a cytoplasmic domain (139 aa). About five sixth of its sequence belongs to the topological domain. The ankG binding motif (aa1224-1228) is located at the cytoplasmic domain. The antibody has been raised against synthetic peptides corresponding to two parts of the topological domain (aa153-174 and aa837-856 (red), published[134]). White numbers indicate the relative starting and ending amino acids to the three domains. *Established after Uniprot.org: Q810U4.*
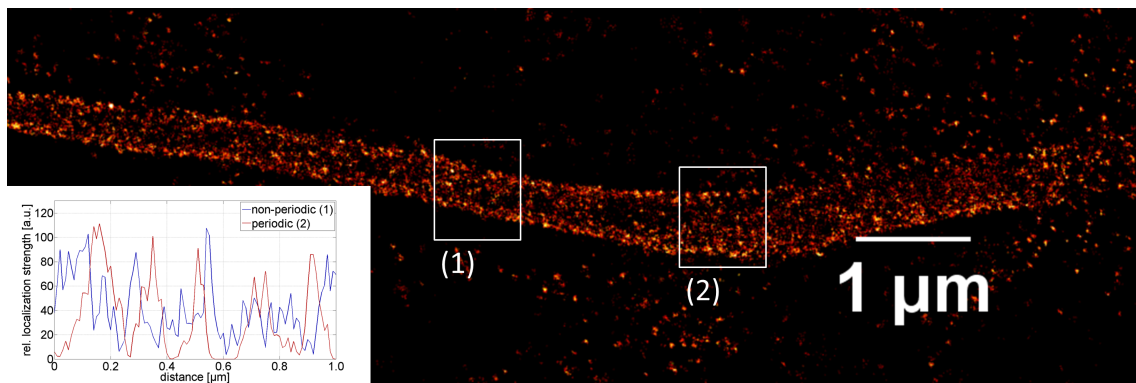
(a) Example AIS: Marked (1) area of non-periodic NrCAM organization. (2) area of periodic NrCAM organization.
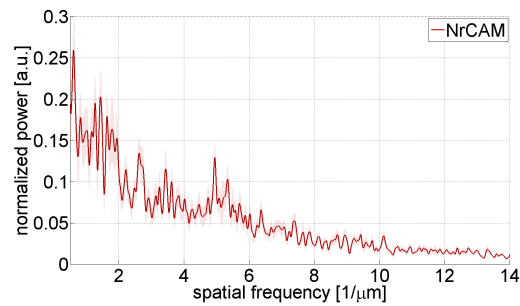

(b) The mean power spectrum calculated from complete

NrCAM data set.

Figure 73: NrCAM in control neurons at the age of *DIV 14*. (a) Example image of an AIS labeled for NrCAM including marked areas of non-periodic (1) and periodic (2) organization. (b) The mean power spectrum calculated from the complete NrCAM data set. N = 34. Error is the SEM.

11 Appendix C

11.1 Kolmogorov-Smirnov-Test

The significance of the maturation progress and between control and qv^{3J} mutant neurons was tested with Kolmogorov-Smirnov-Tests. The tests were performed on the mean fluorescence intensities (without SEM). The significance level is 5.0 %. A p-value (p = probability for significant difference in %) equal or greater than 95.0 % is taken as a significant difference between the two tested groups. Otherwise, a p-value below 95.0 % is set as a non-significant difference, the two tested groups are identified as equal or similar.

(a) VGSCs   (b) βIV-spectrin labeled N-terminal
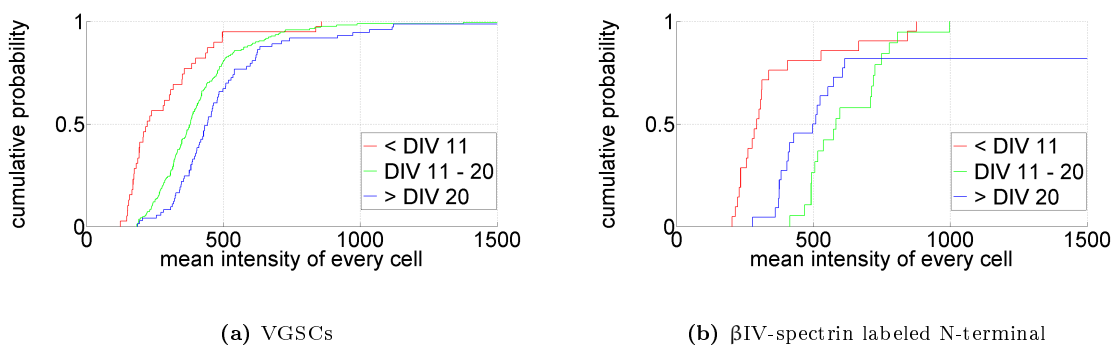
Figure 74: Two example graphs of VGSCs and βIV-spectrin (labeled N-terminal) with maturation in wildtype neurons. Kolmogorov-Smirnov-Tests between groups < *DIV 11, DIV 11 - 20 and > 20.* (a) VGSCs, (b) βIV-spectrin labeled N-terminal.

The probability of differences between the three maturation stages is summarized in table 1. In all cases the groups are found to be significantly different, except ankG (C-terminal labeled) within the first two weeks ($< DIV\ 11,\ DIV\ 11\ \text{-}\ 20$) is found as similar.

Table 1: Significance of matural differences in wildtypes. All three groups were tested against each other for significant differences: p ($< DIV\ 11,\ DIV\ 11\ \text{-}\ 20$), p ($< DIV\ 11,\ > DIV\ 20$) and p ($DIV\ 11\ \text{-}\ 20,\ > DIV\ 20$).

		in [%]
βIV-spectrin labeled N-terminal	p ($< DIV\ 11,\ DIV\ 11\ \text{-}\ 20$)	≈ 100.00
	p ($< DIV\ 11,\ > DIV\ 20$)	≈ 100.00
	p ($DIV\ 11\ \text{-}\ 20,\ > DIV\ 20$)	≈ 95.30
βIV-spectrin labeled C-terminal	p ($< DIV\ 11,\ DIV\ 11\ \text{-}\ 20$)	≈ 100.00
	p ($< DIV\ 11,\ > DIV\ 20$)	≈ 100.00
	p ($DIV\ 11\ \text{-}\ 20,\ > DIV\ 20$)	≈ 95.05
ankG labeled N-terminal	p ($< DIV\ 11,\ DIV\ 11\ \text{-}\ 20$)	≈ 100.00
	p ($< DIV\ 11,\ > DIV\ 20$)	≈ 100.00
	p ($DIV\ 11\ \text{-}\ 20,\ > DIV\ 20$)	≈ 99.77
ankG labeled C-terminal	p ($<$ DIV 11, DIV 11 - 20)	≈ 80.33
	p ($< DIV\ 11,\ > DIV\ 20$)	≈ 100.00
	p ($DIV\ 11\ \text{-}\ 20,\ > DIV\ 20$)	≈ 98.90
VGSCs	p ($< DIV\ 11,\ DIV\ 11\ \text{-}\ 20$)	≈ 100.00
	p ($< DIV\ 11,\ > DIV\ 20$)	≈ 100.00
	p ($DIV\ 11\ \text{-}\ 20,\ > DIV\ 20$)	≈ 99.63
Na$_v$1.6	p ($< DIV\ 11,\ DIV\ 11\ \text{-}\ 20$)	≈ 100.00
	p ($< DIV\ 11,\ > DIV\ 20$)	≈ 100.00
	p ($DIV\ 11\ \text{-}\ 20,\ > DIV\ 20$)	≈ 100.00
Na$_v$1.2	p ($< DIV\ 11,\ DIV\ 11\ \text{-}\ 20$)	≈ 100.00
	p ($< DIV\ 11,\ > DIV\ 20$)	≈ 100.00
	p ($DIV\ 11\ \text{-}\ 20,\ > DIV\ 20$)	≈ 100.00

The probability of differences between the three maturation stages is summarized in table 2. For control neurons, in most cases a significant difference is found. Exceptions are ankG (N-terminal labeled) between week two and three and ankG (C-terminal labeled) between week one and two. The maturation in qv^{3J} mutant neurons appears less clear. For VGSCs no differences are found between the first two weeks of maturation. For ankG (N-terminal labeled) only between the first two weeks a significant difference is identified. For ankG (C-terminal labeled) no significant difference between week one and three is identified.

Table 2: Significance of matural differences in control and qv^{3J} mutant neurons. All three groups were tested against each other for significant differences: p ($< DIV\ 11,\ DIV\ 11$ - 20), p ($< DIV\ 11,\ > DIV\ 20$) and p (DIV 11 - $20,\ > DIV\ 20$).

		control in [%]	mutant in [%]
VGSCs	p ($< DIV\ 11,\ DIV\ 11$ - 20)	≈ 99.91	≈ 81.41
	p ($< DIV\ 11,\ > DIV\ 20$)	≈ 100.00	≈ 95.25
	p ($DIV\ 11$ - $20,\ > DIV\ 20$)	≈ 99.91	≈ 99.92
ankG labeled N-terminal	p ($< DIV\ 11,\ DIV\ 11$ - 20)	≈ 100.00	≈ 99.45
	p ($< DIV\ 11,\ > DIV\ 20$)	≈ 100.00	≈ 82.00
	p ($DIV\ 11$ - $20,\ > DIV\ 20$)	≈ 1.40	≈ 4.23
ankG labeled C-terminal	p ($< DIV\ 11,\ DIV\ 11$ - 20)	≈ 100.00	≈ 100.00
	p ($< DIV\ 11,\ > DIV\ 20$)	≈ 65.86	≈ 27.21
	p ($DIV\ 11$ - $20,\ > DIV\ 20$)	≈ 99.25	≈ 100.00

The following table (table: 3) summarizes the probability of differences between control and qv^{3J} mutant neurons. VGSCs and ankG (C- and N-terminal labeled) show a significant difference. Exception is ankG (C-terminal labeled) at $< DIV\ 11$, which reveals no differences between control and qv^{3J} mutant neurons.

Table 3: Significance of differences between control and qv^{3J} mutant neurons. Control and qv^{3J} mutant neurons were tested for significant differences: p (control, $DIV\ 11$ - 20), p ($< DIV\ 11$, $> DIV\ 20$) and p ($DIV\ 11$ - 20, $> DIV\ 20$).

		p (control, qv^{3J}) in [%]
VGSCs	$< DIV\ 11$	≈ 99.93
	$DIV\ 11$ - 20	≈ 100.00
	$> DIV\ 20$	≈ 100.00
ankG labeled N-terminal	$< DIV\ 11$	≈ 95.39
	$DIV\ 11$ - 20	≈ 100.00
	$> DIV\ 20$	≈ 99.82
ankG labeled C-terminal	$< DIV\ 11$	≈ 79.09
	$DIV\ 11$ - 20	≈ 100.00
	$> DIV\ 20$	≈ 94.20
NrCAM	$< DIV\ 11$	≈ 89.28
	$DIV\ 11$ - 20	≈ 99.54
	$> DIV\ 20$	≈ 96.48
βII-spectrin	$< DIV\ 11$	≈ 63.12
	$DIV\ 11$ - 20	≈ 42.69
	$> DIV\ 20$	≈ 77.03

11.2   Antibodies

Primary antibodies were always used with the same secondary antibody for the same project part. In most cases for wide-field ("2nd antibody wide-field") and STORM ("2nd antibody STORM") imaging different secondaries were applied as noted in the table.

Exceptions are described below.

Table 4: Complete list of primary antibodies and the corresponding secondary antibodies displayed separately for wide-field and STORM imaging.

1st antibody	c[µg/mL]	2nd antibody wide-field	2nd antibody STORM
anti-panNav monoclonal *Sigma-Aldrich* S8809-1MG Lot#: SLBF1242 and SLBL1663V	1.1	anti-mouse (goat) IgG Alexa 488 *Molecular Probes* A11029 Lot#: 1252783	anti-mouse (goat) IgG Alexa 647 *Molecular Probes* A21236 Lot#: 1156622
anti-βIV-spectrin polyclonal *Rasband* gift from *Rasband lab,* *Baylor College of Medicine* C-terminal (aa2237-2253)	N.A.	anti-rabbit (goat) IgG Alexa 488 *Jackson ImmunoResearch* 111-545-003 Lot#: 107909	anti-rabbit (goat) IgG Alexa 647 *Molecular Probes* A21245 Lot#: 1219863
anti-βIV-spectrin polyclonal *OriGene* TA317365 Lot#: 51117 N-terminal (aa2-14)	2.5	anti-goat (donkey) - IgG Alexa 647 *Molecular Probes* A21447 Lot#: 1301819	anti-goat (donkey) IgG Alexa 647 *Molecular Probes* A21447 Lot#: 1301819
anti-βIV-spectrin polyclonal *ATLAS* HPA043370 Lot#: R39720, A96519 central (aa1142-1235)	1.0	anti-rabbit (goat) IgG Alexa 488 *Jackson ImmunoResearch* 111-545-003 Lot#: 107909	anti-rabbit (goat) IgG Alexa 647 *Molecular Probes* A21245 Lot#: 1219863

anti-βIV-spectrin polyclonal *Santa Cruz* sc-131789 Lot#: G0610 C-terminal (aa2350-2400)	2.5	anti-goat (donkey) IgG Alexa 647 *Molecular Probes* A21447 Lot#: 1301819	anti-goat (donkey) IgG Alexa 647 *Molecular Probes* A21447 Lot#: 1301819
anti-ankG monoclonal *Santa Cruz* sc-12719 Lot#: I0414 N - terminal, spectrin- binding domain (aa982-1107)	1.0	anti-mouse (goat) IgG Alexa 488 *Molecular Probes* A11029 Lot#: 1252783	anti-mouse (goat) IgG Alexa 647 *Molecular Probes* A21236 Lot#: 1156622
anti-ankG polyclonal *Santa Cruz* sc-28561 Lot#: F1511 C-terminal (aa4163-4377)	1.0	anti-rabbit (goat) IgG Alexa 488 *Jackson ImmunoResearch* 111-545-003 Lot#: 107909	anti-rabbit (goat) IgG Alexa 647 *Molecular Probes* A21245 Lot#: 1219863
anti-ankG polyclonal *Santa Cruz* sc-31778 Lot#: F0514 C-terminal (aa4150-4200)	1.0	anti-goat (chicken) IgG Alexa 647 *Molecular Probes* A21469 Lot#: 1584272	anti-goat (chicken) IgG Alexa 647 *Molecular Probes* A21469 Lot#: 1584272
anti-MAP2 polyclonal *abcam* ab5392 Lot#: G2128901-2	9.5	anti-chicken (goat) IgG Alexa 647 *Molecular Probes* A214469 Lot#: 1149008 anti-chicken (donkey) IgG Alexa 488 *Jackson ImmunoResearch* 703-545-155 Lot#: 113085	anti-chicken (donkey) IgG Alexa 488 *Jackson ImmunoResearch* 703-545-155 Lot#: 113085

anti-βII-spectrin monoclonal *Santa Cruz* sc-136074 Lot#: C2912	0.5	anti-mouse (goat) IgG Alexa 488 *Molecular Probes* A11029 Lot#: 1252783 anti-mouse (goat) IgG Alexa 647 *Molecular Probes* A21236 Lot#: 1156622	anti-mouse (goat) IgG Alexa 647 *Molecular Probes* A21236 Lot#: 1156622
anti-NrCAM polyclonal *abcam* ab24344 Lot#: GR185066-1	N.A.	anti-rabbit (goat) IgG Alexa 647 *Molecular Probes* A21245 Lot#: 1219863	anti-rabbit (goat) IgG Alexa 647 *Molecular Probes* A21245 Lot#: 1219863
anti-Na$_v$1.6 polyclonal *Alomone* ASC-009 Lot#: ASC009AN1650	4.0	anti-rabbit (goat) IgG Alexa 488 *Jackson ImmunoResearch* 111-545-003 Lot#: 107909	anti-rabbit (goat) IgG Alexa 647 *Molecular Probes* A21245 Lot#: 1219863
anti-Na$_v$1.6 monoclonal *Neuromab* 75-026 Lot#: 455-2JD-71	10.0	anti-mouse (goat) IgG Alexa 488 *Molecular Probes* A11029 Lot#: 1252783	not performed
anti-Na$_v$1.6 *Rasband* gift from *Rasband lab*, *Baylor College of Medicine*	N.A.	anti-rabbit (goat) IgG Alexa 488 *Jackson ImmunoResearch* 111-545-003 Lot#: 107909	not performed
anti-Na$_v$1.2 monoclonal *Neuromab* SMC-373D Lot#: 1007	2.5	anti-mouse (goat) IgG Alexa 488 *Molecular Probes* A11029 Lot#: 1252783	anti-mouse (goat) IgG Alexa 647 *Molecular Probes* A21236 Lot#: 1156622

anti-Na$_v$1.2	2.0	anti-rabbit (goat)	anti-rabbit (goat)
polyclonal		IgG	IgG
Alomone		Alexa 488	Alexa 647
ASC-002		*Jackson ImmunoResearch*	*Molecular Probes*
Lot#:		111-545-003	A21245
ASC002AN1650		Lot#: 107909	Lot#: 1219863

Exceptions

Often double labeling with anti-ankG (N- and C-terminal) was performed for an easy AIS identification. For wide-field imaging ankG received an Alexa 488 or Alexa 647 dye depending on which dye was marked as the standard for the protein double labeled with. For STORM imaging ankG received an Alexa 488 (example experiments: 10.3, 49).

For double labeling of ankG N-terminal and C-terminal received ankG N-terminal an Alexa 647 carrying antibody, whereas the C-terminal received the Alexa 488 carrying antibody (experiments: 9.1.2) For double labeling of anti-βIV-spectrin from *OriGene* with another primary antibody raised in rabbit, cross-reactions were observed when using anti-rabbit secondaries raised in goat. Consequently, the secondaries were changed to anti-goat (chicken), IgG, Alexa 647, *Molecular Probes*, A21469, Lot#: 1584272 and anti-rabbit (donkey), IgG, Alexa 488, *abcam*, 1584272 (experiments: 9.1.1).

Bibliography

[1] Nicholas J Parkinson, Christine L Olsson, Janice L Hallows, Jennifer McKee-Johnson, Bart P Keogh, Konrad Noben-Trauth, Sharon G Kujawa, Bruce L Tempel, "Mutant β-spectrin 4 causes auditory and motor neuropathies in quivering mice" *Nature genetics* (2001) **29**(1), 61–65.

[2] Ilya A Fleidervish, Nechama Lasser-Ross, Michael J Gutnick, William N Ross, "Na+ imaging reveals little difference in action potential-evoked Na+ influx between axon and soma" *Nature neuroscience* (2010) **13**(7), 852–860.

[3] Maarten HP Kole, Greg J Stuart, "Signal processing in the axon initial segment" *Neuron* (2012) **73**(2), 235–247.

[4] Matthew J Craner, Albert C Lo, Joel A Black, Stephen G Waxman, "Abnormal sodium channel distribution in optic nerve axons in a model of inflammatory demyelination" *Brain* (2003) **126**(7), 1552–1561.

[5] Matthew S Grubb, Juan Burrone, "Building and maintaining the axon initial segment" *Current opinion in neurobiology* (2010) **20**(4), 481–488.

[6] Matthew S Grubb, Yousheng Shu, Hiroshi Kuba, Matthew N Rasband, Verena C Wimmer, Kevin J Bender, "Short-and long-term plasticity at the axon initial segment" *The Journal of Neuroscience* (2011) **31**(45), 16049–16055.

[7] Scott M Jenkins, Vann Bennett, "Ankyrin-G coordinates assembly of the spectrin-based membrane skeleton, voltage-gated sodium channels, and L1 CAMs at Purkinje neuron initial segments" *The Journal of cell biology* (2001) **155**(5), 739–746.

[8] Tatiana Boiko, Audra Van Wart, John H Caldwell, S Rock Levinson, James S Trimmer, Gary Matthews, "Functional specialization of the axon initial segment by isoform-specific sodium channel targeting" *The Journal of neuroscience* (2003) **23**(6), 2306–2313.

[9] Verena C Wimmer, Christopher A Reid, Eva Y-W So, Samuel F Berkovic, Steven Petrou, "Axon initial segment dysfunction in epilepsy" *The Journal of physiology* (2010) **588**(11), 1829–1840.

[10] Timothy J Byers, Daniel Branton, "Visualization of the protein associations in the

erythrocyte membrane skeleton" *Proceedings of the National Academy of Sciences* (1985) **82**(18), 6153–6157.

[11] Ke Xu, Guisheng Zhong, Xiaowei Zhuang, "Actin, spectrin, and associated proteins form a periodic cytoskeletal structure in axons" *Science* (2013) **339**(6118), 452–456.

[12] Guisheng Zhong, Jiang He, Ruobo Zhou, Damaris Lorenzo, Hazen P Babcock, Vann Bennett, Xiaowei Zhuang, Robert H Singer, "Developmental mechanism of the periodic membrane skeleton in axons." *eLife* (2014) **3**.

[13] Christophe Leterrier, Jean Potier, Ghislaine Caillol, Fanny Rueda Boroni, Bénédicte Dargent, "Nanoscale architecture of the axon initial segment reveals an organized and robust scaffold" *bioRxiv* (2015) , 022962.

[14] Keith Burridge, Thomas Kelly, Paul Mangeat, "Nonerythrocyte spectrins: actin-membrane attachment proteins occurring in many cell types." *The Journal of cell biology* (1982) **95**(2), 478–486.

[15] Steven R Goodman, Warren E Zimmer, Mary Blair Clark, Ian S Zagon, Jane E Barker, Michael L Bloom, "Brain spectrin: of mice and men" *Brain research bulletin* (1995) **36**(6), 593–606.

[16] Stanny Berghs, Diego Aggujaro, Ronald Dirkx, Elena Maksimova, Paul Stabach, Jean-Michel Hermel, Jian-Ping Zhang, William Philbrick, Vladimir Slepnev, Tatiana Ort et al., "βIV spectrin, a new spectrin localized at axon initial segments and nodes of Ranvier in the central and peripheral nervous system" *The Journal of cell biology* (2000) **151**(5), 985–1002.

[17] Masayuki Komada, Philippe Soriano, "βIV-spectrin regulates sodium channel clustering through ankyrin-G at axon initial segments and nodes of Ranvier" *The Journal of cell biology* (2002) **156**(2), 337–348.

[18] Sandra Lacas-Gervais, Jun Guo, Nicola Strenzke, Eric Scarfone, Melanie Kolpe, Monika Jahkel, Pietro De Camilli, Tobias Moser, Matthew N Rasband, Michele Solimena, "βIVΣ1 spectrin stabilizes the nodes of Ranvier and axon initial segments" *The Journal of cell biology* (2004) **166**(7), 983–990.

[19] Beata Machnicka, Aleksander Czogalla, Anita Hryniewicz-Jankowska, Dżamila M Bogusławska, Renata Grochowalska, Elżbieta Heger, Aleksander F Sikorski, "Spectrins: A structural platform for stabilization and activation of membrane channels, receptors and transporters" *Biochimica et Biophysica Acta (BBA)-Biomembranes* (2014) **1838**(2), 620–634.

[20] P Somogyu, J Hamori, "A quantitative electron microscopic study of the Purkinje cell axon initial segment" *Neuroscience* (1976) **1**(5), 361–IN3.

[21] Debra A Wollner, William A Catterall, "Localization of sodium channels in axon hillocks and initial segments of retinal ganglion cells" *Proceedings of the National Academy of Sciences* (1986) **83**(21), 8424–8428.

[22] Neil A Campbell, Jane B Reece, Jürgen Markl, "Biologie. 6" *Aufl. Heidelberg: Spektrum* (2003).

[23] Shelley I Fried, Aaron CW Lasker, Neal J Desai, Donald K Eddington, Joseph F Rizzo, "Axonal sodium-channel bands shape the response to electric stimulation in retinal ganglion cells" *Journal of neurophysiology* (2009) **101**(4), 1972–1987.

[24] Matthew S Grubb, Juan Burrone, "Activity-dependent relocation of the axon initial segment fine-tunes neuronal excitability" *Nature* (2010) **465**(7301), 1070–1074.

[25] Matthew N Rasband, "The axon initial segment and the maintenance of neuronal polarity" *Nature Reviews Neuroscience* (2010) **11**(8), 552–562.

[26] Andrea Lorincz, Zoltan Nusser, "Molecular identity of dendritic voltage-gated sodium channels" *Science* (2010) **328**(5980), 906–909.

[27] Zoltan Nusser, "Differential subcellular distribution of ion channels and the diversity of neuronal function" *Current opinion in neurobiology* (2012) **22**(3), 366–371.

[28] Costa M Colbert, Enhui Pan, "Ion channel properties underlying axonal action potential initiation in pyramidal neurons" *Nature neuroscience* (2002) **5**(6), 533–538.

[29] Andrea Lorincz, Zoltan Nusser, "Cell-type-dependent molecular composition of the axon initial segment" *The Journal of Neuroscience* (2008) **28**(53), 14329–14340.

[30] Lucy M Palmer, Greg J Stuart, "Site of action potential initiation in layer 5 pyramidal neurons" *The Journal of neuroscience* (2006) **26**(6), 1854–1863.

[31] Wenqin Hu, Cuiping Tian, Tun Li, Mingpo Yang, Han Hou, Yousheng Shu, "Distinct contributions of Nav1. 6 and Nav1. 2 in action potential initiation and backpropagation" *Nature neuroscience* (2009) **12**(8), 996–1002.

[32] Ekaterini Kordeli, Stephen Lambert, Vann Bennett, "Ankyrin A NEW ANKYRIN GENE WITH NEURAL-SPECIFIC ISOFORMS LOCALIZED AT THE AXONAL INITIAL SEGMENT AND NODE OF RANVIER" *Journal of Biological Chemistry* (1995) **270**(5), 2352–2359.

[33] James L Salzer, "Polarized domains of myelinated axons" *Neuron* (2003) **40**(2), 297–318.

[34] Kristian L Hedstrom, Xiaorong Xu, Yasuhiro Ogawa, Renato Frischknecht, Constanze I Seidenbecher, Peter Shrager, Matthew N Rasband, "Neurofascin assembles a specialized extracellular matrix at the axon initial segment" *The Journal of cell biology* (2007) **178**(5), 875–886.

[35] Bettina Winckler, Paul Forscher, Ira Mellman, "A diffusion barrier maintains distribution of membrane proteins in polarized neurons" *Nature* (1999) **397**(6721), 698–701.

[36] Jürgen-Markus Sobotzik, Jana Maria Sie, Chrisoula Politi, Domenico Del Turco, Vann Bennett, Thomas Deller, Christian Schultz, "AnkyrinG is required to maintain axo-dendritic polarity in vivo" *Proceedings of the National Academy of Sciences* (2009) **106**(41), 17564–17569.

[37] Lydia H Davis, Vann Bennett, "Identification of two regions of beta G spectrin that bind to distinct sites in brain membranes." *Journal of Biological Chemistry* (1994) **269**(6), 4409–4416.

[38] Jyoti Dhar Malhotra, Kristin Kazen-Gillespie, Michael Hortsch, Lori L Isom, "Sodium channel β subunits mediate homophilic cell adhesion and recruit ankyrin to points of cell-cell contact" *Journal of Biological Chemistry* (2000) **275**(15), 11383–11388.

[39] Yumi Matsuoka, X Li, Vann Bennett, "Adducin: structure, function and regulation" *Cellular and Molecular Life Sciences CMLS* (2000) **57**(6), 884–895.

[40] David M Shotton, Brian E Burke, Daniel Branton, "The molecular structure of human erythrocyte spectrin: biophysical and electron microscopic studies" *Journal of molecular biology* (1979) **131**(2), 303–329.

[41] Vann Bennett, Daniel Branton, "Selective association of spectrin with the cytoplasmic surface of human erythrocyte plasma membranes. Quantitative determination with purified (32P) spectrin." *Journal of Biological Chemistry* (1977) **252**(8), 2753–2763.

[42] Vann Bennett, Peter J Stenbuck, "Identification and partial purification of ankyrin, the high affinity membrane attachment site for human erythrocyte spectrin." *Journal of Biological Chemistry* (1979) **254**(7), 2533–2541.

[43] Shih-Chun Liu, Laura H Derick, Jiri Palek, "Visualization of the hexagonal lattice in the erythrocyte membrane skeleton." *The Journal of cell biology* (1987) **104**(3), 527–536.

[44] DW Speicher, Ludmila Weglarz, Tara M DeSilva, "Properties of human red cell spectrin heterodimer (side-to-side) assembly and identification of an essential nucleation site." *Journal of Biological Chemistry* (1992) **267**(21), 14775–14782.

[45] Jonathan Q Davis, Vann Bennett, "Brain ankyrin. A membrane-associated protein with binding sites for spectrin, tubulin, and the cytoplasmic domain of the erythrocyte anion channel." *Journal of Biological Chemistry* (1984) **259**(21), 13550–13559.

[46] Jonathan Q Davis, Tanya McLaughlin, Vann Bennett, "Ankyrin-binding proteins related to nervous system cell adhesion molecules: candidates to provide transmembrane and intercellular connections in adult brain." *The Journal of cell biology* (1993) **121**(1), 121–133.

[47] Michael Hortsch, K Sue O'shea, Guangyan Zhao, Feodor Kim, Yolanda Vallejo, Ronald R Dubreuil, "A conserved role for L1 as a transmembrane link between neuronal adhesion and membrane cytoskeleton assembly" *Cell Communication and Adhesion* (1998) **5**(1), 61–73.

[48] Anthony J Baines, "The spectrin–ankyrin–4.1–adducin membrane skeleton: adapting eukaryotic cells to the demands of animal life" *Protoplasma* (2010) **244**(1-4), 99–131.

[49] Elior Peles, James L Salzer, "Molecular domains of myelinated axons" *Current opinion in neurobiology* (2000) **10**(5), 558–565.

[50] VT Marchesi, E Steers, "Selective solubilization of a protein component of the red cell membrane" *Science* (1968) **159**(3811), 203–204.

[51] Nicholas H Putnam, Mansi Srivastava, Uffe Hellsten, Bill Dirks, Jarrod Chapman, Asaf Salamov, Astrid Terry, Harris Shapiro, Erika Lindquist, Vladimir V Kapitonov et al., "Sea anemone genome reveals ancestral eumetazoan gene repertoire and genomic organization" *science* (2007) **317**(5834), 86–94.

[52] Y Yan, E Winograd, A Viel, T Cronin, SC Harrison, D Branton, "Crystal structure of the repetitive segments of spectrin" *Science* (1993) **262**(5142), 2027–2030.

[53] AnthonyJ Baines, "Evolution of spectrin function in cytoskeletal and membrane networks" *Biochemical Society Transactions* (2009) **37**(4), 796.

[54] A Viel, MS Gee, L Tomooka, D Branton, "Motifs involved in interchain binding at the tail-end of spectrin" *Biochimica et Biophysica Acta (BBA)-Protein Structure and Molecular Enzymology* (1998) **1384**(2), 396–404.

[55] WT Tse, MC Lecomte, FF Costa, M Garbarz, C Feo, P Boivin, D Dhermy, BG Forget, "Point mutation in the beta-spectrin gene associated with alpha I/74 hereditary elliptocytosis. Implications for the mechanism of spectrin dimer self-association." *Journal of Clinical Investigation* (1990) **86**(3), 909.

[56] Lisa Cherry, Nick Menhart, Leslie Wo-Mei Fung, "Interactions of the α-Spectrin N-terminal Region with β-Spectrin IMPLICATIONS FOR THE SPECTRIN TETRAMERIZATION REACTION" *Journal of Biological Chemistry* (1999) **274**(4), 2077–2084.

[57] Jonathan J Ipsaro, Sandra L Harper, Troy E Messick, Ronen Marmorstein, Alfonso Mondragón, David W Speicher, "Crystal structure and functional interpretation of the erythrocyte spectrin tetramerization domain complex" *Blood* (2010) **115**(23), 4843–4852.

[58] Ernst UNGEWICKELL, Walter GRATZER, "Self-Association of Human Spectrin" *European Journal of Biochemistry* (1978) **88**(2), 379–385.

[59] Alain Viel, Daniel Branton, "Spectrin: on the path from structure to function" *Current opinion in cell biology* (1996) **8**(1), 49–55.

[60] Vann Bennett, Diana M Gilligan, "The spectrin-based membrane skeleton and micron-scale organization of the plasma membrane" *Annual review of cell biology* (1993) **9**(1), 27–66.

[61] Joacim Robertsson, Katja Petzold, L Lofvenberg, Lars Backman, "Folding of spectrin's SH3 domain in the presence of spectrin repeats" *Cellular and Molecular Biology Letters* (2005) **10**(4), 595.

[62] Scott P Kennedy, Stephen L Warren, Bernard G Forget, Jon S Morrow, "Ankyrin binds to the 15th repetitive unit of erythroid and nonerythroid beta-spectrin." *The Journal of Cell Biology* (1991) **115**(1), 267–277.

[63] Jonathan J Ipsaro, Lei Huang, Alfonso Mondragón, "Structures of the spectrin-ankyrin interaction binding domains" *Blood* (2009) **113**(22), 5385–5393.

[64] Yang Yang, Yasuhiro Ogawa, Kristian L Hedstrom, Matthew N Rasband, "βIV spectrin is recruited to axon initial segments and nodes of Ranvier by ankyrinG" *The Journal of cell biology* (2007) **176**(4), 509–519.

[65] Yogambal Srinivasan, Lawrence Elmer, Jonathan Davis, Vann Bennett, Kimon Angelides, "Ankyrin and spectrin associate with voltage-dependent sodium channels in brain" *Nature* (1988).

[66] Vann Bennett, Stephen Lambert, Jonathan Q Davis, Xu Zhang, "Molecular architecture of the specialized axonal membrane at the node of Ranvier" *Society of General Physiologists series* (1997) **52**, 107–122.

[67] Vann Bennett, Anthony J Baines, "Spectrin and ankyrin-based pathways: metazoan inventions for integrating cells into tissues" *Physiological reviews* (2001) **81**(3), 1353–1392.

[68] Zongming Pan, Tingching Kao, Zsolt Horvath, Julia Lemos, Jai-Yoon Sul, Stephen D Cranstoun, Vann Bennett, Steven S Scherer, Edward C Cooper, "A common ankyrin-G-based mechanism retains KCNQ and NaV channels at electrically active domains of the axon" *The Journal of neuroscience* (2006) **26**(10), 2599–2613.

[69] Helen C Lai, Lily Y Jan, "The distribution and targeting of neuronal voltage-gated ion channels" *Nature Reviews Neuroscience* (2006) **7**(7), 548–562.

[70] David Kapfhamer, Diane E Miller, Stephen Lambert, Vann Bennett, Thomas W Glover, Margit Burmeister, "Chromosomal localization of the ankyrinG gene (ANK3/Ank3) to human 10q21 and mouse 10" *Genomics* (1995) **27**(1), 189–191.

[71] Peter Michaely, Diana R Tomchick, Mischa Machius, Richard GW Anderson, "Crystal structure of a 12 ANK repeat stack from human ankyrinR" *The EMBO journal* (2002) **21**(23), 6387–6396.

[72] V Bennett et al., "Ankyrins. Adaptors between diverse plasma membrane proteins and the cytoplasm" *J. Biol. Chem* (1992) **267**(13), 8703–8706.

[73] Paul M Jenkins, Namsoo Kim, Steven L Jones, Wei Chou Tseng, Tatyana M Svitkina, Henry H Yin, Vann Bennett, "Giant ankyrin-G: A critical innovation in vertebrate evolution of fast and integrated neuronal signaling" *Proceedings of the National Academy of Sciences* (2015) **112**(4), 957–964.

[74] Peter Michaely, Vann Bennett, "The membrane-binding domain of ankyrin contains four independently folded subdomains, each comprised of six ankyrin repeats." *Journal of Biological Chemistry* (1993) **268**(30), 22703–22709.

[75] Stephen Lambert, Jonathan Q Davis, Vann Bennett, "Morphogenesis of the node of Ranvier: co-clusters of ankyrin and ankyrin-binding integral proteins define early developmental intermediates" *The Journal of neuroscience* (1997) **17**(18), 7025–7036.

[76] Daixing Zhou, Stephen Lambert, Peter L Malen, Scott Carpenter, Linda M Boland, Vann Bennett, "AnkyrinG is required for clustering of voltage-gated Na channels at axon initial

segments and for normal action potential firing" *The Journal of cell biology* (1998) **143**(5), 1295–1304.

[77] Guy Lemaillet, Barbara Walker, Stephen Lambert, "Identification of a conserved ankyrin-binding motif in the family of sodium channel α subunits" *Journal of Biological Chemistry* (2003) **278**(30), 27333–27339.

[78] Tammy Szu-Yu Ho, Daniel R Zollinger, Kae-Jiun Chang, Mingxuan Xu, Edward C Cooper, Michael C Stankewich, Vann Bennett, Matthew N Rasband, "A hierarchy of ankyrin-spectrin complexes clusters sodium channels at nodes of Ranvier" *Nature neuroscience* (2014).

[79] Ekaterini Kordeli, Jonathan Davis, Bruce Trapp, Vann Bennett, "An isoform of ankyrin is localized at nodes of Ranvier in myelinated axons of central and peripheral nerves." *The Journal of cell biology* (1990) **110**(4), 1341–1352.

[80] Vann Bennett, Stephen Lambert, "Physiological roles of axonal ankyrins in survival of premyelinated axons and localization of voltage-gated sodium channels" *Journal of neurocytology* (1999) **28**(4-5), 303–318.

[81] Jonathan Q Davis, Stephen Lambert, Vann Bennett, "Molecular composition of the node of Ranvier: identification of ankyrin-binding cell adhesion molecules neurofascin (mucin+/third FNIII domain-) and NrCAM at nodal axon segments." *The Journal of cell biology* (1996) **135**(5), 1355–1367.

[82] Xu Zhang, Vann Bennett, "Restriction of 480/270-kD ankyrin G to axon proximal segments requires multiple ankyrin G-specific domains" *The Journal of cell biology* (1998) **142**(6), 1571–1581.

[83] Wei Chou Tseng, Paul M Jenkins, Masashi Tanaka, Richard Mooney, Vann Bennett, "Giant ankyrin-G stabilizes somatodendritic GABAergic synapses through opposing endocytosis of GABAA receptors" *Proceedings of the National Academy of Sciences* (2015) **112**(4), 1214–1219.

[84] Anna Brachet, Christophe Leterrier, Marie Irondelle, Marie-Pierre Fache, Victor Racine, Jean-Baptiste Sibarita, Daniel Choquet, Bénédicte Dargent, "Ankyrin G restricts ion channel diffusion at the axonal initial segment before the establishment of the diffusion barrier" *The Journal of cell biology* (2010) **191**(2), 383–395.

[85] Kristian L Hedstrom, Yasuhiro Ogawa, Matthew N Rasband, "AnkyrinG is required for maintenance of the axon initial segment and neuronal polarity" *The Journal of cell biology* (2008) **183**(4), 635–640.

[86] Dorothy P Schafer, Smita Jha, Fudong Liu, Trupti Akella, Louise D McCullough, Matthew N Rasband, "Disruption of the axon initial segment cytoskeleton is a new mechanism for neuronal injury" *The Journal of Neuroscience* (2009) **29**(42), 13242–13254.

[87] Marie-Pierre Fache, Anissa Moussif, Fanny Fernandes, Pierre Giraud, Juan José Garrido, Bénédicte Dargent, "Endocytotic elimination and domain-selective tethering constitute a potential mechanism of protein segregation at the axonal initial segment" *The Journal of cell biology* (2004) **166**(4), 571–578.

[88] Timothy D Garver, Qun Ren, Shmuel Tuvia, Vann Bennett, "Tyrosine phosphorylation at a site highly conserved in the L1 family of cell adhesion molecules abolishes ankyrin binding and increases lateral mobility of neurofascin" *The Journal of cell biology* (1997) **137**(3), 703–714.

[89] Juan José Garrido, Pierre Giraud, Edmond Carlier, Fanny Fernandes, Anissa Moussif, Marie-Pierre Fache, Dominique Debanne, Bénédicte Dargent, "A targeting motif involved in sodium channel clustering at the axonal initial segment" *Science* (2003) **300**(5628), 2091–2094.

[90] Andreas Gasser, Tammy Szu-Yu Ho, Xiaoyang Cheng, Kae-Jiun Chang, Stephen G Waxman, Matthew N Rasband, Sulayman D Dib-Hajj, "An ankyrinG-binding motif is necessary and sufficient for targeting Nav1. 6 sodium channels to axon initial segments and nodes of Ranvier" *The Journal of Neuroscience* (2012) **32**(21), 7232–7243.

[91] William A Catterall, "Structure and function of voltage-gated sodium channels at atomic resolution" *Experimental physiology* (2014) **99**(1), 35–51.

[92] Helene Vacher, James S Trimmer, "Trafficking mechanisms underlying neuronal voltage-gated ion channel localization at the axon initial segment" *Epilepsia* (2012) **53**(s9), 21–31.

[93] Lori L Isom, KS De Jongh, DE Patton, BF Reber, J Offord, H Charbonneau, K Walsh, AL Goldin, WA Catterall, "Primary structure and functional expression of the beta 1 subunit of the rat brain sodium channel" *Science* (1992) **256**(5058), 839–842.

[94] Alan L Goldin, Robert L Barchi, John H Caldwell, Franz Hofmann, James R Howe, John C Hunter, Roland G Kallen, Gail Mandel, Miriam H Meisler, Yoheved Berwald Netter et al., "Nomenclature of voltage-gated sodium channels" *Neuron* (2000) **28**(2), 365–368.

[95] Ning Qin, Michael R D'Andrea, Mary-Lou Lubin, Navid Shafaee, Ellen E Codd, Ana M Correa, "Molecular cloning and functional expression of the human sodium channel β1B subunit, a novel splicing variant of the β1 subunit" *European journal of biochemistry* (2003) **270**(23), 4762–4770.

[96] Frank H Yu, Ruth E Westenbroek, Inmaculada Silos-Santiago, Kimberly A McCormick, Deborah Lawson, Pei Ge, Holly Ferriera, Jeremiah Lilly, Peter S DiStefano, William A Catterall et al., "Sodium channel beta4, a new disulfide-linked auxiliary subunit with similarity to beta2." *The Journal of neuroscience: the official journal of the Society for Neuroscience* (2003) **23**(20), 7577–7585.

[97] John H Caldwell, Kristin L Schaller, Robert S Lasher, Elior Peles, S Rock Levinson, "Sodium channel Nav1. 6 is localized at nodes of Ranvier, dendrites, and synapses" *Proceedings of the National Academy of Sciences* (2000) **97**(10), 5616–5620.

[98] Matthew N Rasband, James S Trimmer, "Developmental clustering of ion channels at and near the node of Ranvier" *Developmental biology* (2001) **236**(1), 5–16.

[99] Tatiana Boiko, Matthew N Rasband, S Rock Levinson, John H Caldwell, Gail Mandel, James S Trimmer, Gary Matthews, "Compact myelin dictates the differential targeting of two sodium channel isoforms in the same axon" *Neuron* (2001) **30**(1), 91–104.

[100] Charlotte F Ratcliffe, Ruth E Westenbroek, Rory Curtis, William A Catterall, "Sodium channel $\beta 1$ and $\beta 3$ subunits associate with neurofascin through their extracellular immunoglobulin-like domain" *The Journal of cell biology* (2001) **154**(2), 427–434.

[101] Matthew J Craner, Jia Newcombe, Joel A Black, Caroline Hartle, M Louise Cuzner, Stephen G Waxman, "Molecular changes in neurons in multiple sclerosis: altered axonal expression of Nav1. 2 and Nav1. 6 sodium channels and Na+/Ca2+ exchanger" *Proceedings of the National Academy of Sciences of the United States of America* (2004) **101**(21), 8168–8173.

[102] Miriam H Meisler, Nicholas W Plummer, Daniel L Burgess, David A Buchner, Leslie K Sprunger, "Allelic mutations of the sodium channel SCN8A reveal multiple cellular and physiological functions", In *Mutagenesis of the Mouse Genome* , 37–45. Springer (2004).

[103] Miriam H Meisler, Jennifer Kearney, Andrew Escayg, Bryan T Macdonald, Leslie K Sprunger, "Sodium channels and neurological disease: insights from Scn8a mutations in the mouse" *The Neuroscientist* (2001) **7**(2), 136–145.

[104] CH Yoon, EP Les, "Quivering, a new first chromosome mutation in mice" *Journal of Heredity* (1957) **48**(4), 176–180.

[105] Gregory R Bock, Marius P Frank, Karen P Steel, MS Deol, "The quivering mutant mouse: hereditary deafness of central origin" *Acta oto-laryngologica* (1983) **96**(5-6), 371–377.

[106] MS Deol, Marius P Frank, Karen P Steel, Gregory R Bock, "Genetic deafness of central origin" *Brain research* (1983) **258**(1), 177–179.

[107] Yang Yang, Sandra Lacas-Gervais, D Kent Morest, Michele Solimena, Matthew N Rasband, "βIV spectrins are essential for membrane stability and the molecular organization of nodes of Ranvier" *The Journal of neuroscience* (2004) **24**(33), 7230–7240.

[108] Michael J Rust, Mark Bates, Xiaowei Zhuang, "Sub-diffraction-limit imaging by stochastic optical reconstruction microscopy (STORM)" *Nature methods* (2006) **3**(10), 793–796.

[109] Ernst Abbe, "Beiträge zur Theorie des Mikroskops und der mikroskopischen Wahrnehmung" *Archiv für mikroskopische Anatomie* (1873) **9**(1), 413–418.

[110] George Patterson, Michael Davidson, Suliana Manley, Jennifer Lippincott-Schwartz, "Superresolution imaging using single-molecule localization" *Annual review of physical chemistry* (2010) **61**, 345.

[111] Sebastian van de Linde, Anna Löschberger, Teresa Klein, Meike Heidbreder, Steve Wolter, Mike Heilemann, Markus Sauer, "Direct stochastic optical reconstruction microscopy with standard fluorescent probes" *Nature protocols* (2011) **6**(7), 991–1009.

[112] Ulrike Endesfelder, Sebastian Malkusch, Benjamin Flottmann, Justine Mondry, Piotr Liguzinski, Peter J Verveer, Mike Heilemann, "Chemically induced photoswitching of fluorescent probes-a general concept for super-resolution microscopy" *Molecules* (2011) **16**(4), 3106–3118.

[113] Jie Wang, David A Richards, "Segregation of PIP2 and PIP3 into distinct nanoscale regions within the plasma membrane" *Biology open* (2012) **1**(9), 857–862.

[114] Xiaowei Zhuang, "Nano-imaging with STORM" *Nature photonics* (2009) **3**(7), 365.

[115] Graham T Dempsey, Joshua C Vaughan, Kok Hao Chen, Mark Bates, Xiaowei Zhuang, "Evaluation of fluorophores for optimal performance in localization-based super-resolution imaging" *Nature methods* (2011) **8**(12), 1027–1036.

[116] Peter Wardman, "Reduction potentials of one-electron couples involving free radicals in aqueous solution" *Journal of Physical and Chemical Reference Data* (1989) **18**(4), 1637–1755.

[117] Mike Heilemann, Peter Dedecker, Johan Hofkens, Markus Sauer, "Photoswitches: Key molecules for subdiffraction-resolution fluorescence imaging and molecular quantification" *Laser & Photonics Reviews* (2009) **3**(1-2), 180–202.

[118] Sebastian van de Linde, Ivan Krstić, Thomas Prisner, Sören Doose, Mike Heilemann, Markus Sauer, "Photoinduced formation of reversible dye radicals and their impact on super-resolution imaging" *Photochemical & Photobiological Sciences* (2011) **10**(4), 499–506.

[119] Bo Huang, Hazen Babcock, Xiaowei Zhuang, "Breaking the diffraction barrier: super-resolution imaging of cells" *Cell* (2010) **143**(7), 1047–1058.

[120] Nick Goeden, Alexandre Bonnin, "Ex vivo perfusion of mid-to-late-gestation mouse placenta for maternal-fetal interaction studies during pregnancy" *Nature protocols* (2013) **8**(1), 66–74.

[121] Gerard MJ Beaudoin III, Seung-Hye Lee, Dipika Singh, Yang Yuan, Yu-Gie Ng, Louis F Reichardt, Jyothi Arikkath, "Culturing pyramidal neurons from the early postnatal mouse hippocampus and cortex" *Nature protocols* (2012) **7**(9), 1741–1754.

[122] Steve Wolter, "rapid STORM manual" *http://www.super-resolution.de/home/rapidstorm/* (2012).

[123] William RJ Whitaker, Richard LM Faull, Henry J Waldvogel, Christopher J Plumpton, Piers C Emson, Jeffrey J Clare, "Comparative distribution of voltage-gated sodium channel proteins in human brain" *Molecular brain research* (2001) **88**(1), 37–53.

[124] Andrea Lorincz, Zoltan Nusser, "Specificity of immunoreactions: the importance of testing specificity in each method" *The Journal of neuroscience* (2008) **28**(37), 9083–9086.

[125] Jean-Marc Fritschy, "Is my antibody-staining specific? How to deal with pitfalls of immunohistochemistry" *European Journal of Neuroscience* (2008) **28**(12), 2365–2370.

[126] Matthew N Rasband, "Cytoskeleton: axons earn their stripes" *Current Biology* (2013) **23**(5), R197–R198.

[127] Beat M Riederer, Ian S Zagon, Steven R Goodman, "Brain spectrin (240/235) and brain spectrin (240/235E): two distinct spectrin subtypes with different locations within mammalian neural cells." *The Journal of cell biology* (1986) **102**(6), 2088–2097.

[128] Christian R Lombardo, Scott A Weed, Scott P Kennedy, Bernard G Forget, Jon S Morrow, "Beta II-spectrin (fodrin) and beta I epsilon 2-spectrin (muscle) contain NH2-and COOH-terminal membrane association domains (MAD1 and MAD2)." *Journal of Biological Chemistry* (1994) **269**(46), 29212–29219.

[129] Libo Yao, Paul Janmey, Luciano G Frigeri, Wei Han, Jun Fujita, Yuko Kawakami, John R Apgar, Toshiaki Kawakami, "Pleckstrin homology domains interact with filamentous actin" *Journal of Biological Chemistry* (1999) **274**(28), 19752–19761.

[130] G Elisabeth Pollerberg, Keith Burridge, Keith E Krebs, Steven R Goodman, Melitta Schachner, "The 180-kD component of the neural cell adhesion molecule N-CAM is involved in cell-cell contacts and cytoskeleton-membrane interactions" *Cell and tissue research* (1987) **250**(1), 227–236.

[131] Lisa M Sharkey, Xiaoyang Cheng, Valerie Drews, David A Buchner, Julie M Jones, Monica J Justice, Stephen G Waxman, Sulayman D Dib-Hajj, Miriam H Meisler, "The ataxia3 mutation in the N-terminal cytoplasmic domain of sodium channel Nav1. 6 disrupts intracellular trafficking" *The Journal of Neuroscience* (2009) **29**(9), 2733–2741.

[132] Osamu Ohara, Reiko Ohara, Hisashi Yamakawa, Daisuke Nakajima, Manabu Nakayama, "Characterization of a new β-spectrin gene which is predominantly expressed in brain" *Molecular brain research* (1998) **57**(2), 181–192.

[133] Yasuhiro Ogawa, Matthew N Rasband, "The functional organization and assembly of the axon initial segment" *Current opinion in neurobiology* (2008) **18**(3), 307–313.

[134] Martin Grumet, Vincent Mauro, Mark P Burgoon, Gerald M Edelman, Bruce A Cunningham, "Structure of a new nervous system glycoprotein, Nr-CAM, and its relationship to subgroups of neural cell adhesion molecules." *The Journal of cell biology* (1991) **113**(6), 1399–1412.

List of Figures

List of Tables

Acronyms

aa	amino acid
ABD	actin-binding domain
AIS	axon initial segment
ankB	ankyrin-B
ankG	ankyrin-G
AP	action potential
a.u.	arbitrary units
bfgf	basic fibroblast growth factor
bp	base pairs
BSA	bovine serum albumin
CNS	central nervous system
DAPI	4',6-Diamidin-2-phenylindol
dATP	desoxyadenosintriphosphat
dCTP	desoxycytidintriphosphat
dGTP	desoxyguanosintriphosphat
DIV	days in vitro
dTTP	desoxythymidintriphosphat
DNA	deoxyribonucleic acid
E18	embryonic day 18
EDTA	ethylenediaminetetraacetic acid
EMCCD	electron multiplying charge-coupled device
FWHM	full width at half maximum
HILO	highly inclined thin illumination
LED	light-emitting diode

MAP2   microtubule-associated protein 2

MEA   cysteamine hydrochloride

MEM   Minimum Essential Media

NA   numerical aperture

NaOH   sodium hydroxide

Nav   sodium channels

NF   neurofilament

noR   nodes of Ravier

NrCAM   neuronal cell adhesion molecule

PCR   polymerase chain reaction

P0   postnatal day 0 (newborn)

P2   postnatal day 2

PBS   phosphate buffered saline

PCs   purkinje cells

PH-domain   pleckstrin homology domain

PNS   pheriperal nervous system

PSF   point spread function

qv   quivering

RNA   ribonucleic acid

SDS   sodium dodecyl sulfate

SEM   standard error of the mean

shRNA   small hairpin ribonucleic acid

SH3   Src-homology 3

STORM   stochastic optical reconstruction microscopy

TIRF   total internal reflection fluorescence

TRIS   tris(hydroxymethyl)-aminomethan

UV   ultraviolet

VGSCs   voltage-gated sodium channels

Acknowledgments

Curriculum vitae

Melanie Dannemeyer

Date of birth: 24. Juli 1986

Place of birth: Bremen

Nationality: German

Education

12/2012 -	PhD in Biophysics, Georg-August University Göttingen
10/2010 - 09/2012	Master of Science in Genome Based Systems Biology,
	Bielefeld University and Arizona State University:
	Master thesis in Biophysics, Arizona State University:
	"Biophysical Characterization of Cancer Cells
	by Combined Atomic Force Microscopy -
	Confocal Fluorescence Microscopy"
	Supervisor: Prof. Dr. Robert Ros, Prof. Armin Gölzhäuser
10/2007 - 09/2010	Bachelor of Science in Molecular Biotechnology, Bielefeld University
08/1999 - 06/2006	High School - Gymnasium Brake

International Experience

12/2011 - 07/2012	Visiting Student, Robert Ros Lab, Center for Biological Physics,
	Department of Physics, Arizona State University, AZ.
09/2011 - 12/2011	Visiting Student, Alexandra Ros Lab,
	Department of Chemistry and Biochemistry,
	Arizona State University, AZ.
08/2003 - 05/2004	Student Exchange Year, South Hills High School, West Covina, CA.

Publications

Doss, B. L., Staunton, J. R., Dannemeyer, M., Linhart, M., & Ros, R. (2012). "Combined AFM Nanoindentation and Finite Element Analysis of Soft Heterogeneous Biomaterials", Microscopy and Microanalysis, 18(S2), 866-867.

Conferences

Talks

"Combined Atomic Force and Confocal Fluorescence Microscopy for Elasticity Measurements of Living Cells", Oral presentation at Biophest, University of Arizona, Tucson, 2012.

Posters

"Structural changes in the axon initial segment of developing neurons and qv3J mutants", Axons in the desert II, Israel, 2015.

"Imaging of VGSC Alteration in Cultured Hippocampal Neurons", 58th Annual Meeting of the Biophysical Society, San Francisco, 2014.

"Super-resolution Cryo-fluorescence Microscopy", Visit IMPRS Physics of Biological and Complex Systems, MPI for Biophysical Chemistry, Göttingen, 2013.

Scholarships

Rectorate Scholarship Bielefeld University, 2011.

PROMOS Scholarship for study abroad (DAAD), 2011-2012.

Miscellaneous

Trainer for Pre- and Postnatal Training, 05/2015.

Trainer for Muscle - Activity - Excellence, 03/2015.

Trainer for Indoor Cycling, 12/2014.

Group Fitness B-License at BSA-Academy, School of Health Management, 09/2014.